The Dissertation Committee for Justina Oichi Tam certifies that this is the approved version of the following dissertation:

Interactions of Composite Gold Nanoparticles with Cells and Tissue: Implications in Clinical Translation for Cancer Imaging and Therapy

Committee:

Konstantin V. Sokolov, Supervisor

Stanislav Y. Emelianov

Keith P. Johnston

Rajagopal Ramesh

John X.J. Zhang

Interactions of Composite Gold Nanoparticles with Cells and Tissue: Implications in Clinical Translation for Cancer Imaging and Therapy

by

Justina Oichi Tam, B.S.

Dissertation

Presented to the Faculty of the Graduate School of

The University of Texas at Austin

in Partial Fulfillment

of the Requirements

for the Degree of

Doctor of Philosophy

The University of Texas at Austin

December 2012

Dedication

To my wonderful God, family, and friends for their unending love and support.

Acknowledgements

I cannot put in words how grateful I am to my wonderful family. My mom and dad have always supported me throughout my schooling and did everything they could to ensure that I would have the best opportunities possible. My always-caring sister, Jasmine, brother-in-law, Brandon, and their baby, Toby, took me in when I first moved to Austin and made my transition into graduate school as easy as possible. They have been my biggest supporters in this journey and I am so blessed to have them in my life. My friends from home have also always been wonderfully encouraging.

I cannot thank my supervisor, Kostia, enough for his wonderful attitude towards me every day for over half a decade. He is a large reason why graduate school has had such a positive impact on me. I would also like to thank my committee members and collaborators who were a tremendous aid during my graduate career both in a research and career mentoring capacity: Stas, Dr. Johnston, Dr. Ramesh, and Dr. Zhang.

My labmates and collaborators were some of the most unique, friendly, and inspiring people I have ever met; Tim, Jesse, Sonia, Nate, Pratixa, Kort, Jenia, Veronika, Linda, Maria, Ryna, Frank, Albert, Doug, Avi, Leonid, Aris, collaborators from MD Anderson (Dr. Tomo, Ailing, and Shinji), Stas lab (Soon Joon, Valli, Bo, and many more) and Johnston lab (Jasmine, Avi, and Bobby) were wonderful people to work with and great friends. I should note that Tim in particular stands out in my personal experience because he is the most amazing mentor a new or seasoned grad student could ever have. A significant amount of work was performed by bright undergraduate students in our lab; Angel, John, Ehssan, Aziz, Neil, Allison, Angela, Asher, Jeja, and Neil have inspired me to be a better researcher. Angel in particular has been especially supportive of me during my graduate career and I am truly grateful for his encouragement. Also, this

work would not have been done without the tremendous help of some key university staff and students: Dwight Romanovicz, Haley Finjo, Isaac Arnquist, Hugo Celio, and all the ARC staff.

My roommates, Jasmine, Brandon, Mark, Dave, Richard, Shu, Toby, and Tuzi were all wonderful people to share graduate life with! I owe a special thanks to Mark, who has consistently been a voice of reason and a wonderful friend during my entire graduate career.

I was also extremely fortunate to befriend many wonderful people in my grad classes. Eileen, Kathy, Katy, and Krista were the first classmates I bonded with over homework in our classes, and I could not have gone through grad school without them as well as many others in the department. I cannot thank enough my colleagues and friends (and their dogs!) in the BME department; they have truly impacted my life positively and I am so grateful to have befriended them.

Lastly, I am grateful for funding from NIH that provided me with generous support.

Interactions of Composite Gold Nanoparticles with Cells and Tissue: Implications in Clinical Translation for Cancer Imaging and Therapy

Justina Oichi Tam, Ph.D.

The University of Texas at Austin, 2012

Supervisor: Konstantin V. Sokolov

Current methods to diagnose and treat cancer often involve expensive, time-consuming equipment and materials that may lead to unwanted side effects and may not even increase a patient's chance of survival. Thus, for a while now, a large part of the research community has focused on developing improved methods to detect, diagnose, and treat cancer on the molecular scale. One of the most recently discovered methods of cancer therapy is targeted therapy. These targeted therapies have potential to provide a patient with a form of personalized medicine because these therapies are biological molecules that specifically target other molecules involved with a cancer's growth.

Past trials using these therapeutic molecules, however, have led to controversial results, where certain patients responded better than others to the therapy for unknown reasons. Elucidating the reason behind these mixed results can be accomplished using metal nanoparticle technologies which could provide a bright signal to monitor the path that these therapeutic molecules take in vivo as well as enhance the molecule's efficacy. Literature has shown that presenting targeting molecules in a dense manner to their target

will increase these molecules' binding affinity. This concept has been explored here to increase binding affinity of therapeutic molecules by attaching these molecules in a dense manner on the surface of gold nanoparticles, and correlating this increased affinity with therapeutic efficacy. Additionally, gold nanoparticles provide an easy surface for molecules to be functionalized on and have shown to be effective imaging, x-ray, and photothermal therapy agents. A major roadblock to using these gold nanoparticles clinically is their non-degradability and thus potential to cause long-term negative side effects in vivo. A platform for developing biodegradable gold nanoparticles is also explored here to take advantage of the gold nanoparticles' excellent imaging and drug delivery capabilities while still allowing them to be used safely in the long term.

Table of Contents

List of Figures

Figure 3.18 225-NP is specific for EGFR-expressing tumor cells and pre-treatment with Clone 225 antibody abrogates 225-NP-mediated tumor cell killing. (a) The right column shows images of HCC827 cells pre-treated with Clone 225 antibody (2 μg/mL) for 15 minutes before incubation with either IgG-NPs (middle row) or 225-NPs (bottom row). Cells shown in the left column were not treated with free Clone 225 antibodies. The fixed cells were imaged using dark-field reflectance microscopy. Binding and uptake of 225-NPs was completely inhibited in the presence of Clone 225 antibody. In IgG-NP-treated cells, Clone 225 antibody had no effect. Scale bar is 50 μm. (b) Inhibition effect on the cytotoxicity of 225-NPs by pre-treatment with free Clone 225 antibody. After treatment with/without Clone 225 antibody (0.065 μg/mL) for 6 hours, the cells were treated with either non-conjugated nanoparticles (AuFe), IgG-NPs, or 225-NPs for an additional 66 hours. The number of viable cells was counted as described in Materials and Methods. Results shown are the means ± S.D. of three independent experiments. *P-value<0.05 vs. AuFe alone, Clone 225 antibody alone, IgG-NPs, or Clone 225 antibody plus 225-NPs. (c) Inhibition effects on 225-NP-induced apoptosis and autophagy by pre-treatment with Clone 225 antibody. Cellular proteins were lysed after treatment with 225-NPs ($6x10^9$ particles) for 66 hours in the presence of absence of free Clone 225 antibody (0.065 μg/mL). Proteins were separated by SDS-PAGE, and immunoblotted with anti-PARP and anti-LC3 antibodies. The anti-β-actin antibody was used as a control for protein loading and transfer. The intensities of the amount of LC3-II bands were quantified by ImageJ software. 225-NP-mediated

Chapter 1: Introduction

1.1 BACKGROUND: CURRENT LIMITATIONS IN DIAGNOSING AND TREATING CANCER

Cancer is a disease where cells divide uncontrollably. According to the National Cancer Institute's Surveillance, Epidemiology, and End Results (SEER) program, the expected number of deaths from cancer in the U.S. in 2012 is 577, 190, meaning 1,500 people are expected to die from cancer each day. The most common cancers are lung, bronchus, prostate, breast, and colorectal, and the lifetime probability of having cancer is quite high: 45% for men and 38% for women[1].

Even though cancer is a complex disease, there are basically six essential changes that normal cells undergo to become malignant cancer cells: self-sufficiency, unresponsiveness to antigrowth signals, evasion of programmed cell death, endless potential to replicate, tissue invasion, and metastasis[2]. Research into the mechanism behind this uncontrollable growth has revealed a complex circuit of molecules inside and outside the cell that play a large, interconnected role in cancer cell growth. For example, one important class of molecules involved in cancer growth is cell surface receptors that interact with growth stimulatory signals. These receptors can become deregulated and overexpressed, allowing the receptor to be hypersensitive to growth signals and trigger proliferation when, in normal cases, the receptor would not. One receptor that is overexpressed in multiple types of tumors including stomach, brain, breast, and lung is the epidermal growth factor receptor (EGFR). Ligand-independent signaling has been shown to occur with EGFR because a truncated version of the cytoplasmic domain of EGFR can fire constitutively[2].

In a person, these molecular abnormalities can manifest themselves as symptoms such as thickening of tissue, discomfort in eating, and unusual discharge. If a patient

exhibits symptoms of cancer, a physician will order tests that involve collecting blood and urine to ensure certain vital organs are functioning normally and to detect any tumor markers. These tests, however, are not sure signs of a presence of a disease, so medical imaging procedures are a crucial part of an accurate diagnosis[3].

Typical imaging procedures used to detect cancer are x-ray, computed tomography (CT) scans, radionuclide scans, positron emission tomography (PET) scans, magnetic resonance imaging (MRI), and ultrasound[3]. Though x-ray, CT, radionuclide, and PET scans can achieve high contrast for certain anatomical features, they are all limited by the dose of radiation or radioactive material that can be given to a patient. Additionally, these techniques are quite expensive to run. MRI provides a safer from of whole body imaging, but MRI is the most expensive imaging technique being used and lacks sensitivity. Ultrasound imaging is a safe and cost-effective method of imaging, but this technique lacks resolution, which is necessary for identifying early abnormalities such as neoplastic changes[4]. Technologies to enhance contrast in images can simultaneously improve resolution and decrease the required dose of excitation energy, allowing for safer and higher resolution imaging procedures to be available.

Oftentimes, to diagnose a patient, a physician will also collect a biopsy, which is a small sample of tissue, and send the sample to a pathologist who will stain the sample for different cellular markers and image the sample with a microscope[3]. This histopathological investigation is the gold standard for determining if cancer is present. This method, however, can be subjective because the result is based on an interpretation of the pathologist. Thus, more objective techniques are being explored to give more functional and quantitative information of the tissue sample.

If a physician determines the patient does indeed have cancer, standard methods of treatment include surgery, radiation therapy, and/or chemotherapy. Newer methods of

treatment include biological therapy and stem cell transplantation. Often, treatments damage healthy cells as well as cancer cells, and thus negative side effects ranging from rashes to death have been observed[3]. Recently, many research groups have worked to improve these existing therapeutic methods as well as improve current diagnostic methods to increase sensitivity, be less invasive, and yield results more quickly.

1.2 TARGETED THERAPY FOR TREATING CANCER ON THE MOLECULAR SCALE

Targeted therapies are substances that block tumors from growing by interfering with molecules that are critical for tumors to grow. Many of these therapies are small-molecule inhibitors or monoclonal antibodies[5]. Small-molecule inhibitors are typically identified in drug screens, while monoclonal antibodies are generated by immunizing a mouse with a target molecule and hybridizing the mouse's spleen cells with myeloma cells to produce a hybridoma cell line that will produce the monoclonal antibodies. Typically, for targeting intracellularly, small molecule inhibitors are used because they can diffuse into a cell, but for targeting cell surface receptors, larger, monoclonal antibodies are used. Certain types of monoclonal antibodies such as anti-EGFR antibodies, however, can enter cells by being actively transported into the cell after binding to a cell surface receptor indicating great potential for some antibodies to act as intracellular delivery agents.

Recent promising targets of cancer therapy include: oncogenes such as cMYC[6], inflammatory markers surrounding a cancer[7], various proteins such as nuclear factor kappa-light-chain-enhancer of activated B cells (NF-kappa B)[8], signal transducer and activator of transcription (STAT) proteins[9], vascular endothelial growth factor receptors (VEGFRs)[10], and epidermal growth factor receptors (EGFRs)[11].

In particular, EGFR has been extensively studied as a target because this receptor has been shown to be very important in the progression of multiple types of cancer. Patients with alterations in these receptors tend to have a more aggressive disease and thus worse clinical outcome[12]. The family of EGFRs consists of four types: EGFR/ERBB1, ERBB2, ERBB3, and ERBB4. All types have a ligand-binding domain on the surface of the cells and a cytoplasmic domain for binding tyrosine kinases. Upon binding of EGF ligands, EGFR will form homo- and heterodimers, and the cytoplasmic kinase domain of EGFR will be activated. There are two main types of EGFR drugs: small-molecule tyrosine-kinase inhibitors (TKIs) that block the tyrosine kinase from activating the cytoplasmic domain of the receptor by binding to the kinase's adenosine triphosphate (ATP)-binding site, and surface receptor-binding antibodies that block ligands from binding to the receptor extracellularly.

One monoclonal antibody targeting EGFR that is currently used in the clinic and in clinical trials is Cetuximab. Cetuximab has been shown to strongly inhibit cancer cell growth in EGFR-overexpressing cells and in mice tumor xenografts[13]. This antibody was approved by the FDA in 2003 for colorectal cancer and in 2006 for head and neck squamous cell carcinoma. Recent clinical trials have yielded mixed results, where some trials showed that Cetuximab improved the odds of response and reduced disease progression[14], while other trials have shown no difference in overall survival[15].

Targeted therapy induces cell death directly by apoptosis or indirectly by activating immune cells. Studies described here have also shown that targeted therapies assembled on a platform of nanoparticles can also induce another type of cell death, autophagy. Furthermore, understanding the pathways activated by our therapeutic molecules will allow us to design and tailor our therapy to a wide variety of individual patient's particular health needs.

Though we will not discuss here, other emerging forms of targeted therapy include cancer vaccines and gene therapy. One concern of targeted therapies is their ability to become ineffective over time as the cancer develops resistance. In particular, resistance to anti-EGFR drugs has been observed, leading many to suggest targeted therapies like Cetixumab be used in combination with other drugs such as HER2/neu targets to increase therapeutic efficacy[16].

1.3 NANOPARTICLES FOR IMAGING AND TREATING CANCER

1.3.1 Overview

Nanoparticles hold great potential for offering improved methods to treat and image cancer. Along with the fact that traditional drugs for cancer are non-specific, another large problem with systemically administered drugs is that often, the cancer develops resistance to these drugs[17]. Resistance means that a tumor is not decreasing in size or has relapsed after initially decreasing[18]. Resistance can come in two forms: non-cellular based and cellular based[17]. Non-cellular based resistance arises from poor vasculature, acidic microenvironments, and high interstitial pressure. Cellular based resistances arise from altered enzyme activity, altered apoptosis and transport mechanisms, and increased multi-drug resistance (MDR) efflux systems[18-19]. Nanoparticles offer a way to overcome these drug resistances by protecting drugs during their transport as well as decreasing their toxicity toward normal cells. Additionally, nanoparticles have shown an ability to evade MDR, and some speculate this is because a protein that is often involved in MDR, P-glycoprotein (Pgp), only activates efflux of drugs when the drugs are in the plasma membrane, and not if they are in the cytoplasm or in lysosomes (Figure 1.1).

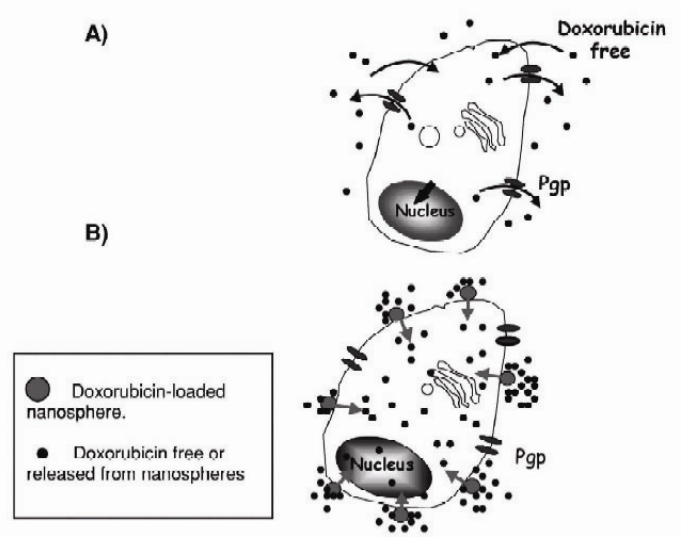

Figure 1.1 (A) Free doxorubicin is small enough to diffuse into a cancer cell, but is effluxed by a multi-drug resistance (MDR) protein, Pgp. (B) Doxorubicin encapsulated in nanospheres bind to the cell membrane and release doxorubicin, creating a concentration gradient that could saturate Pgp and overcome MDR[17].

Nanoparticles are submicrometer colloidal systems that can act as delivery vehicles for drugs. These nanoparticles can accumulate in a tumor via passive diffusion across a highly permeable tumor vasculature[20] or by active targeting[21]. Additionally, retention of nanoparticles in the tumor can occur from poor clearance by lymphatics of neoplastic tissue. To detect a tumor and its boundaries, many nanoparticles have been used to target specific cancer markers and provide qualitative and quantitative analyses of tumor location and spread. Common nanoparticles used for treating and imaging cancer are organic, quantum dots, magnetic, carbon, and gold nanoparticles.

1.3.2 Organic nanoparticles

1.3.2.1 Polymer-drug conjugates

In the 1980's, the first nanoparticles were used to deliver drugs in clinical trials, and a decade later, these nanoparticle-drug conjugates became commercially available[22].

One of the earliest reports of using nanoparticles to treat cancer was in 1979 with drugs adsorbed onto a polymer nanoparticle, polyalkylcyanoacrylate[23]. Polymers are the most commonly researched material to develop nanoparticle carriers. Polymer-drug conjugates (6-15nm) have been shown to target various types of tumors and blood vessels, and as of 2006, had 12 products being evaluated in clinical trials[24]. Though a wide range of drugs and polymers have been used in research, only four drugs (doxorubicin, amptothecin, paclitaxel, and palatinate) and four polymers (N-(2-hydroxylpropyl)methacrylamide (HPMA) copolymer, poly-L-glutamic acid, poly(ethylene glycol) (PEG), and dextran) have been used to develop polymer-drug conjugates[22].

1.3.2.2 Liposomes

Researchers have shown that liposomes of a size of 200nm can effectively extravasate from leaky vasculature to a nearby tumor[25]. In the past few years, liposomes (85-100nm) have been extensively studied in Phase I-III clinical trials, and are used to treat solid tumors. Liposomes are spherical, closed structures formed by multiple lipid bilayers. These lipid based carriers are biocompatible, biodegradable, and their surface can be easily modified. These carriers, however, have been shown to rapidly clear from the body via the reticuloendothelial system[17, 26] and are characterized by a burst release of drug.

1.3.2.3 Polymeric nanoparticles

Polymeric nanoparticles can be made of synthetic polymers like polylactic acid and poly(lactic-co-glycolic acid), or of natural polymers like chitosan and collagen. These polymeric nanoparticles are in the size range of 50-200nm, and are being studied in Phase I-III clinical trials for treating a variety of cancers[27].

1.3.2.4 Dendrimers

Dendrimers are synthetic macromolecules that have a branched structure, are biocompatible, and have high water solubility[22]. Additionally, targeting molecules, imaging agents, and drugs can be easily conjugated to these dendrimers. Challenges to their use in the clinic include the fact that they are rapidly cleared from the body owing to their small size, and are more expensive to make compared to other types of nanoparticles.

1.3.3 Quantum dots

Nanoparticles can also serve as contrast agents. Traditionally, clinically used optical imaging methods involve fluorophores as contrast agents. Fluorescent proteins and organic dyes, however, are neither as bright nor as stable as metal nanoparticles or quantum dots (Figure 1.2).

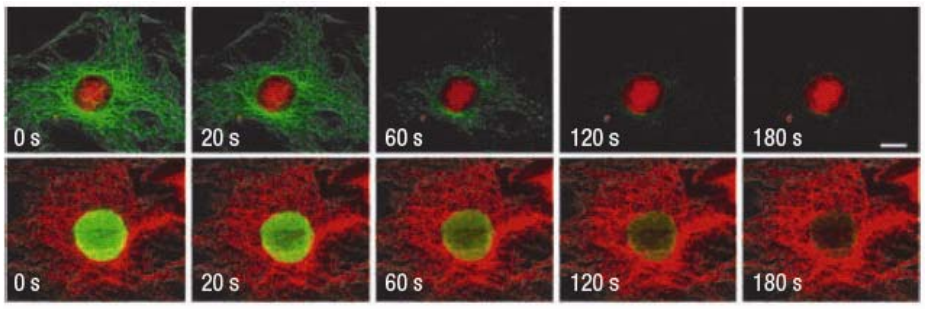

Figure 1.2 Organic dyes undergo more photobleaching than quantum dots. Top row: Nuclei of 3T3 cells were labeled with quantum dot QD 630-streptavidin (red) and microtubules were simultaneously labeled with AlexFluor 488 (green). Bottom row: Microtubules were labeled with QD 630-streptavidin (red) and nuclei were labeled were labeled with AlexaFluor 488 (green). Scale bar is 10μm[28].

Quantum dots are particles that are quantum confined, surrounded by a stable polymer shell[29]. These quantum dots have unique optical and electronic properties with

molar extinction coefficients about 10-100 times larger than traditional organic dyes[30], size-tunable fluorescence emission in near infrared wavelengths[29], and a broad excitation spectrum that allows for multiplexing by exciting a mixed population of quantum dots, while detecting emission wavelengths that are far from their excitation[31]. Quantum dots were first synthesized in the early 1980's[32] and since then, have been used in diagnostic devices[33]. One of the earliest uses in vivo was imaging and quantifying cancer biomarkers on the surface of pancreatic cancer cells[34], image tumors and lymph nodes in mice[29, 35], and as photo-therapy agents[36]. Concerns over the quantum dots' toxicity had initially plagued their ability to be seen as a clinical diagnostic and treatment tool, but more recently, researchers have shown they are nontoxic if protected by a stable coating[29, 30b, 37]

1.3.4 Magnetic nanoparticles

Currently, magnetic resonance imaging (MRI) is the preferred method of cross-sectional imaging in the brain, spine, and muscoskeletal system[38]. Magnetic nanoparticles have proven to be useful as dual functioning MRI contrast agents and therapeutic hyperthermia agents. The first reported use of magnetic nanoparticles in vivo was in the 10th century and involved magnetite grains that were given to a patient who had swallowed rust, to speed up the excretion of the poisonous rust[38].

Recently, magnetic nanoparticles have been used to deliver a large payload to specific areas in the body and provide strong contrast in MRI images using an externally applied magnet targeted to the site of interest. Nd-Fe-B capsules were delivered to the brain with an accuracy of 2mm[38], and dextran-coated iron oxide nanoparticles showed strong potential as MRI contrast agents[39]. MRI is based on a nuclear magnetic resonance (NMR) signal of protons, after being excited by a strong static magnetic field (clinically,

up to 2T) and a transverse radiofrequency-field (5-100MHz). The excited protons relax back to equilibrium as the net magnetization vector tries to realign with the longitudinal axis of the magnetic field[40]. There are two types of relaxation processes: T1-recovery, which is longitudinal relaxation, and T2-decay, which is transverse relaxation. Different types of tissue have different T1 and T2 values. Fluids typically have a long T2 and are associated with diseases[38]. Initial forays into gaining contrast in MRI came from the difference between deoxy- and oxygenated hemoglobin, but this difference was very small, so researchers turned to using exogenous contrast agents. The first exogenous agents were gadolinium (Gd) ions, which are high spin paramagnetic ions[38]. To protect tissue from the Gd ions' toxicity, a chelator DTPA was incorporated into the contrast agent. From there, superparamagnetic materials were explored and showed higher magnetic moment than the paramagnetic particles. These superparamagnetic contrast agents yielded T2-relaxation effects, which resulted in a signal reduction on T2-weighted images[38]. Most T2 agents are made up of Fe_3O_4 or Fe_2O_3. When these Fe_3O_4 or Fe_2O_3 nanoparticles are in the presence of a magnetic field, they induce a local field inhomogeneity that causes nearby protons to dephase. This dephasing results in transverse relaxation, and the total relaxation time T2* is given by Equation (1).

$$\frac{1}{T2*} = \left(\frac{1}{T2}\right) + \gamma Bs \qquad (1)$$

where γBs represents the relaxation by field inhomogeneities and is the susceptibility effect[41].

Magnetic nanoparticles used for hyperthermia of cancer would require nanoparticles to be concentrated around or inside a tumor. These nanoparticles would then absorb energy from an external alternating magnetic field and heat its

surroundings[38]. There are two types of hyperthermia: mild hyperthermia which heats tissue between 41-46 degrees C to stimulate an immune response, and thermoablation, which heats tissue up to 56 degrees C, which leads to tumor destruction via necrosis[42]. Studies have shown that certain parameters must be met for hyperthermia to be usable for patients. The product of the amplitude and the frequency of the magnetic field must be lower than 4.85×10^8 $Am^{-1}s^{-1}$ for one hour, and the frequency must be higher than 50kHz to avoid electrically stimulating neuromuscular junctions but lower than 10MHz to achieve good penetration depth[38]. Upon excitation by an AC magnetic field, the magnetic moments of nanoparticles rotate and then relax to equilibrium, termed Neel relaxation. In 2003, a successful human trial using Fe_3O_4 nanoparticles modified with aminosilane groups to induce hyperthermia was demonstrated in a patient with chondroscarcoma, which is a cancer comprised of cells that produce cartilage[38]. Additionally, iron oxide nanoparticles have also been used in diagnostic devices to detect circulating tumor cells using immunomagnetic properties combined with a microfluidic device for high-throughput monitoring of cancer ex vivo[43].

1.3.5 Carbon nanoparticles

Carbon nanostructures have shown strong potential as medical contrast agents[44]. They have shown to have higher relaxivity values compared to conventional MRI contrast agents composed of Gd-(III), are biocompatible, and can cross cell membranes[44]. Limitations of these particles, however, include the fact that these particles have demonstrated aggregation in vivo and are quickly taken up by the reticuloendothelial system [45]. Recent developments have improved the stability of these nanoparticles and have allowed for renal clearance within one hour of injection[46].

1.3.6 Gold nanoparticles

Since the 1970's, metal nanoparticles have been used to immunolabel biological molecules for electron microscopy[47]. More recently, gold nanoparticles have been used in cellular and medical imaging[48]. Compared to other nanoparticles, gold nanoparticles serve as a flexible platform for tuning a variety of parameters such as size, shape, composition, and structure, which lead to various optical properties[49]. Chapter 2 will discuss further the chemical and optical properties of gold nanoparticles and their recent uses as biomedical delivery, contrast, and therapeutic agents.

1.4 DISSERTATION SUMMARY

This dissertation builds on the past few decades of research that indicate strong potential for metal nanoparticles to be used as diagnostic and therapeutic agents of cancer. Here, we look at specific parameters that are of utmost clinical importance such as the nanoparticles' ability to enhance therapeutic efficacy of currently used drugs, and the particles' ability to be efficiently cleared by the body to avoid potential long term side effects.

Chapter 2 examines the properties of gold nanoparticles that are critical for their in vivo use, and their recent uses as delivery, imaging, and therapeutic agents in cells and animals.

Chapter 3 looks at the therapeutic efficacy and activated paths of therapeutic antibodies conjugated to gold nanoparticles on lung cancer cells. These antibodies are the mouse analog of a clinically used targeted antibody-drug, Cetuximab.

Chapter 4 provides a method for developing biodegradable plasmonic nanoparticles and shows both in vitro degradation and in vivo clearance of biodegradable gold nanoclusters.

Chapter 5 summarizes the use of gold nanoparticles as clinically useful diagnostic and therapeutic agents, and the outlook of using these nanoparticles in the clinic

Chapter 2: Requirements of Nanoparticles for In Vivo Use: Properties and Applications in Molecular Medicine

Metal nanoparticles, especially plasmonic nanoparticles such as gold nanoparticles, have shown a strong potential for a variety of biomedical applications, ranging from ex vivo sensing to in vivo therapy. To be used in vivo, nanoparticles must have certain properties: be biocompatible, characterizable, functionalizable, soluble or colloidal, have low rate of aggregation, exhibit uptake into target cells over normal cells, allow for monitoring over time, and have long circulating life[22]. In this chapter, examples of nanoparticles, with emphasis on gold nanoparticles, and the properties that allow them to meet these requirements are given. Additionally, recent uses of these nanoparticles in diagnosis and therapy are highlighted.

2.1 PROPERTIES OF GOLD NANOPARTICLES

2.1.1 Synthesis

2.1.1.1 Spheres

An initial synthesis of gold nanoparticles was developed in 1951 by Turkevich[50] and involves reducing gold ions to nanoparticles using citrate[51], where the citrate also stabilizes the already-formed nanoparticles. Stabilizers other than citrate can be used during synthesis of gold and will prevent aggregation via Coulombic repulsion or steric hindrance[52]. The size of the nanoparticles can be tuned simply by controlling the ratio of citrate to $HAuCl_4$[53]. This type of solution phase synthesis of metal nanoparticles allows for control over size, shape, composition, and structure of the particles and tends to yield an energetically favorable shape of a sphere[52].

A more recent method for synthesizing gold spheres was developed in 2000 using a seed-mediated growth to synthesize a more monodisperse solution for large diameter

(>20nm) spheres than the previously used Turkevich method. This synthesis involved growing the gold nanoparticles using initial gold seeds and NH_2OH.

Another commonly used procedure for synthesizing gold particles is the Brust-Schiffrin method[54]. This method involves both an aqueous and an organic phase along with a phase-transfer agent tetractylammonium bromide to reduce $AuCl_4$ anions with $NaBH_4$ in the presence of alkanethiols, resulting in thiol-stabilized particles[55]. Since then, simpler, single-phase methods have been developed.

2.1.1.2 Non-spherical particles

Non-spherical particles such as rods can be made using established methods such as electrochemical ionization and reduction of gold[56] or seed-mediated growth using gold spheres as seeds to grow rods in the presence of excess gold ions and surfactant cetyltrimethylammonium bromide (CTAB)[57]. Because CTAB is considered cytotoxic, other less cytotoxic surfactants have been explored such as liquid-chlorin photosensitizers from algae and choline hydroxide[51]. The aspect ratio of these rods can be easily changed by varying the concentration of silver ions[49]. These rods exhibit plasmon resonances in the near infrared region (NIR), which is optimal for medical optical-based imaging because common tissue chromophores have low absorption in the NIR wavelength range (Figure 2.1).

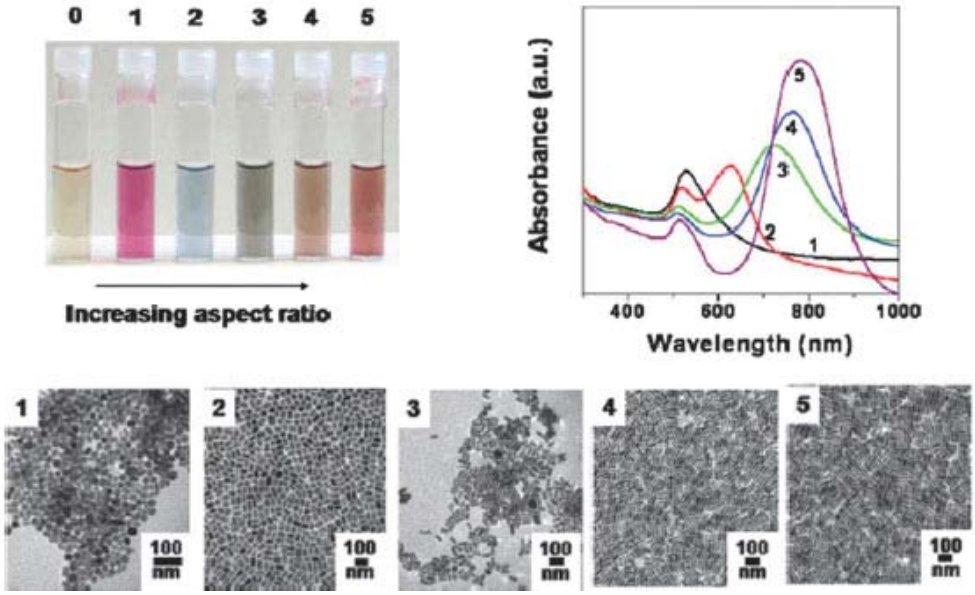

Figure 2.1 Optical properties of gold nanoparticles change with shape. (Top left) Photographs of solutions of 4 nm gold spheres (vial 0) followed by increasing aspect ratios (vials 1-5). (Top right) Absorbance spectra of solutions from vials 1-5. (Bottom) TEM of nanoparticles from vials 1-5. Scale bars are 100 nm in all TEM images[58].

Another type of metal nanoparticle that can be tuned to the NIR range is a core/shell nanostructure of silica/gold, termed nanoshells. The silica cores are functionalized with an amine-terminated silane that binds to small gold particles. Subsequent layers of gold are added by electroless plating[59]. A similar method has also been used to synthesize another NIR absorbing particle, the nanorice[60].

Another procedure for synthesizing NIR absorbing particles involves using ethylene glycol as a solvent and reducing agent at elevated temperatures. This procedure has been used to synthesize NIR absorbing nanoplates and nanocages[61].

2.1.2 Bioconjugation

Gold nanoparticles capped with citrate can be easily replaced with other ligands[62]. A stable bond between thiol and gold was first observed in 1993[63]. More recently, a

popular method of thiolating gold nanoparticles is performed using the Schiffrin-Brust synthesis as described in Chapter 2.1.1.1[54]. Another popular method of conjugating to gold nanoparticles is through a "click" reaction, linking terminal alkyne and an azide[64]. A common method of functionalizing gold nanoparticles that have a terminal carboxylate group is to attach a molecule with an amino group on one end using EDC chemistry and a desired group on the other end[65]. Nanoparticles have also been conjugated to a versatile molecule, the dendrimer, using a solution containing a pre-organized number of internal ligands during synthesis, resulting in dendrimer encapsulated gold nanoparticles[51, 66]. Stable nanoparticle conjugates have been synthesized using PEG sorbitan fatty acid esters functionalized with lipoic acid, which contains a disulfide bond. These conjugates have been shown to be stable in environments of pH 1-14[51, 66]. Recently, directional conjugation of antibodies has been achieved by allowing the antigen-binding sites of the Fab portion of an antibody to be directed outward towards the target[67] (Figure 2.2). This is accomplished by attaching a heterobifunctional linker to the Fc region of a glycosylated antibody, allowing the Fab portion of the antibody to be free to interact with a target. The linker consisted of an amide-bonded adipic hydrazide and an alkane ending in a dithiol group to attach to gold nanoparticles with near-covalent strength.

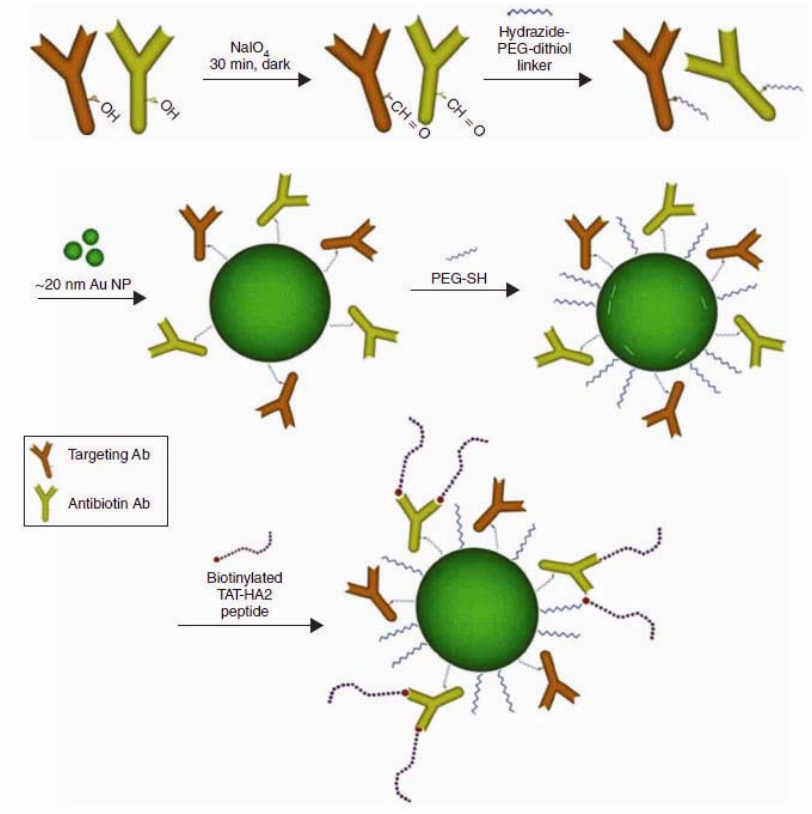

Figure 2.2 Schematic of directional conjugation of antibodies on gold nanoparticle surface[67].

2.1.3 Optical properties

Optical properties of gold nanoparticles have been of interest since Faraday reported the first scientific article about them in 1857[51]. Then in 1908, Mie used Maxwell's equations to describe the extinction spectra of spherical particles of arbitrary size[68]. Because Mie's theory assumes the spherical particles and surrounding media are homogenous[52], there are some challenges when applying this theory to medical optics[69]. Complicating factors include non-spherical particles, the presence of a supporting substrate, a solvent layer on top of the particles, and particles that are so close together there is electromagnetic coupling of the particles[69].

Since Mie's time, numerical methods such as T-matrix formalism, discrete dipole approximation (DDA)[70], and finite-difference time-domain simulations[71] have been used to calculate the optical properties of nanoparticles for complex cases. Mie's theory, however, is still widely used today because it is the only simple, exact solution to Maxwell's equations that is relevant to particles[52].

When light irradiates a small metal sphere, the incoming oscillating electric field causes the sphere's conduction electrons to oscillate coherently (Figure 2.3).

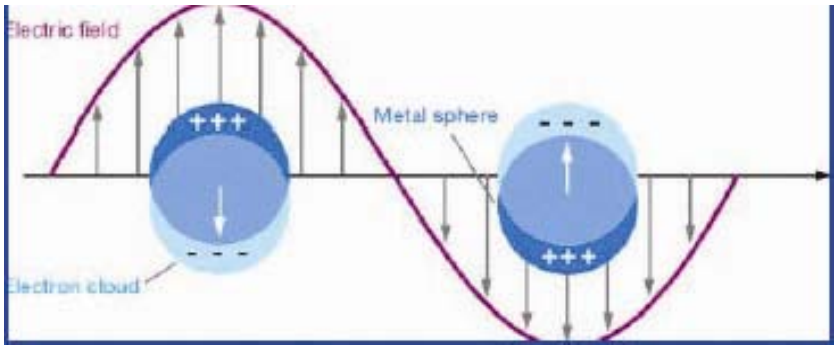

Figure 2.3 Schematic of a displacement of an electron charge cloud relative to the nucleus of a metal sphere, resulting in a localized surface plasmon[52].

Subsequently, after these conduction electrons are displaced, the electrons are attracted back to the positively charged nucleus, resulting in an oscillation at a frequency that is governed by: the density of electrons, effective electron mass, and shape and size of the charge distribution. This collective oscillation of electrons is termed the dipole plasmon resonance of the particle[69], which is the simplest type of local surface plasmon resonance (LSPR). Larger particles have higher multipoles, where a quadrupole term must be taken into account, as well as retardation effects[52, 69]. Very small nanoparticles <3 nm do not exhibit this plasmon resonance because at this small size, the gold is no longer a piece of metal with a conduction band, but is a molecule described by its

molecular orbitals[51]. The particle's dipole plasmon frequency occurs because all the conduction bands oscillate in phase with each other and this leads to a buildup of polarization charge at the surface of the particle[52, 69]. There is also a homogenous buildup of charge inside the particle and this is manifested in strong scattering and an enhanced electric field at the surface of the particle[52]. The LSPR's maximum intensity and spectral position varies with the size, shape, composition, and local environment of the nanoparticle[72].

The optical properties of noble metal nanoparticles are best described by a complex, wavelength-dependent dielectric constant ϵ given by Equation (2)[52].

$$\epsilon(\lambda) = \epsilon_{\mathrm{r}}(\lambda) + i\epsilon_{\mathrm{i}}(\lambda) \qquad (2)$$

where $\epsilon = m^2$ and $m = n + ik$ is the complex refractive index given as a function of the refractive index, n, and the absorption coefficient, k. In the electrostatic dipole regime, the extinction of a spherical metal nanoparticle can be described by Equation (3).

$$E(\lambda) \propto \frac{\epsilon_{\mathrm{i}}}{(\epsilon_{\mathrm{r}} + \chi\epsilon_{\mathrm{med}})^2 + \epsilon_{\mathrm{i}}^2} \qquad (3)$$

where ϵ_{med} is the dielectric constant of the surrounding medium, λ is the excitation wavelength, χ is a form factor that is related to the aspect ratio (χ=2 for a sphere, and increases with increasing aspect ratio), ϵ_{i} is the imaginary component of the dielectric function of the metal spheres, and ϵ_{r} is the real component. When the real component of the dielectric constant is much greater than the imaginary component, then a maximum extinction occurs when $\epsilon_{\mathrm{r}} = -2 * \epsilon_{\mathrm{med}}$. At this maximum is where the LSPR occurs[52].

When the refractive index increases, there is a red shift in extinction spectrum because of a buildup of polarization charges on the dielectric side of the interface, which will weaken the total restoring force[52]. When we have larger particles beyond the Rayleigh approximation (diameter > 30nm), a red shift is also observed as well as a

broadening of the extinction spectrum. The red shift occurs because as the particle becomes larger, the conduction electrons do not all move in phase with each other and this causes a retardation effect which leads to a reduced depolarization field at the center of the particle[73]. Broadening of the spectrum is attributed to radiative losses, which could translate into a loss of sensitivity for biosensing applications[74].

For a NIR absorbing particle such as a nanorod, the plasmon resonance exhibits two peaks, and as the aspect ratio increases, so does the distance between the two conduction bands. Other NIR absorbing agents such as triangular nanoparticles also have multiple plasmon resonances, with very large field enhancements at their tips[75].

Typical sizes of gold nanoparticles that are used for biomedical applications are 40-80 nm. Using Mie theory and discrete dipole approximation, extinction and scattering efficiencies were calculated for three common types of gold nanoparticles: spheres, rods, and nanoshells, along with some conventionally used absorbing dyes for comparison[76]. Results showed that, compared to conventional absorbing dyes, all gold nanoparticle types yielded orders of magnitude higher optical cross sections than absorbing and fluorescent dyes[76]. Gold particles of 40nm in size are often used as biological imaging agents. These 40nm spheres yielded an absorption cross section of 7.7×10^{9} $M^{-1}cm^{-1}$ at 528nm, which is five orders of magnitude greater than a clinically used NIR absorbing dye indocyanine green (ICG), 1.1×10^{4} $M^{-1}cm^{-1}$ at 778nm. 80nm particles showed an equally high margin in scattering cross section (3.2×10^{10} $M^{-1}cm^{-1}$) over a commonly used fluorescent molecule, fluorescein (9.2×10^{4} $M^{-1}cm^{-1}$ at 483nm with a quantum yield of ~0.98)[76].

Using these calculations, for spheres, as diameter increased from 20 to 80 nm, so did the extinction and scattering contribution. Red shifting occurred slightly with increasing size. Nanoshells demonstrated advantages over spheres in that they exhibited

plasmon resonances in the NIR as well as had higher optical cross-sections. Their extinction was linearly dependent on their overall size, but independent of their core/shell radius. The scattering contribution increased as thickness of the shell increased, and red shifting occurred as the total size of the nanoshell increased or with a decrease in shell thickness. Concerning rods, as the effective size increased, so did the extinction and relative scattering contribution, but the absorption contribution remained dominant for all sizes of rods. Both extinction and scattering contribution were independent of the rod's aspect ratio, but red shifting occurred with increasing effective radius or increasing aspect ratio. Ultimately, per micron, rods yielded an order of magnitude higher absorption and scattering than both spheres and rods. Thus, rods are strong candidates for optical imaging agents in vivo, however, their biocompatibility, stability under laser heating, and clearance in vivo still need to be fully characterized before they can be widely used as a systemic agent.

2.1.4 Cytotoxicity

There have been concerns about the cytotoxicity of gold nanoparticles at the concentration that they will typically be administered at, which is 1-100 nanoparticles per cell[51]. In general, reports have shown that gold nanoparticles show little toxicity[51]. Cationically functionalized aklythioloate-gold nanoparticles containing trimethylammonium ligand termini were used to translocate DNA across a cell membrane and were only toxic at concentrations that were two times higher than needed for maximal transfection. Control nanoparticles without cationic surface charge were non-toxic[51]. Another study showed that gold nanoparticles bound to a variety of ligands including biotin, cysteine, citrate, and glucose did not appear toxic to human leukemia cells (K562) up to a concentration of 250 mM, while $HAuCl_4$ was highly toxic, killing

90% of cells[77]. Results of nanoshells in mice showed no complications[78]. Au-Cu-shells led to dose dependent cytotoxicity, with 67% viability at higher doses[51]. The CTAB layer on gold nanorods has been shown to be toxic[79], but rods coated in layer-by-layer polyelectrolytes showed low toxicity[80]. Another ligand, PEGylated-biotin-PEG-poly(caprolactone) conjugated to gold nanoparticles showed minimal toxicity on Caco2 cells[80].

2.1.5 Biodistribution

Blood and lymphatic vessels provide a route for nanoparticles to be delivered to specific sites in the body, but it is not clear how to manipulate this intricate path of vessels to target certain sites[81]. Even the most active compounds in vitro are useless if they do no circulate in the blood long enough to reach their target by avoiding the immune system and rapid excretion[82]. Different routes of administration have led to different biodistributions. Injections of nanoparticle-drug conjugates via subcutaneous, intramuscular, and topical routes have led to a higher retention of drug than free drug, but the conjugates were typically found in local lymph nodes[83]. The uptake of nanoparticles by phagocytes in vivo depends on the size, surface charge, and hydrophobicity of the particles[84]. The mononuclear phagocyte system, or the reticuloendothelial system, consists of bone marrow progenitors, blood monocytes, and tissue macrophages[85]. During the clearance process, first, circulating proteins called opsonins absorb onto foreign particles and then interact with certain receptors on monocytes and macrophages[38]. These opsonins include fibronectin, immunoglobulins, and complement proteins[81]. Different types of particles attract different types of opsonins, leading to different clearance rates for these different particles[86].

After intravenous injection, typically, nanoparticles are rapidly cleared from the blood by the liver's Kupffer cells and the spleen's marginal zone and red pulp[21]. Nanoparticles larger than 200 nm clear faster than small nanoparticles[21]. Long-circulating particles are ideal for tumor accumulation because they predominantly escape the blood stream only when there are fenestrations such as in the sinus endothelium of the liver or when there is leaky vasculature such as is typically found surrounding a tumor[21, 87]. Liver fenestrations can be as large as 150 nm, while tumor capillary fenestrations can be as large as 300 nm[81]. Splenic filtration often occurs as well, with slits as large as 200-250 nm[21]. Nanoparticles with long circulation times have been achieved using clodronate to impair macrophages in the liver[88], but this strategy will be difficult to translate to the clinic because an essential defense system will be suppressed potentially for a couple of weeks[38, 88a].

Coating nanoparticles with amphiphilic chains has been observed to decrease phagocytosis of the nanoparticles in vivo, and lead to an increase in blood residence time[89]. Also, hydrophilic coatings of dextran, poloxamer (PEO-PPO-PEO) and PEG have been used to add stealth to the particles by suppressing macrophage recognition, leading to reduced adsorption and surface opsonization[81]. Poloxamine-908-coated spheres showed to increase the blood half-life of spheres up to 1-2 days[90]. PEG has shown to suppress protein adsorption at an optimal molecular weight of 2kD to 5kD[21, 91]. Recently, to increase stability of PEGylated nanoparticles in vivo, a short hydrophobic layer was conjugated to gold nanoparticles on one end and to PEG on the other end. The hydrophobic layer provides a shield to prevent proteins from slipping through the PEG layer and destabilizing the PEGylated particles. These novel conjugates have shown decreased uptake in macrophage cells compared to PEGylated nanoparticles without a

hydrophobic layer, indicating great potential for these conjugates to have increased stealth in vivo[92].

The biological distribution of gold nanoparticles after intravenous administration showed that overall, nanoparticles between the sizes of 15-200 nm accumulated in the liver, spleen, and lungs. Distribution between other organs was size dependent. Both 15 and 50 nm were found in the brain, while only a small amount of 200 nm particles was found in the brain, blood, stomach, and pancreas[93]. A similar study injecting gold nanoparticles into rats showed 10 nm particles were distributed between various organs while 50-250 nm particles ended up only in liver, spleen, and blood[94]. Typically, nanoparticles of 30-100 nm in size are optimal to prevent rapid clearance from blood by leakage into blood capillaries and macrophages[95]. Surface chemistry can also play a role in biodistribution. Bare hydrogel nanoparticles have shown to have an increased accumulation in the liver compared to the spleen, while PEGylated hydrogels showed a more even distribution between liver and spleen[96]. A hypothesis for this difference in distribution is that particles with longer circulation times have a higher chance of being exposed to the spleen and thus uptake by splenic phagocytes is more likely for PEGylated particles which have a longer circulation time than non-PEGylated particles[97]. Concerning very small gold nanoparticles, an intravenous injection of 1.4 and 1.8 nm particles showed that 1.4 nm could travel through the air/blood barrier in the lungs, but 1.8 nm was trapped in the lungs[98].

Comparing lipoic acid and monothiol PEG, gold nanoparticle surfaces functionalized with lipoic acid were more stable, and comparing 20, 40, and 80 nm gold conjugated to 5kD PEGylated lipoic acid, 20 nm yielded the lowest uptake by the reticuloendothelial system and the highest uptake into a tumor[99]. Targeting agents can be conjugated to the nanoparticle surface to improve the stability of the nanoparticles and

increase affinity of the nanoparticles to a tumor[100], as well as determine the nanoparticle's path of internalization, whether through receptor-mediated endocytosis or lipid raft-dependent macropinocytosis[81]. More recent results, however, showed that targeting agents may not always influence tumor accumulation as much as specific cell uptake after already arriving in the tumor vicinity via passive targeting[101]. Gold nanorods conjugated to ScFv antibodies did not show statistically different accumulation in a tumor compared to non-targeted nanorods, but histopathology revealed that targeted nanorods accumulated in tumor cells while non-targeted nanorods accumulated in extracellular matrix[101b].

2.2 GOLD NANOPARTICLES FOR BIOMEDICAL APPLICATIONS

2.2.1 Sensing and imaging

Besides the traditional application of using gold nanoparticles in immunostaining for TEM, gold nanoparticles have been used as contrast agents in a wide variety of detection and imaging methods such as biosensing technologies, magnetic resonance imaging (MRI), surface enhanced Raman scattering (SERS), and photoacoustic (PA) imaging.

2.2.1.1 Biosensing

For detecting molecules in solution, gold spheres, nanoshells[102], nanorods[58], and nanowires[103] have been used to detect proteins[104], viruses[105], and nucleic acids[106] at as low as femtomolar concentrations of target analyte. Gold nanoparticles have been extremely useful in biosensing techniques because of their plasmon coupling property. When the inter-particle space decreases, the color of the solution changes, and this color change can provide a quick visual detection of the presence of an analyte. In 1980, initial studies involving this plasmon coupling effect for sensing was performed by

Leuvering[107], and more recently this method has been improved upon using hyper-Raleigh scattering. In 1996, Mirkin was the first to use this colorimetric type of assay using gold nanoparticles to detect nucleic acids[106] and he and his colleagues have since extended the technique to detect endonuclease activity in real time[108]. Gold nanoparticles have also been used in fluorescence detection assays. Though gold nanoparticles have low quantum yields, they fluoresce strongly under a high excitation light[51]. Gold nanoparticles have also been used as strong fluorescent quenchers, and have shown to quench fluorescent dyes by 50% when the dyes are only 25 nm away[109]. This quenching method has been used to detect large proteins that can act as a spacer between a fluorophore and a gold nanoparticle to inhibit quenching[110]. Gold nanoparticles have also served as nanoelectrodes for electrochemical sensing because the turnover rate of electrons transferred through gold nanoparticles is about seven times higher than through some catalytic enzymes such as glucose oxidase[51].

2.2.1.2 MRI

For whole body imaging such as MRI, 2 nm gold particles have been used to deliver Gd chelates to a specific site in the body and showed a higher relaxivity (586 $nM^{-1}s^{-1}$) than gold nanoparticle-free Gd chelates (3 $nM^{-1}s^{-1}$)[111]. Hybrid nanoparticles made up of gold coated iron oxide nanoparticles have also shown strong potential as dual optical and MRI contrast agents in T2 weighted imaging (Figure 2.4)[112] .

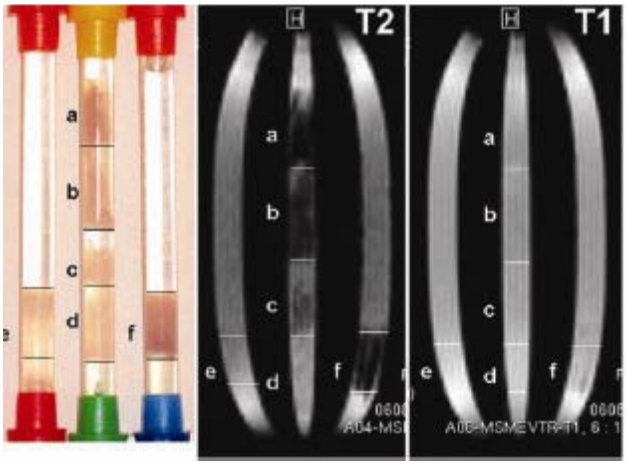

Figure 2.4 MRI images of cell phantoms labeled with anti-EGFR hybrid core/shell iron oxide/gold nanoparticles. Left: Sections (a)-(d) are MDA-MB-468 cells treated with anti-EGFR hybrid nanoparticles from (a) highest concentration to (d) lowest concentration, and (f) is a positive control of cells labeled with the highest concentration of nanoparticles. Middle: T2 weighted image of the tubes in the left photo. Right: T1 weighted image of the tubes in the far left photo[112b].

2.2.1.3 SERS

Gold nanoparticles have also been extensively used for surface enhanced Raman scattering (SERS) techniques. When Raman active molecules are placed within 10 nm of a gold nanoparticle surface, an enhanced SERS signal 10^{14}-10^{15} can occur, which could lead to single molecule detection[51]. This enhancement arises from an electronic coupling of the molecules with the gold nanoparticles and the nanoparticle's plasmon resonance, which leads to an increase in the Raman signal to the fourth power of the local dielectric field[51]. SERS has been used to differentiate cancerous cells from non-cancerous cells using gold nanorods conjugated to anti-EGFR antibodies[113], and to differentiate unhealthy acidic cells from healthy cells using nanoshells[114]. SERS has also extended to in vivo tests, detecting a tumor as small as 0.03 cm^3 using gold nanoparticles conjugated to ScFv antibodies at a penetration depth of 1-2 cm (Figure 2.5)[100].

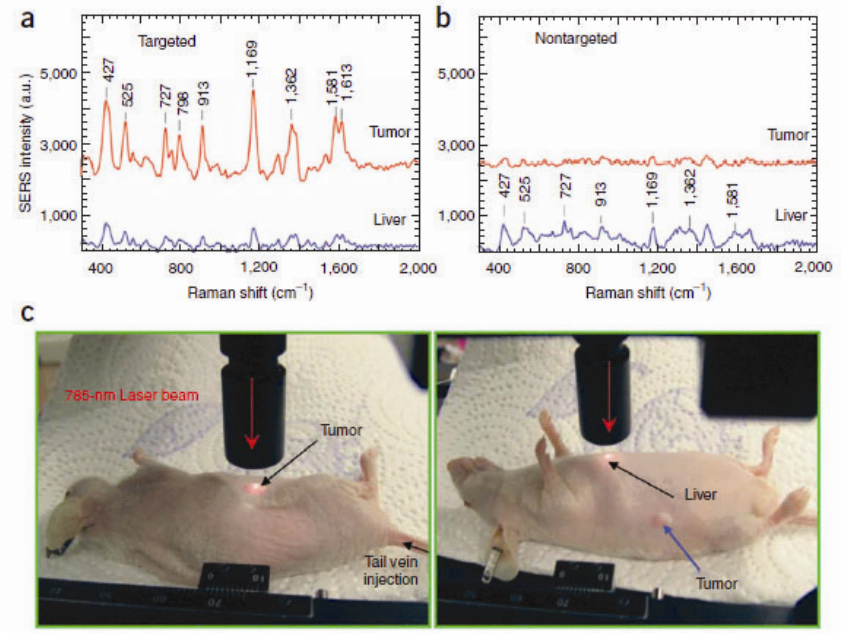

Figure 2.5 SERS of ScFv antibody conjugated gold nanoparticles with Raman reporter, malachite green, injected via tail vein into nude mice bearing head-and-neck squamous cell carcinoma xenograft tumors. SERS spectra from tumor (red spectrum) and liver (blue spectrum) of (a) targeted particles and (b) non-targeted particles were obtained 5 hrs after injection. (c) Photos of the anatomical location of the tumor (left) and the liver (right) are pointed out[100].

2.2.1.4 Photoacoustic imaging

Recently, gold nanoparticles have also been used in photoacoustic (PA) imaging, which is a technique that images tissue absorbers using a pulsed light excitation and ultrasound detection. Developments in PA imaging combined with gold nanoparticles have shown high sensitivity, molecular specificity, and penetration depth in imaging diseases like cancer (Figure 2.6)[115] and cardiovascular disease[116] as well as important structures like blood[117] and sentinel lymph nodes[118] that can provide information about the early onset of these diseases. Even more recently, along with diagnosis, photoacoustic imaging has been used to detect migration of stem cells for therapeutic purposes[119].

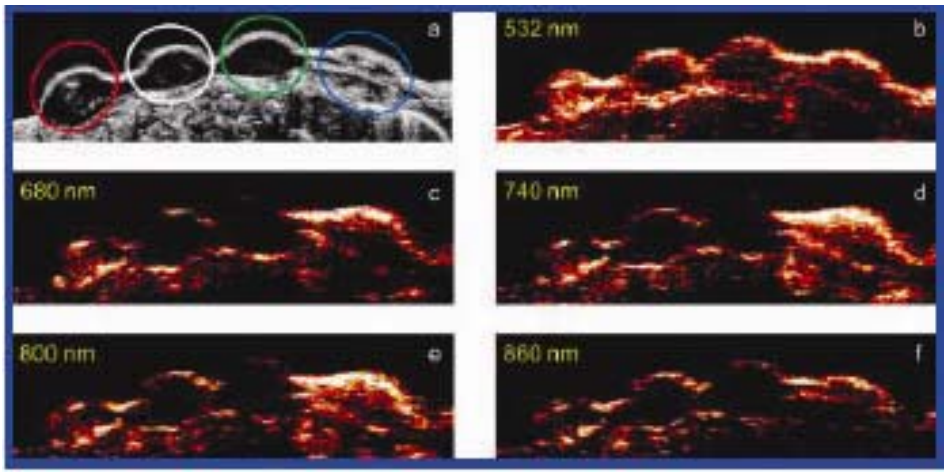

Figure 2.6 Ultrasound (a) and photoacoustic (b-f) images of gelatin phantoms implanted in a mouse ex vivo illuminated at wavelengths 532, 680, 740, 800, and 860 nm, respectively. In (a), the red circle is human epithelial carcinoma cells (A431) treated with anti-EGFR gold nanoparticles, the white circle is cells only, the green circle is cells mixed with non-specific PEGylated nanoparticles, and the blue circle is control NIR dye[115].

2.2.1.5 Other modalities

Other optical imaging modalities that have been used in conjunction with gold nanoparticles to target and image cancer cells include mulitphoton microscopy[120], optical coherence microscopy[121], and third-harmonic microscopy[49].

2.2.2 Clinical diagnostics

Since the 1950's, gold nanoparticles have been used as radioactive labels in vivo. Gold nanoparticles have shown advantages over conventional organic dyes and quantum dots because of reduced toxicity, resistance to photobleaching, unique spectroscopic properties, and surface enhanced effects[51].

One of the most promising uses of gold nanoparticles in clinical diagnoses is enhancing signal from enzyme-linked immunosorbent assays (ELISAs). These types of tests include immunochromatographic test strips, where both the primary and secondary

antibodies are conjugated to gold nanoparticles. This technique has been demonstrated in detecting gonadotropin hormone at 1 pg/mL[122]. Nanoshells have also been used as contrast agents in ELISA-based tests to determine IgG content in whole blood[102]. Gold nanoparticles have also been used to detect nucleic acids of clinical relevance such as single nucleotide polymorphisms (SNPs) and mutations that have been known to lead to diseases such as cancer[123].

Cancer diagnostics have been extensively studied using gold nanoparticles as sensing and imaging agents. Large gold nanoparticles strongly scatter light and when they are immunotargeted to cancer markers such as epidermal growth factor receptor (EGFR), they can be illuminated with a simple laser pointer[48c] or with white light[124] (Figure 2.7).

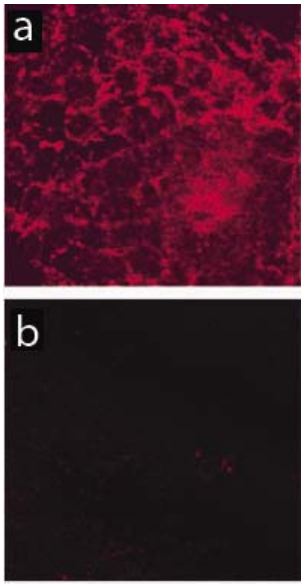

Figure 2.7 Laser scanning confocal reflectance images with 647 nm excitation wavelength of (a) precancerous and (b) normal fresh cervical tissue ex vivo labeled with ant-EGFR gold nanoparticle conjugates[48c].

Other diseases that gold nanoparticles have been used to detect in conjunction with emerging technologies include Alzheimer's disease[125] and HIV[126].

2.2.3 Therapy

2.2.3.1 Photothermal therapy

Laser hyperthermia, or photothermal therapy, uses optical heat to ablate a tumor to avoid the non-specific side effects that traditional methods of therapy suffer from[51]. Absorbing agents such as indocyanine green (ICG) and iron oxide have been used for photothermal therapy of cancer, but these agents provide only small cross sections and thus a large concentration of agents is needed to be effective. Thus, there has been a large interest in using gold nanoparticles to alleviate these problems because gold nanoparticles are considered non-toxic and have high absorption cross sections[51]. After gold nanoparticles are irradiated, they convert light to heat extremely quickly, in about 1 ps[127].

Smaller gold nanoparticles 10-30 nm in size are of optimal size to be delivered to a tumor and when aggregated on a cell's surface, can be irradiated with NIR wavelengths of light, resulting in bubble formation[112b, 128]. SK-Br-3 cancer cells have been photothermally destroyed both in vitro and in vivo using PEGylated nanoshells. The shells cause a local increase in temperature to 37.4 ± 6.6°C at a depth of 2.5 mm for 5 min, using a laser dosage that was 10-25 times less than needed for ICG. More recently, nanoshells have been used to ablate 98% of a prostate tumor in vivo using an 810 nm laser with a 200 nm laser fiber at $4Wcm^{-2}$ [129]. Larson et al. also showed significant photothermal damage using anti-EGFR antibodies conjugated to hybrid gold shell iron oxide core nanoparticles on EGFR-overexpressing cancer cells using a single 400 $mJcm^{-2}$ pulse at 700 nm wavelength, with no effect on cells that were exposed to non-specific PEGylated hybrid nanoparticles (Figure 2.8)[112b].

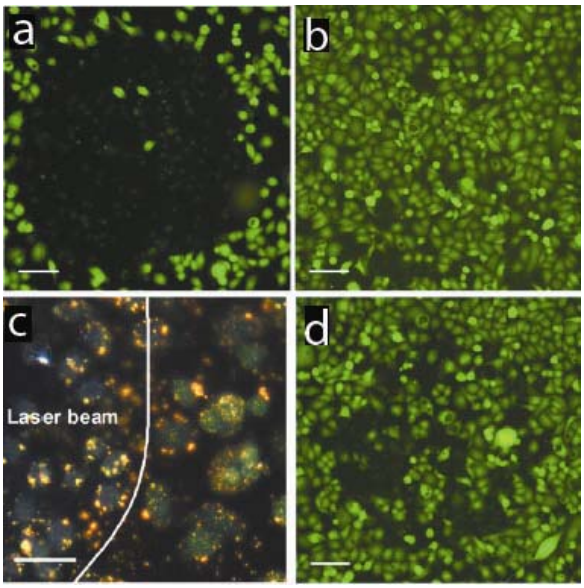

Figure 2.8 Photothermal therapy of MDA-MB-468 breast cancer cells using anti-EGFR hybrid gold nanoparticles. Fluorescence images of cells treated with (a) anti-EGFR hybrid nanoparticles and (b) PEGylated hybrid nanoparticles after one 7 ns 400mJcm^{-2} laser pulse at 700 nm. Green fluorescence is from calcein AM staining that indicates cell survival. (c) Dark-field reflectance images of cells treated with anti-EGFR hybrid nanoparticles after one 7 ns, 400mJcm^{-2} laser pulse at 700 nm. (d) Fluorescence image of cells treated with PEGylated hybrid nanoparticles after six hundred 7 ns, 400mJcm^{-2} pulses at 700 nm. Scale bar is approximately 100 μm in the fluorescence images and 50 μm in the dark-field image[112b].

A NIR absorbing hollow nanoparticle comprised of both silver and gold has shown selective damage to lung cancer cells A549 with a laser power that was significantly reduced compared to the power needed for rods[130].

2.2.3.2 Targeted delivery for therapy and gene therapy

Nanoparticles have also acted purely as delivery vehicles. Nanoparticles carrying a photodynamic therapy agent, phtalocyanine, generated singlet oxygen upon excitation with light, inducing apoptosis and necrosis in tumors[131]. Gold nanoparticles have also been used to deliver DNA, small interfering RNA (siRNA), and drugs through surface

functionalization[62d]. Additionally, concentrating drugs on the surface of nanoparticles can lead to a decrease in non-specific systemic toxicity. A cytokine that can induce apoptosis, tumor necrosis factor (TNF-α), decorated on the surface of 33 nm PEGylated particles maximized tumor damage while minimizing systemic exposure to TNF-α[132]. Gold nanoparticles have also shown to decrease angiogenesis by binding to heparin-binding growth factors and inhibiting the phosphorylation of proteins that are critical for angiogenesis[133]. This inhibition has also been used to image and treat arthritis by reducing the presence of macrophages and monitoring the process with photoacoustic imaging[134]. Gold nanorods have shown to effectively treat antifibrotic disorders by modulating cell-mediated matrix remodeling. Three-dimensional phantoms of collagen and cardiac fibroblasts were treated with polyelectrolyte-coated gold nanorods and a reduced contraction and expression of mRNA-encoding actin and collagen type I were observed[135].

Potential gene therapy applications have also been reported using gold nanoparticles to deliver plasmid DNA via gold-polyethylenimine (PEI) conjugates[136] and negatively charged oligonucleotides[137].

2.2.3.3 Hyperthermia

Radiofrequencies (RF), frequencies of 10 kHz – 900 MHz, have been used for healing purposes during the last century, but only since the 1990's have these frequencies been used to treat tumors in the liver[51]. This technique is currently limited by the need to implant heating needles at the tumor and the inability to monitor the heat generation. Additionally, this therapy has suffered from damage to nearby healthy liver as well as a relatively high observation of recurrence[51]. Recently, gold nanoparticles have been used with RF heating to induce cancer death in a rat using 35 mW of power[138].

Hyperthermia has been demonstrated using not only magnetic nanoparticles, but also with nanoshells that accumulated in a tumor and disrupted the perivasculature[139].

2.3 MULTIMODAL NANOPARTICLES

The future of personalized medicine relies heavily on the future of molecular imaging. Though there are a handful of molecular imaging techniques, no single modality will provide all the information a researcher or physician requires[140]. Current molecular imaging methods used clinically have limitations: optical imaging is difficult to quantify as you delve deep into tissue, magnetic resonance imaging (MRI) has good resolution but low sensitivity, and positron emission tomography (PET) has poor resolution but high sensitivity. Multimodal probes offer the ability to combine the advantages of multiple imaging modalities to enhance the visualization of biological processes and collect data more reliably[140].

Molecular imaging is the ability to see within the body and understand biological processes on the molecular scale[140]. This should allow us to visualize fundamental alterations that molecules undergo in a disease as opposed to visualizing only the endpoint, thus giving us a better understanding of the disease and allowing us to detect the disease earlier. Ideally, agents would allow us to non-invasively monitor processes over time[140]. Molecular imaging has been achieved using inorganic nanoparticles made up of iron oxide, quantum dots, gold, and silica. Because of these nanoparticles' small sizes, they can interact with biological molecules, have readily tunable properties, and potential to be multifunctional.

2.3.1 MRI/Optical

2.3.1.1 Paramagnetic agents

Commercially available MRI contrast agents include Magnevist and Dotarem, which are gadolinium (Gd) chelates. Gd-nanoparticle conjugates with dual MRI/optical contrast have been developed using Gd-lipid-rhodamine nanoparticles, and these particles were found to evenly distribute throughout breast cancer cells[141]. Gd chelates-nanoparticles have also been developed using a dendrimer PAMAM[142] and quantum dots[143]. A Gd-DOTA-silica nanoparticle yielded a high 15000$mM^{-1}s^{-1}$ relaxivity with a 1.4T MRI, and these particles showed promise for in vivo translation because they efficiently cleared through the bladder[143]. These silica nanoparticles have also been doped with fluorophores or metals such as ruthenium to create dual fluorescence/MRI imaging agents[140, 144]. Another triple modality nanoparticle was developed for imaging with photoacoustic imaging, Raman spectroscopy, and MRI. The nanoparticles consisted of a gold core for photoacoustic imaging, a Raman active layer for Raman spectroscopy, and a gadolinium layer for MRI[145].

Along with conventional fluorophores, quantum dots have also been used as optical imaging agents in multimodal imaging. Quantum dots have relatively high absorption cross sections in the Vis and NIR range of 10^{-15} cm^2, which is an order of magnitude higher than NIR fluorophores and thus have shown to be strong photothermal microscopy and photoacoustic agents. Care must be taken, however, to limit toxicity of the quantum dots, whose cores could potentially disintegrate after being irradiated[146]. CdSe/ZnS core/shell quantum dots conjugated to a lipid-based Gd nanoparticle showed relaxivities of 12$mM^{-1}s^{-1}$, which is three times higher than the clinically used Gd-DTPA[147].

Silica nanoparticles doped with quantum dots and paramagnetic lipids showed a quantum yield of 35% and an MRI relaxivity of 14.4 $mM^{-1}s^{-1}$[148]. Silica-quantum dot nanoparticles have also been doped with manganese to yield T1 relaxivity values of $12mM^{-1}s^{-1}$ and a quantum yield of 8.1% in water with NIR two-photon microscopy, with limited toxicity when given to cells. Though this is a promising dual NIR imaging/MRI agent, challenges with this agent are that the synthesis of the agent is complicated and there is a need for post-processing the optical data[149].

2.3.1.2 Superparamagnetic agents

Along with gadolinium, iron oxide nanoparticles have also shown to be useful MRI contrast agents. In contrast to gadolinium, they are superparamagnetic materials and yield a T2 contrast. Commercial iron oxide nanoparticles are Feridex, Resovist, and Combidex, and they have shown to be less toxic than Gd-based agents[41, 150]. One of the first iron oxide nanoparticles used for MRI was a cross-linked iron oxide (CLIO) which consisted of a cross-linked dextran functionalized with amine groups[151]. Fe_2O_3 and Fe_3O_4 have been conjugated to NIR fluorescent dyes such as Cy5.5 and shown to be useful MRI/optical imaging agents for imaging structures such as sentinel lymph node and brain imaging, with low toxicity (Figure 2.9)[151-152].

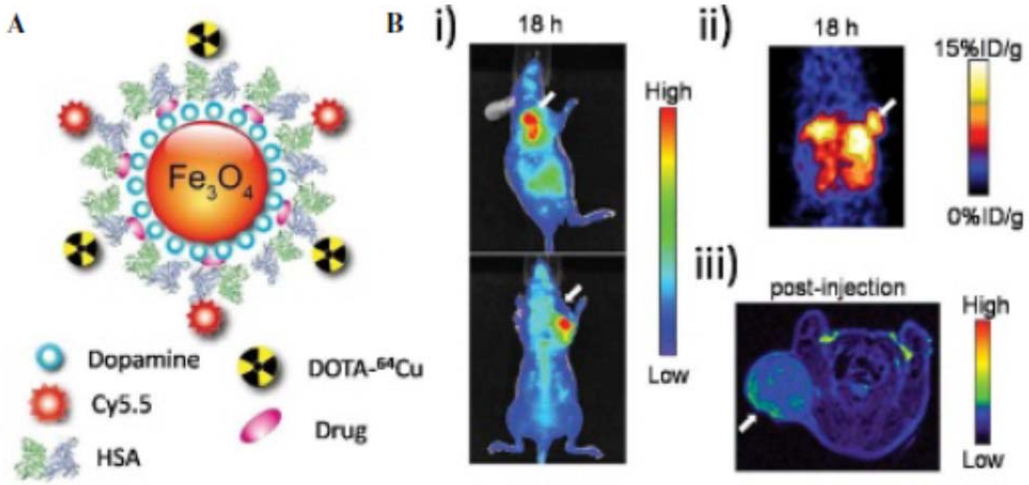

Figure 2.9 Iron oxide nanoparticles conjugated to cu-DOTA and Cy5.5 allow for triple modality imaging with MRI, PET, and NIR fluorescence. (A) Schematic of multimodal nanoparticle. (B) (i) NIR fluorescence, (ii) PET, and (iii) MR images of mice 18 hours after injection of nanoparticles[152b].

Iron oxide has also been paired with gold nanoparticles for optical/MR imaging as well as photothermal therapy of cancer cells using both Fe_2O_3[112b, 112d] and Fe_3O_4[153]. 5 nm gold particles have an absorption cross section that is 3 nm^2, which is two times as high as a common organic fluorophore[154]. Additionally, because of the gold nanoparticles' high absorption cross section, they provide excellent photoacoustic imaging contrast owing to thermoelastic expansion[155]. Gold coated carbon nanotubes (GNTs) have also been developed for both efficient photoacoustic and photothermal signal, resulting in 100 times NIR contrast over control in lymphatic vessels with 300 nm spatial resolution[156]. These GNTs have also been used in combination with PEGylated magnetic nanoparticles to capture circulating tumor cells in vivo via an externally applied magnet and to image the captured cells photoacoustically[157].

2.3.1.3 ^{19}F MRI agents

Quantum dots with perfluorodecalin nanoemulsions have also been developed for dual ^{19}F-based MRI and optical imaging and have been shown to be delivered intracellularly both to phagocytic and non-phagocytic cells[158].

2.3.2 MRI/SPECT

Single photon emission computed tomography (SPECT) involves imaging gamma rays emitting from a nucleus, with the most common isotope being ^{99m}Tc, which has a half-life of six hours. This is long enough for tumor accumulation but short enough to expose the patient to only minimal amounts of radiation. ^{99m}Tc with a phospholipid layer of Gd chelates have been used to reveal tumor neovasculature that was asymmetric and patchy[159].

2.3.3 MRI/PET

Positron emission tomography (PET) detects radiopharmaceuticals that emit positrons when they are activated[140]. PET is very sensitive and MRI has excellent spatial resolution. The difficulty in combining these techniques together, however, is the fact that conventional photomultiplier tubes that are used for PET do not operate in the high magnetic field required by MRI[142]. One way researchers have avoided this complication was to use a fiber optic light guide to direct certain components of the PET to avoid the magnetic field[160]. Another challenge is that MRI typically requires high doses of contrast agent while PET needs only trace amounts[154]. An MRI/PET agent consisted of manganese iron oxide nanoparticles and isotope I^{24} [161]. Manganese showed to have a two to three times higher relaxivity coefficient than iron oxide nanoparticles without manganese.

Recently, a triple modality probe used for PET/MRI/fluorescence consisted of a cross-linked iron oxide-TAT peptide that was cross-linked with aminated dextran for MRI, then attached to lysine fluorescein for optical imaging and DTPA with In for radioactive nuclear imaging[162].

As advances are made in developing these inorganic nanoparticles, their biodistribution, biocompatibility, and reproducibility must be characterized[154]. The next step is to combine these multimodal probes with a therapeutic component. Advances in instrumentation will also be necessary to have these agents be widely used.

2.4 CLEARANCE OF NANOPARTICLES FROM THE BODY

New nanoparticles and nanoparticle conjugates are constantly being developed, and their success in vivo depends critically on their biocompatibility and clearance properties[44]. Because nanoparticles often contain heavy metals, they could pose a toxicity concern if they are retained in vivo for a long time. Additionally, they could interfere with diagnostic imaging tests conducted over time. Nanoparticles with optimal clearance kinetics would minimize risks associated with toxicity by minimizing the exposure of these materials to the body.

Properties known to affect clearance are material, shape, size, and surface chemistry[44]. After intravenous administration, nanoparticles encounter blood cells, platelets, and a variety of proteins[44]. If a particle traveling in the blood is opsonized, the effective particle size increases and this is inversely related to renal filtration. Blood vessel are lined with an endothelial layer which serves as a selective barrier for transporting macromolecules between the vascular region and the extravascular space[163]. This barrier has an effective pore size of 5 nm[164]. Thus, molecules with a diameter of 5 nm or less rapidly achieve equilibrium with the extravascular extracellular space (EES),

while larger particles cannot pass the endothelial barrier and have a longer blood circulation time. In comparison, lymphatic vessels are slightly more permeable, allowing particles < 6 nm to pass[165].

Modifying the surface of a nanoparticle is a common method to alter their in vivo clearance kinetics, such as with the common procedure of PEGylating the surface of a nanoparticle to increase circulation as well as particle elimination[166].

2.4.1 Clearance through the kidney

The desired excretion path for a nanoparticle is through the kidneys because there is minimal intracellular catabolism taking place in the kidneys, and thus there is minimal chance of retention. In contrast, the hepatobiliary route involves modification by intracellular enzymes[44]. Nanoparticles flowing through the glomerular capillary wall of a kidney will enter filtration slits which have effective pore sizes of about 4.5-5 nm[167]. Typically, molecules of < 6 nm are filtered, but 8 nm are not. Molecules 6-8 nm can be filtered if their surface charge is favorable[44]. For example, insulin, with a hydrodynamic diameter (HD) of 3 nm, achieves 100% filtration, with a half-life of only 9 minutes[168]. But an Fab fragment of an antibody, with a HD of 6 nm, achieves only 9% filtration with a serum half-life of 28 minutes[169], while whole antibodies of HD 11 nm have a serum half-life of days. A less researched path of renal filtration is excretion through resorption of substances to the proximal tube of the functional unit of the kidney, the nephron. This is the path that glucose takes to be excreted in urine. Few studies have been done to characterize this path, but Kobayashi and colleagues have shown that polyamine dendrimers can undergo this proximal tube resorption[170].

2.4.2 Clearance through the liver

When nanoparticles do not undergo renal clearance, they most likely undergo hepatobiliary clearance. One of the liver's main functions is to clear the body of particles 10-20 nm in size which are of the size of viruses[164], and even though this process of uptake by the liver is quick, the process of excretion is interestingly very slow[164]. In the liver, particles undergo a breakdown and are excreted through bile[44].

Phagocytic Kupffer cells in the liver have stellated branches that are mechanical traps for unwanted substances in blood like opsonized particles[44]. These Kupffer cells are part of the reticuloendothelial system (RES) and remove particles via degradation. If particles are not degraded, they will remain in the body. The turnover rate of Kupffer cells has been shown to be 21 days[171]. Hepatocytes also play an important role in clearing foreign particles from the bloodstream through endocytosis and enzymatic breakdown. The capacity of this hepatocytic breakdown, however, is much less than in Kupffer cells[44].

2.4.3 Nanoparticle types

2.4.3.1 Dendrimers

Larger-sized nanoparticles were first used in magnetic resonance (MR) angiography when small gadolinium (Gd) chelates were cleared too quickly from the blood to be useful as imaging agents[142]. Thus, dendrimers served as delivery vehicles of MR contrast agents to increase circulation time[172]. Because commonly used dendrimers such as PAMAM and poly(propyleneime) are usually 3-10 nm, their major clearance route is through the kidneys[173]. 60% of dendrimers DAB-G3-DAB-G2 and PAMAM-G2-based contrast agents clear from the body in 15 minutes[174]. Interestingly, even though the DAB dendrimer accumulates in the liver more than the PAMAM dendrimer, the DAB

clears faster, which could be because DAB has a shorter interior structure than PAMAM[174].

2.4.3.2 Inorganic biodegradable nanoparticles

Biodegradable macromolecular structures have been conjugated to low molecular weight Gd-chelates to yield longer vascular retention times and then over time degrade to allow for renal filtration[175]. Biodegradable polydisulfide Gd (III) complexes have been developed to serve as long-circulating carriers and can also degrade via endogenous thiols (glutathione, cysteine, and homocysteine), which have been known to exchange with disulfides[176].

2.4.3.3 Quantum dots

Quantum dots of 5.5 nm or less showed clearance from a mouse body at 50% in four hours (Figure 2.10)[164]. The serum half-life of these quantum dots increased linearly with increasing size from 4.36 – 8.65 nm. The surface charge of the quantum dots played a large role in protein adsorption. Anionic (DHLA-coated) and cationic (cysteamine-coated) quantum dots led to protein adsorption, increasing the HD > 15 nm, but zwitterionic coatings (cysteine) allowed the quantum dots to remain small, water soluble, and free from protein adsorption after four hours of incubation with 100% serum at 37°C. Thus, a zwitterionic coating was chosen as the optimal surface coating for renal clearance. Neutral PEGylated quantum dots did not lead to protein adsorption but could not be synthesized smaller than 10 nm.

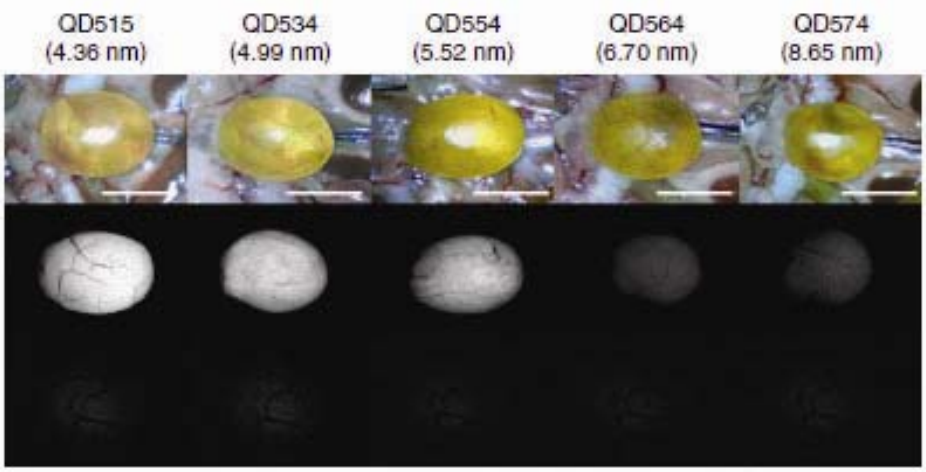

Figure 2.10 Exposed mouse bladders 4 hours after intravenously injecting varying sizes of quantum dots. Top row: Color video of bladders injected with increasing sizes of quantum dots (left to right). Middle row: Fluorescence images of top row. Bottom row: Fluorescence images of unininjected control bladder. Scale bar is 1 cm[164].

Another study confirmed that surface coating played a major role in clearance. Fischer and colleagues saw that conjugating bovine serum albumin (BSA) to quantum dots (> 8 nm) quickened hepatobiliary clearance compared to unconjugated quantum dots[177].

2.4.3.4 Carbon nanoparticles

Conjugates of Gd and C60 showed urinary excretion one hour after injection[46]. Single walled carbon nanotubes (SWCNTs) showed improved relaxivity values compared to conventional MRI agents and also possessed intrinsic NIR fluorescence along with distinct Raman signatures for multimodal imaging[178]. These SWCNTs have shown fast particle clearance with a particle half-life of three hours[179].

2.4.3.5 Liposomes

Reports have shown that liposome clearance is dominated by opsonins from the complement system[180]. Thus, anionic and cationic liposomes are typically found in the liver[181]. Increasing liposomal size has shown to increase clearance from blood into the liver[180b]. Compared to free contrast agents, liposomal contrast agents for computed tomography and MRI have shown to increase circulation half-life substantially, to ~18 hours[182].

2.4.3.6 Gold nanoparticles

1.9 nm gold particles in mice have shown half-lives of 2-10 minutes. After 15 minutes post injection, the highest gold content was found in the kidneys, and after five hours, 77.5% of the gold had been cleared[183]. A study looking at a wide range of gold nanoparticle sizes 10-250 nm in diameter showed that 24 hours after injection, 10 nm particles were found mostly in the liver, blood, and spleen as well as throughout many other organs, while in contrast, 50-250 nm particles were found exclusively in the liver, spleen, and blood[94].

Gold-dendrimer PAMAM conjugates were synthesized in sizes of 5-22 nm with different surface charges: positive, negative, and neutral, and showed that renal clearance occurred for 5 nm particles but decreased as nanoparticle size increased. Regarding surface charge, renal clearance was maximum for positively charged particles with 36% injected dose of 5 nm positively charged particles in urine after five days. In contrast, negatively and neutral-charged 5 nm particles showed only ~8% injected dose in urine in the same time frame[184].

Another study showed that 2 nm glutathione capped gold particles were cleared renally, with 50% of the injected dose found in the urine after 24 hours. In comparison, cysteine, citrate, and PEGylated particles showed a much lower renal clearance[185].

2.4.3.7 Magnetic nanoparticles

Magnetic nanoparticles have shown to be taken up by macrophages and are thus good MRI markers for inflammatory diseases[186]. Intravenous injection of magnetic nanoparticles have shown to clear via the reticuloendothelial system (RES), with blood half-lives ranging from 1-36 hours[186].

Biodistribution has shown to depend on size, with ultra-small superparamagnetic iron oxide (USPIO) nanoparticles distributing in both lymph nodes and the RES, while larger SPIOs distribute only in the RES. Coatings have shown to play a large role in distribution as well, where magnetic nanoparticles coated in dextran showed a higher accumulation in a liver (75% of the injected dose) than magnetic nanoparticles coated in oleic acid and pluronic polymer (55% injected dose)[187].

Another study showed that a 30 nm USPIO nanoparticle coated in low molecular weight dextran led to urinary excretion of about 89% injected dose after 56 days. The iron was found to be incorporated into the body store of iron in the form of hemoglobin[188].

2.4.3.8 Silica nanoparticles

Luminescent mesoporous silicon nanoparticles 126 nm in diameter with 5-10 nm pore sizes have been developed for in vivo imaging and have been shown to degrade into biocompatible, renally clearable components of orthosilicic acid $Si(OH_4)$[189]. These particles completely cleared from a mouse in 4 weeks[189b].

Studies have shown that optimal characteristics of nanoparticles for efficient clearance must be < 6 nm in size with either a zwitterionic or cationic surface charge[44]. Because of the wide variety of nanoparticles being developed, however, agent-specific studies must be determined to ensure minimal toxicity and effective clearance.

Chapter 3: Plasmonic Nanoparticles for Treating Cancer

3.1 INTRODUCTION

The epidermal growth factor receptor (EGFR) is overexpressed in 80% of all non-small cell lung cancer cells and is associated with poor survival[190]. Since the early 2000's, EGFR-targeted inhibitors have been used as therapeutic molecules in the clinic[191]. These therapeutic molecules, however, have only induced modest increases in patient survival on average, compared to standard non-targeted treatments. This is one of the reasons why lung cancer remains the leading cause of cancer-related deaths for both men and women[1]. To overcome this limitation in targeted therapeutic efficacy, we employed nanoparticles as an efficient delivery vehicle for the therapeutic molecules and a bright signal to monitor the therapeutic molecules' interactions with target cells. This chapter will detail studies involved in analyzing the interactions between therapeutic molecules conjugated to the surface of hybrid core/shell iron oxide/gold nanoparticles and implications for diagnosing and treating cancer. A majority of this chapter was recently published in the journal PLoS One[192].

3.1.1 Nanoparticles for treating cancer

Recently, nanoparticles have shown to enhance the effect of traditional therapies as well as provide therapy based on their own intrinsic properties. Nanoparticles provide an attractive platform for therapeutic applications because of their small size, which is similar to biological molecules such as viruses and proteins that can evade the reticuloendothelial system (RES) and gain intracellular access.

Additionally, nanoparticles can be composed of multiple materials (organics and inorganics) and can provide a surface for conjugating a variety of biomolecules such as antibodies, nucleic acids, and polyethylene glycol (PEG). Plasmonic nanoparticles also

have very unique optical properties. Plasmonic gold nanoparticles have a very high absorption cross section, and thus have been used for photothermal therapy[112b, 127a, b, 127d, e, 128, 193] and hyperthermia-induced killing of cancer cells[138-139]. Because of their small size and thus large surface area to volume ratio, NPs have also acted as delivery vehicles for drugs[62d, 131-132]. More details of these studies can be found in Chapter 2.2.3.

3.1.2 Multivalency

Targeted therapeutics have shown only modest increases in treating cancer[194]. Two ways that can improve on this disappointing therapeutic effect is to monitor the therapeutic molecule in the body to determine as early as possible if the therapeutic molecule is arriving at its desired destination, and to increase the binding affinity of these therapeutic molecules to its target. Both these goals can be accomplished using a single entity: nanoparticle technology.

Plasmonic nanoparticles such as gold nanoparticles have already been shown to be robust contrast agents in optical imaging modalities which have high spatial resolution that can be monitored over time[195]. Thus, gold nanoparticles can serve as bright monitors of therapeutic molecules in vivo.

Increasing the binding affinity of therapeutic molecules can be accomplished by increasing the valency of the therapeutic molecule. In 1972, Crothers and Metzger calculated an increase in observed equilibrium constant for forming a bond between an antibody and its antigen as antibody valency increased[196]. Since then, molecules have shown to target more effectively if the valency of the molecule is increased[197]. In the early 2000's, this multivalent enhancement was exploited to show that polyvalent inhibitors were able to bind to toxins and inhibit them from binding to their target cells more effectively than univalent inhibitor molecules. In 2000, Kitov and colleagues

showed that an oligovalent carbohydrate ligand of less than 10 nm bound 1-10 million times more strongly to Shiga-like toxins than univalent P^k trisaccharides, and more effectively than the toxins to their target, showing that multivalent ligands can act as extremely potent inhibitors of toxin[198]. Similarly, a year later, Mourez and colleagues showed that by attaching an anthrax-inhibiting peptide to a polyacrylamide backbone, they achieved a 7,500 fold increase in inhibition of anthrax per peptide over free peptide[199].

Multivalency has also been used to increase targeting to cancer cells. Folic acid has been used as a targeting agent on polymeric nanoparticles and showed an increased uptake in cancer cells than free folic acid[200]. To quantify this binding avidity, Hong and colleagues decorated dendrimer nanoparticles with folate molecules and showed an enhanced dissociation constant of multivalent nanoparticles compared to free folate, ranging from 2,500-170,000 times for increasingly multivalent particles[201]. An in vivo study showed that by decorating 26 nm gold nanoparticles with tumor necrosis factor (TNF), a decrease in tumor size was obtained compared to free TNF[202]. Moreover, these type of conjugates showed less systemic toxicity than free TNF[203]. More recent studies have shown that there is an optimal density of targeting ligand that can be decorated on the surface of a nanoparticle to maximize targeting[204]. Poon and colleagues determined that an optimal density of 3.1 folate groups per micelle led to the highest uptake of cells overexpressing the folate receptor, compared to more densely and less densely packed folate groups. Each micelle type had the same total number of folates per micelle.

Thus, many studies have shown that multivalent molecules can lead to an enhanced binding and effect on their targets compared to free molecules.

3.2 MATERIALS AND METHODS

3.2.1 Cell culture

Human non-small cell lung cancer (NSCLC) cells (H1299, H1819, H1975, H3255 HCC827) were a generous gift from Dr. John D. Minna (Department of Internal Medicine and Pharmacology, Hammon Center for Therapeutic Oncology Research, The University of Texas Southwestern Medical Center, Dallas, Texas). NSCLC cells (H520), lung fibroblasts (MRC-9 and WI38), and normal human bronchial epithelial (NHBE) cells were purchases from American Type Culture Collection (Manassas, VA). All cells were cultured in RPMI 1640 medium (GIBCO, Grand Island, NY) or MEM Alpha (GIBCO) supplemented with 10% FCS (Hyclone, Logan, UT), 2mM L-glutamine, penicillin (50 U/mL), and streptomycin (100 μg/mL).

3.2.2 Synthesis and conjugation of nanoparticles

The protocol for preparing colloidal core/shell iron oxide/gold (AuFe) nanoparticles has been previous described in a paper by Lyon and colleagues (Figure 3.1)[205]. First, iron seeds were synthesized by coprecipitation of Fe(II) and Fe(III) chlorides (1:2 ratio) with 1.5M NaOH as the reductant. The colloid was magnetically decanted, washed in DIUF water (18 MOhms) via centrifugation for 2 hours at 1500 x g, and resuspended in a stabilizer – 0.1M tetramethylammoinum hydroxide (TMAOH). The resulting colloidal suspension of 9 nm magnetite (Fe_3O_4) nanoparticles was oxidized in boiling 0.1M HNO_3 followed by washing in 0.01M HNO_3 and resuspension in 0.1M TMAOH. The final colloidal suspension had ~36 mM, γ Fe_2O_3 at pH 12 with a particle diameter of *ca.*9 nm. $N(CH_3)^{4+}$ and OH^- ions stabilized the suspension, preventing aggregation. A gold coating was formed by reducing $HAuCl_4$ on the surface of the iron using an iterative hydroxylamine process under UV-Vis spectroscopy monitoring that

showed a gradual increase in plasmon resonance peak characteristic for spherical gold nanoparticles. Right after synthesis, AuFe nanoparticles exhibited a jagged appearance because of the fact that Au^{3+} ions initially reduce onto specific sites of the iron oxide nanoparticles, and over time, will fill the bare space and create a more uniform surface[205].

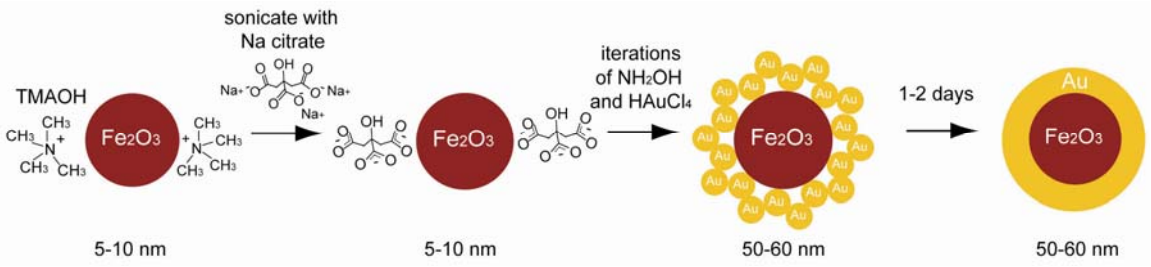

Figure 3.1 Schematic of process of coating iron oxide nanoparticle (5-10 nm) with a gold shell, yielding ~50 nm total diameter[205].

The antibody conjugation procedure was followed as previously described in a paper by Kumar and colleagues (Figure 3.2)[67]. Briefly, monoclonal antibodies were attached to the gold surface via a linker (SensoPath Technologies) that consisted of a short polyethylene glycol (PEG) chain terminated at one end by a hydrzide moiety, and at the other end by two thiol groups. First, antibodies at a concentration of 1 mg/mL were exposed to 10 mM $NaIO_4$ in a 40 mM HEPES pH 7.4 solution for 30-40 minutes at room temperature, thereby oxidizing the hydroxyl moieties on the antibodies' Fc region to aldehyde groups. The formation of the aldehyde groups was colorimetrically confirmed using a standard assay with an alkaline Purpald solution. Then, excess hydrazide-PEG-thiol linker was added to the oxidized antibodies and was allowed to react for 20 minutes. The hydrazide portion of the PEG linker interacts with aldehyde groups on the antibodies to form a stable linkage. In this procedure, a potential loss of antibody function is avoided because the linker cannot interact with the antibody's target-binding region, which

contains no glycosylation. The unreacted linker was removed by a 100,000 MWCO centrifugal filter (Millipore). After purification, the modified antibodies were mixed with nanoparticles in 40 mM HEPES (pH 7.4) for 20 minutes at room temperature. During this step, a stable bond is formed between the gold surface and the linker's thiol groups. Subsequently, 5% by volume of 10^{-5} M 5kD methoxyPEG-SH (Creative PEGWorks) in water was mixed for 5 minutes with antibody/nanoparticle conjugates to cap remaining bare surfaces of nanoparticles. Then, 2% by weight PEG (Sigma-Aldrich) solution was washed twice at 1500 x g for 20 minutes. Final conjugates were resuspended in 2% PEG in PBS.

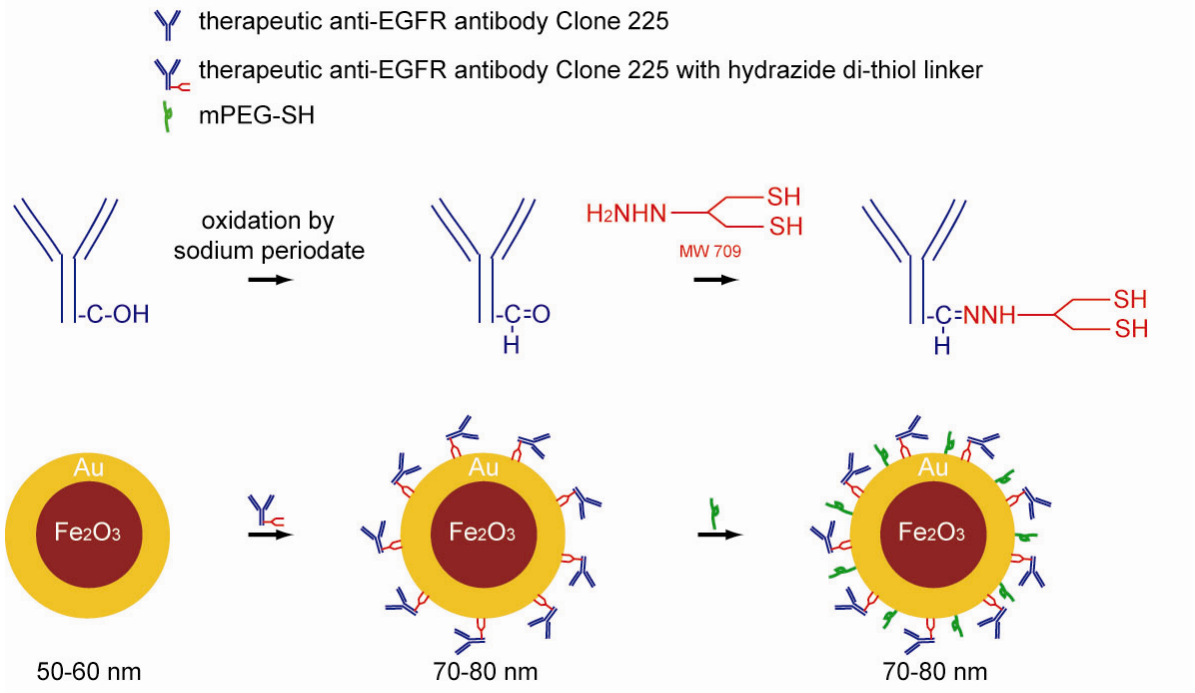

Figure 3.2 Schematic of antibody conjugation to nanoparticle surface. Top row: Dithiol linker is covalently attached to an antibody only on Fc portion of the antibody. Bottom row: Antibody+linker attached to nanoparticle surface via the dithiol linker, leaving the Fab targeting portion of the antibody free.

For varying the density of Clone 225 antibodies on the surface of the nanoparticles (Figure 3.3), a fluorescence technique was used. Nanoparticles were conjugated with anti-EGFR antibodies [Clone 225 monoclonal antibody, (host mouse; Sigma-Aldrich, St. Louis, MO)], anti-rabbit IgG monoclonal antibody (Clone RG-16, Sigma-Aldrich, St. Louis, MO) or with a mixture of the two antibodies at ratios of anti-EGFR:anti-rabbit Abs of 1:0, 1:1, 1:3, 1:10, 1:40, and 0:1. To achieve different antibody ratios at the surface of the nanoparticles, antibodies were pre-mixed at the desired ratio before adding to the nanoparticle suspension. The composition of Clone 225 and anti-rabbit IgG antibodies on the surface of the nanoparticles was verified using fluorescent assay. Clone 225 antibodies and anti-rabbit antibodies were labeled using Alexa Fluor 488 and Alexa Fluor 594, respectively. Then, calibration curves were measured to determine the concentration of labeled antibodies using fluorescent intensity. The fluorescent intensities of antibody solution at the excitation/emission wavelengths of the two Alexa fluorophores were measured at the concentration that was used for conjugation with nanoparticles and were compared with fluorescence intensities of the supernatant after nanoparticle/antibodies conjugates were spun down. The ratio of the difference in signal between the pre- and post-conjugation intensities was calculated and was used to confirm the composition of both antibodies on the surface of the nanoparticles.

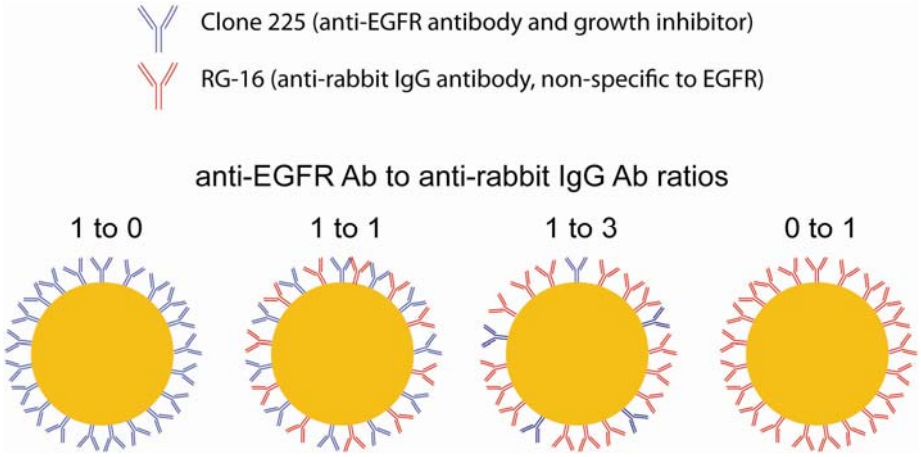

Figure 3.3 Schematic of nanoparticles with varying ratios of therapeutic anti-EGFR antibodies (blue antibodies) to nonspecific anti-rabbit IgG antibodies (red antibodies).

3.2.3 Cell viability assay

The cytotoxic effect of Clone 225-nanoparticles (Clone 225-NP) on NSCLCs and normal cells was determined by using a trypan blue dye exclusion assay. Cancer or normal cells were seeded at 1 or $2x10^5$ cells/well in 6-well plates and incubated overnight at 37°C. The cells were then incubated for 72 hours with/without IgG-NP ($6x10^9$ particles), Clone 225-NP ($6x10^9$ particles), or Clone 225 antibody (0.0065 µg/mL). After the cells were collected by trypsinization, they were stained with trypan blue, and the viable cells in each well were counted. The viability of the untreated cells (the control) was considered 100%. Survival fraction were calculated from the mean cell viability of the treated cells over control and the relative difference in cell number expressed as percent of cell killing over control.

3.2.4 Apoptosis detection assays

Tumor cells that were untreated or treated with Clone 225 antibody, IgG-NP, or Clone 225-NP were collected at 72 hours after treatment, fixed with 70% ethanol, and stained with 10% propidium iodide solution (Roche cellular DNA flow-cytometric

analysis reagent set: Indianapolis, IN) according to the manufacturer's instructions. DNA content was analyzed with a FACScan flow cytometer (Becton Dickinson) as previously described in a paper by Ramesh and colleagues[206]. Data were analyzed with the manufacturer's CellQuest software.

3.2.5 Autophagy detection assay

Using the GFP-LC3 expression vector (LC3 cDNA kindly provided by Dr. N. Mizushima (Department of Physiology and Cell Biology, Tokyo Medical and Dental University), the involvement of LC3 in tumor cells treated with control IgG-NP cells were transfected with the GFP-LC3 expression vector using FuGENE 6 transfection reagent (Roche Applied Science). After overnight culture, cells were treated with IgG- or Clone 225-NP fixed with 4% paraformaldehyde, and examined under an Axioskop 40 fluorescence microscope. To quantify autophagic cells after treatment, we counted the number of autophagic cells among 100 GFP-positive cells.

3.2.6 Cell cycle analysis

HCC827 cells were treated with three difference concentrations (1.5, 2.44, and 3.55 ng/mL) of free Clone 225 antibodies or Clone 225-NP (0.6, 1.2, and $2.4x10^{10}$ particles). The amount of free Clone 225 antibody added was at equimolar concentrations with antibodies attached to nanoparticles. Untreated cells served as controls. At 72 hours after treatment, cells were harvested and the number of cells in the sub-G_1 phase of the cell cycle was determined by DNA flow-cyotmetric analysis[206].

3.2.7 Western blotting

Untreated or treated cells were lysed in extraction buffer and the soluble proteins were isolated as previously described in a paper by Yokoyama and colleagues[207]. Protein concentrations were estimated using a protein assay (Bio-Rad, Richmond, CA), and

proteins were separated by sodium dodecyl sulfate-7.5 to 15% polyacrylamide gel electrophoresis (SDS-PAGE) and transferred electrophoretically to Hybond-P membrane (Amersham, Piscataway, NJ). The membrane was subjected to Western blotting using anti-LC3B antibody (1:5,000 dilution), anti-PARP antibody (1:1000 dilution; Cell Signaling Technology, Beverly, MA), anti-phospho/total-EGFR antibody (1:500 dilution; Santa Cruz Biotechnology, Santa Cruz, CA), anti-phosphorylated/total-AKT, p38 MAPK, and p44/42 MAPK antibodies (1:1000 dilution; Cell Signaling Technology), and mouse anti-β-actin antibody (1:500 dilution; Sigma-Aldrich). Anti-LC3 antibody was generated as previously described[208]. Immunoreactive proteins were detected using an enhanced chemiluminescence reagent (Amersham) according to the manufacturer's instructions.

3.2.8 TEM of cells

HCC827 cells were seeded onto 6-well plates ($1x10^5$ cells/well) and were treated with Clone 225 antibody for 72 hours, IgG-NP or Clone 225-NP ($6x10^9$ particles) for 48 or 72 hours and then fixed with a solution containing 3% glutaraldehyde plus 2% paraformaldehyde in 0.1M cacodylate buffered tannic acid, postfixed with 1% buffered osmium tetroxide for 30 minutes, and stained en bloc with 1% Millipore-filtered uranyl acetate. The samples were dehydrated in increasing concentrations of ethanol, infiltrated, and then embedded in Poly-bed 812 medium. The samples were polymerized in a 60°C oven for 2 days. Ultrathin sections were cut in Leica Ultracut microtome (Leica, Deerfield, IL), stained with uranyl acetate and lead citrate in Leica EM Stainer, and examined with a JEM 1010 transmission electron microscope (JEOL, USA, Inc., Peabody, MA) at an accelerating voltage of 80 kV. Digital images were obtained using AMT imaging system (Advanced Microscopy Techniques Corp., Danvers, MA). To

quantify autophagic cells after treatment, we counted the number of autophagic cells per 100 mm^2 cytoplasm, as previous described[209].

3.2.9 Optical imaging

NSCLC cells and normal cells were resuspended in phenol-free RPMO medium and were seeded in two-well chamber slides. These cells were treated with IgG-NP or Clone 225-NP in the absence or presence of free unbound Clone 225 antibody (2 μg/mL). At 24 hours after treatment, cells were washed, fixed in 1% paraformaldehyde, and imaged using dark-field (DR) reflectance microscopy. All DR images were acquired using Leica, DM6000 microscope equipped with 20x DR objective and Xenon lamp white light illumination.

Confocal images were acquired with a Leica SP2 AOBS confocal microscope using a 63x oil immersion objective, 1.4 NA (Leica Microsystems, Bannockburn, IL). Images were taken every 0.25 μm with a total depth of 55 μm. A 633 nm red HeNe laser was used for detection of nanoparticles in reflectance mode and a UV 350 nm laser excitation was used to measure DAPI fluorescence. A 3D rendering of the confocal images was obtained using the volume rendering program Voxx (Indiana Center for Biological Microscopy).

3.2.10 Immunohistochemistry of EGFR expression

HCC827 cells ($2x10^3$) seeded in two-well chamber slides were treated with IgG-NP or Clone 225-NP ($2x10^9$ particles). At 30 minutes after treatment, chamber slides were washed in phosphate buffered saline (PBS), fixed in 0.1% glutaraldehyde and subjected to immunohistochemical staining using monoclonal antibodies against human phosphorylated and total EGFR (Santa Cruz Biotechnology) and Vectastain kit (Vector laboratories, Burlingame, CA). Untreated cells served as controls. The expression of

phosphorylated and total EGFR in cells after NP treatment was captured by bright-field microscopy and reduction in phosphorylated EGFR determined by semi-quantitative analysis.

3.2.11 Statistical analysis

Data are expressed as means and 95% CI. The statistical significance of the differences in the in vitro antitumor effects of Clone 225 antibody, IgG-NP, and Clone 225-NP was determined by using Student's two-tailed t test.

3.3 RESULTS

3.3.1 Nanoparticle characterization

The process of synthesizing the nanoparticles was characterized with UV Vis and TEM (Figure 3.4).

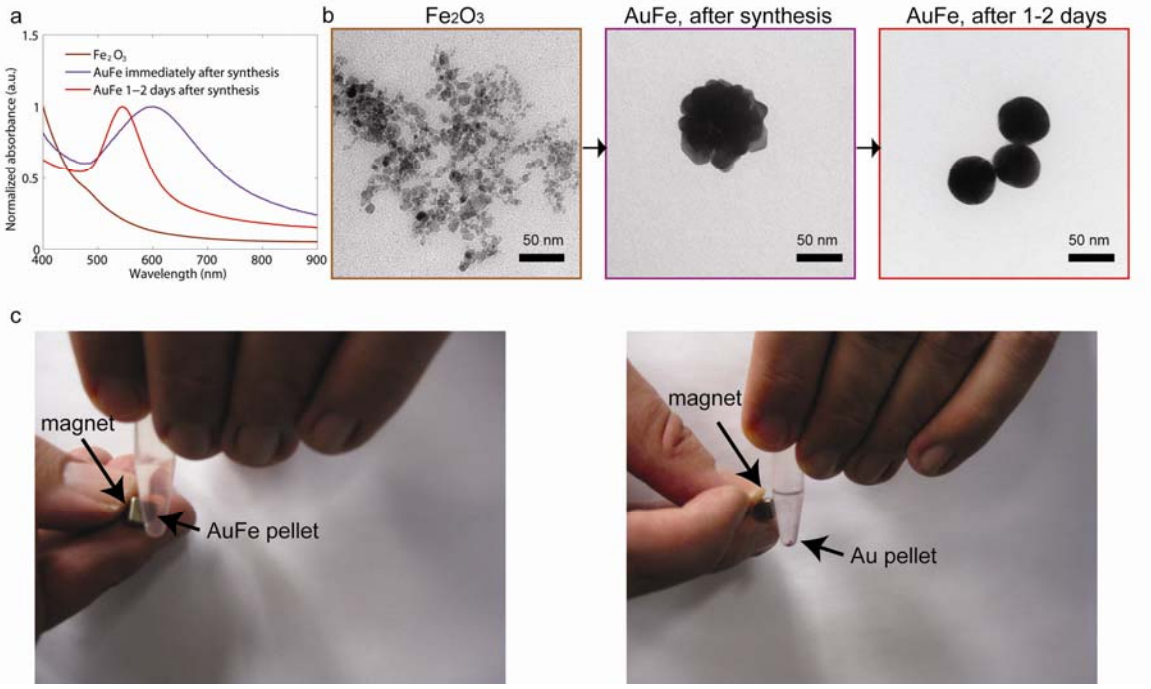

Figure 3.4 Monitoring synthesis of core/shell iron oxide/gold nanoparticles. (a) UV-Vis spectra of iron oxide nanoparticles (brown curve), AuFe right after synthesis (red curve) which has a jagged appearance owing to the fact that the Au^{3+} ions initially reduce onto specific sites of the iron oxide nanoparticles, and then over time, the gold fills the surface, and AuFe after 1-2 days (purple curve). (b) Left to right: TEM images of iron oxide nanoparticles, AuFe right after synthesis, and AuFe 1-2 days after synthesis. (c) Left image shows AuFe nanoparticle pellet being manipulated by a magnet, while in the right image, solid Au nanoparticle pellet cannot be manipulated, demonstrating magnetic properties of the AuFe nanoparticles.

The nanoparticles with and without conjugated antibodies were characterized for size and charge using UV Vis spectroscopy, transmission electron microscopy (TEM), dynamic light scattering (DLS), and zeta potential measurements. UV Vis spectroscopy

revealed a slight red shift in the spectrum after conjugating antibodies to the surface (Figure 3.5). This red shift occurs because of a local change in index of refraction caused by the conjugation of the antibody.

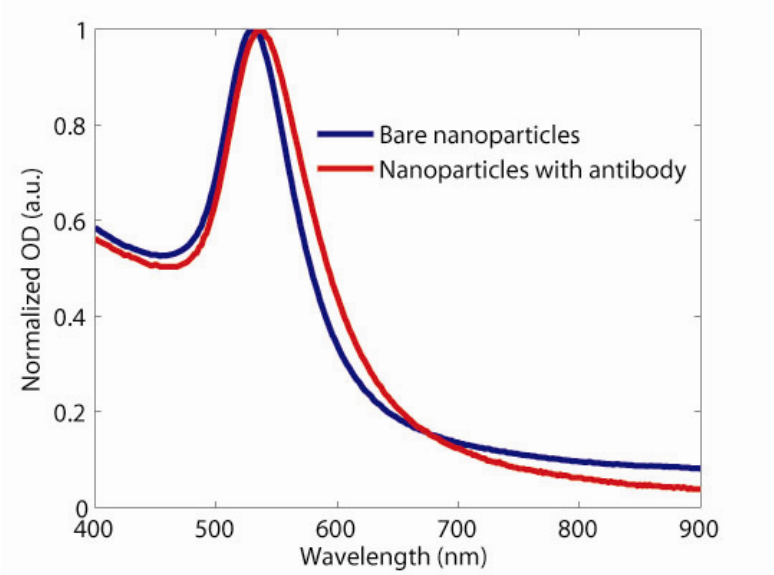

Figure 3.5 UV Vis spectra of bare AuFe nanoparticles and antibody conjugated AuFe. Conjugated nanoparticles spectrum is slightly red-shifted compared to bare nanoparticles because of a local change in index of refraction.

TEM, DLS, and zeta potential measurements are summarized in Figure 3.6. TEM analyses showed that the gold coated iron oxide nanoparticles have sizes of 51±13 nm before and 54±11 nm after antibody conjugation. No apparent change in the sizes of nanoparticles in TEM images is expected as antibody coating does not result in an electron dense layer that would be visible in TEM. DLS measurements showed an increase in nanoparticle sizes from 51±25 nm to 73±35 nm after conjugation of antibodies; this result is consistent with our previous measurements of nanoparticle/antibody conjugates[112d]. Antibody conjugation also resulted in an increase of

surface charge from -53±3 mV to -29±1 mV as antibody and PEG molecules replaced citrate ions from the surface of the citrate stabilized AuFe nanoparticles.

A)

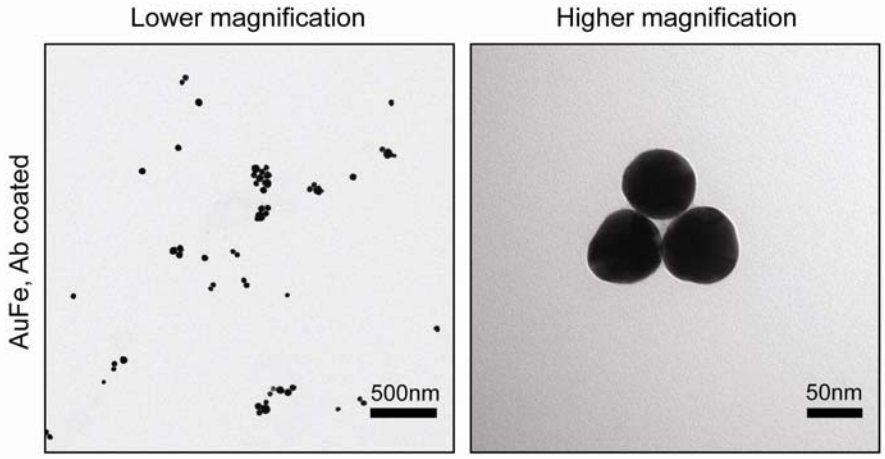

B) TEM (n = 96 measurements)

	AuFe, citrate coated	AuFe, Ab coated
Size (nm)	51.3 ± 12.6	53.8 ± 11.4

C) DLS, volume distribution (n = 3 measurements)

	AuFe, citrate coated	AuFe, Ab coated
Size (nm)	51 ± 3	73 ± 35

D) Zeta potential (n = 5 measurements)

	AuFe, citrate coated	AuFe, Ab coated
Zeta potential (mV)	-53.21 ± 3.48	-28.76 ± 1.19

Figure 3.6 TEM, DLS, and zeta potential measurements of AuFe nanoparticles. (A) Low magnification (left) and high magnification (right) TEM images of antibody (Ab) conjugated AuFe nanoparticles. (B) Size distribution of AuFe nanoparticles before and after Ab conjugation reveal nanoparticles size of ~50 nm. There is little change in size before and after antibody conjugation as measured by TEM because an Ab is not an electron dense material and thus provides little contrast in TEM image (n= at least 96 particles). (C) DLS measurements, volume distribution of AuFe nanoparticles before and after conjugation with Abs (n=3). (D) Zeta potential measurements reveal negatively charged bare AuFe nanoparticles, and as expected, a less negatively charged particles after conjugation with Abs.

3.3.2 225-NP enhances cell killing

3.3.2.1 Cell lines and EGFR/pEGFR expression levels

Epidermal growth factor receptor (EGFR), both phosphorylated and total, expression were examined on several human non-small cell lung cancer (NSCLC) cells using Western blotting. NSCLC cells were wild type (H1299), mutated and overexpressed (HCC827, H1975, and H3255), amplified (H1819), or null (H520). Normal cells were lung fibroblasts (MRC-9 and WI38) and normal human bronchial epithelial (NHBE) cells.

Phosphorylated EGFR (pEGFR) and EGFR were detected in all cell lines except the EGFR-null cell line H520. pEGFR varied with NSCLC that expressed high levels of EGFR (HCC827, H4355, and H1819) (Figure 3.7a). Wild type H1299 cells had a medium level of expression of pEGFR. All normal cells (MRC-9, WI38, and NHBE) as well as mutated and overexpressed H1975 interestingly enough showed low levels of pEGFR.

3.3.2.2 Cell death

Adding Clone 225 conjugated nanoparticles (225-NP conjugates) to highly pEGFR-expressing HCC827, highly pEGFR-expressing H1819, and medium pEGFR-expressing wild type H1299 cells yielded significant cell death compared to control non-specific IgG-NP conjugates ($p<0.05$) (Figure 3.7b). The 225-NP conjugate-mediated cell killing effect was independent of EGFR mutational status. No significant cell death was seen with EGFR-null H520 cells treated with 225-NPs. Among the normal cell lines, normal lung fibroblasts MRC-9 showed some inhibitory effects, 9%, but this was less than the cytotoxic effect on the NSCLC cells, which was 14-18%. No effect was observed with normal human bronchial epithelial NHBE cells.

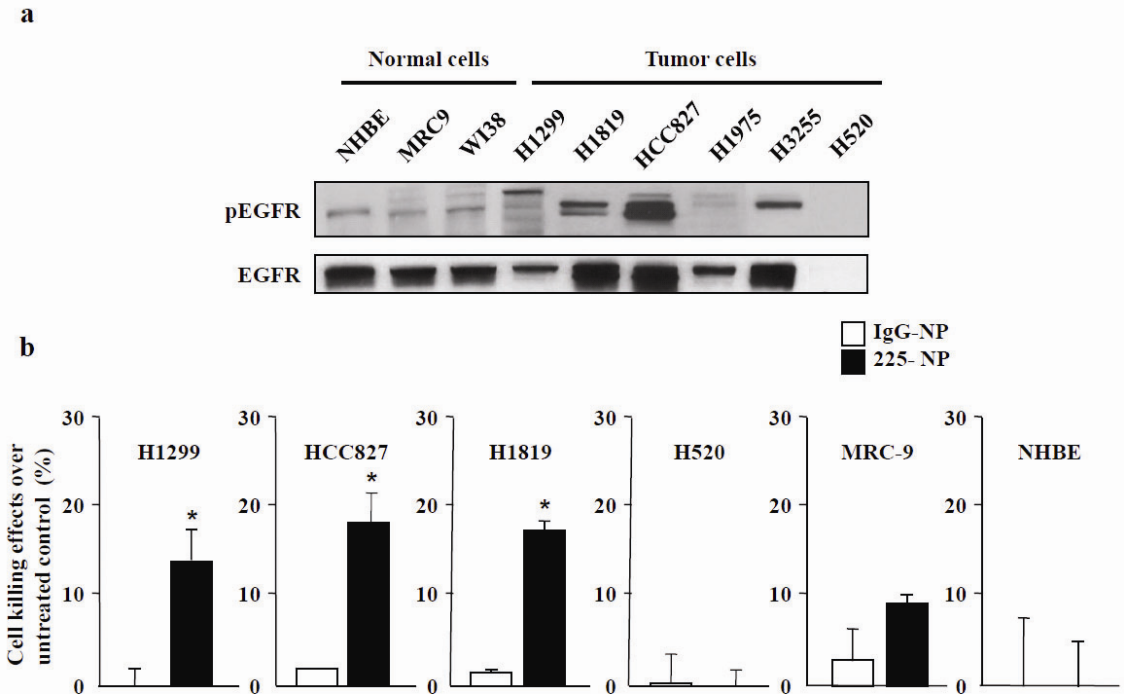

Figure 3.7 Effect of EGFR-targeted 225-NP treatment on NSCLC cells. (a) Expression of phosphorylated and total EGFR in normal and NSCLC cells. (b) Cell killing in response to EGFR-targeted 225-NP on NSCLC and normal cells. Results shown are the means ± S.D. of three independent experiments. *P-value<0.05 vs. IgG-NP on H1299, HCC827, and H1819 cells.

3.3.2.3 Protein expression

Protein expression was then assessed in the cells after being treated with either 225-NP or non-specific IgG-NPs. For high pEGFR-expressing HCC827 cells and medium pEGFR-expressing wild type H1299 cells treated with 225-NPs, a reduced expression of pEGFR, AKT (Protein Kinase B, which inhibits apoptotic processes), p38MAPK, and p44/42MAPK (mitogen-activated protein kinase, which is involved in cell differentiation) was observed compared to non-specific IgG-NPs treated cells (Figure 3.8).

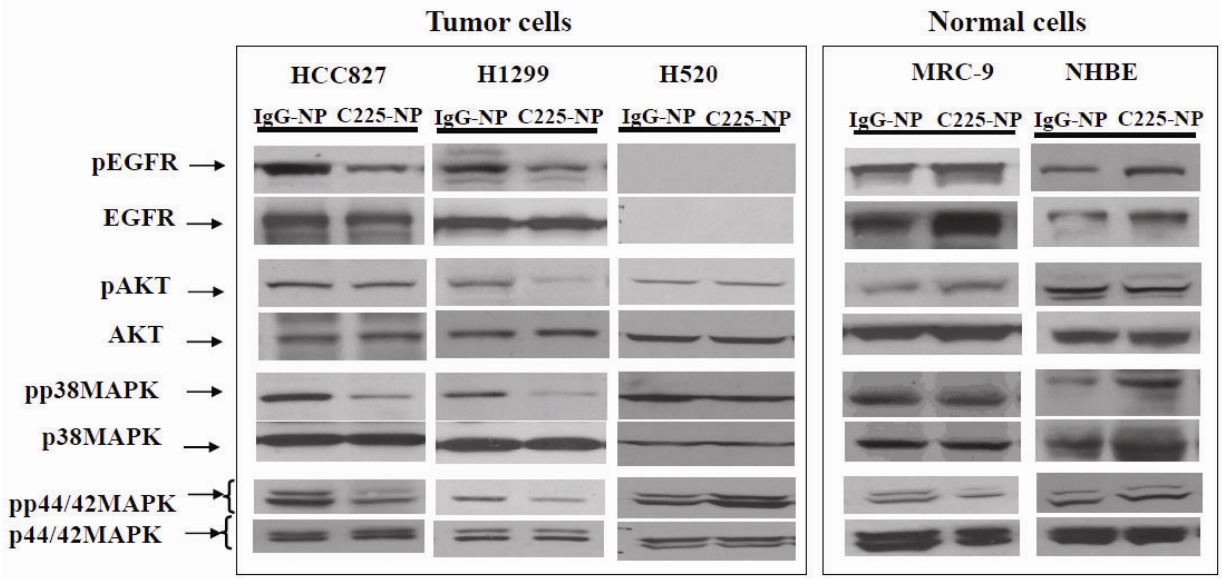

Figure 3.8 225-NP regulated EGFR signaling pathway in tumor cells but not in normal cells. Inhibitory effects of 225-NPs on phosphorylated EGFR (pEGFR) and the downstream signaling molecules involved in human lung cancer and normal cells. 225-NP treatment reduced the expression of the phosphorylated (p) forms of EGFR, AKT, p38MAPK, and P44/42MAPK in EGFR-positive tumor cells but not in normal cells. There was no effect on EGFR-null H520 cells.

pEGFR was markedly reduced by 35% ($p<0.05$) as shown by immunohistochemical staining in high pEGFR-expressing HCC827 cells treated with 225-NP, compared to non-specific IgG-NPs at 30 and 60 minutes after treatment (Figure 3.9). There was no marked reduction in pEGFR or other proteins that are involved in cell growth in normal cells (MRC-9 and NHBE) treated with either 225-NPs or non-specific IgG-NPs.

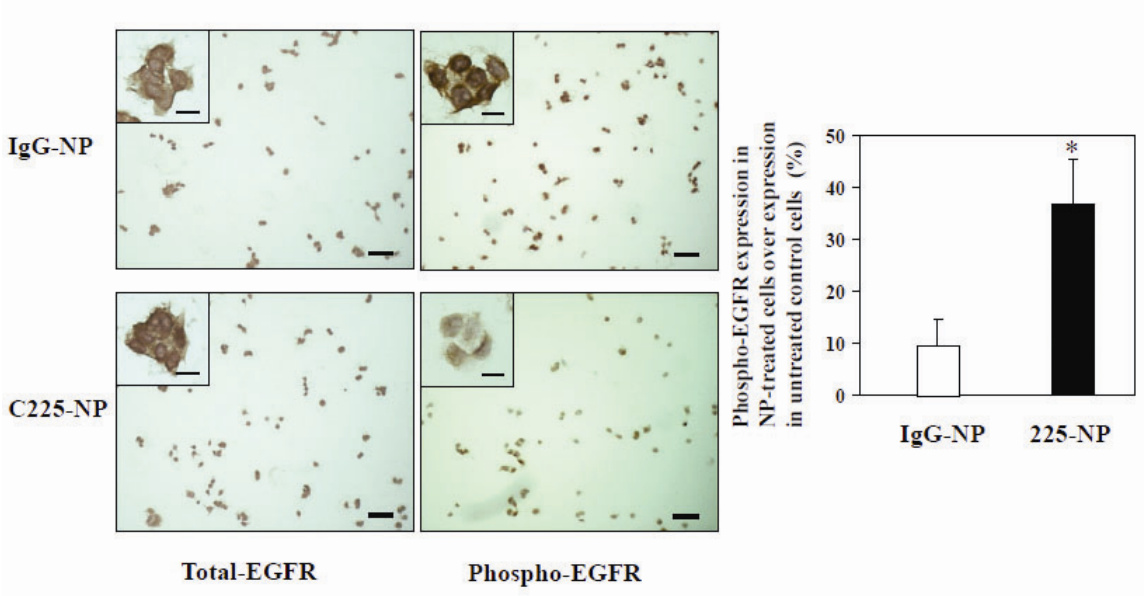

Figure 3.9 225-NP reduces phosphorylated EGFR (pEGFR) expression in NSCLC cells. IgG-NP or 225-NP-treated cells were stained for EGFR by immunocytochemistry. pEGFR expression was reduced in both IgG-NP and 225-NP-treated HCC827 cells when compared to untreated control cells; however, the reduction in pEGFR expression was significantly greater in 225-NP-treated cells (35% reduction over untreated control cells; p-value<0.05) than in IgG-NP-treated cells (8% reduction over untreated control cells).

3.3.3 225-NP produces greater antitumor activity than individual components of nanoparticle

3.3.3.1 Individual components

Next, we determined the contribution of the individual components of the nanoparticles on the killing effect of tumor cells. High pEGFR-expressing HCC827 cells were treated with AuFe nanoparticles alone and free 225, and both individually decreased cell viability by 12-14% over untreated control. A combination of free 225 mixed with (not conjugated to) free AuFe led to cell killing of 22% (Figure 3.10a). After conjugating the AuFe nanoparticle surface with Clone 225 antibody, these conjugates led to significantly higher cell death of 48% ($p<0.05$) than any of the individual components.

3.3.3.2 Non-therapeutic anti-EGFR antibody (Clone 29.1)

To gain more information from these conjugates' interactions with cells, we conjugated the surface of AuFe nanoparticles with non-therapeutic anti-EGFR antibodies (Clone 29.1) and looked at these targeted yet non-therapeutic conjugates' interactions with cells. While non-therapeutic Clone 29.1 antibody still binds to EGFR, the portion of the EGFR that Clone 29.1 binds to does not block the portion that a growth ligand EGF binds to. In contrast, Clone 225 does bind to a portion of the EGFR that blocks binding of EGF and thus inhibits growth of the cell. Clone 29.1 binds to a carbohydrate residue on an external portion of EGFR[210]. When high pEGFR-expressing HCC827 cells were treated with Clone 29.1-NPs, an intermediate cell killing effect (14%) was induced which was significantly less ($p<0.05$) than 225-NP-mediated cell killing effect, but more than other control treatments (7-15%) (Figure 3.10b).

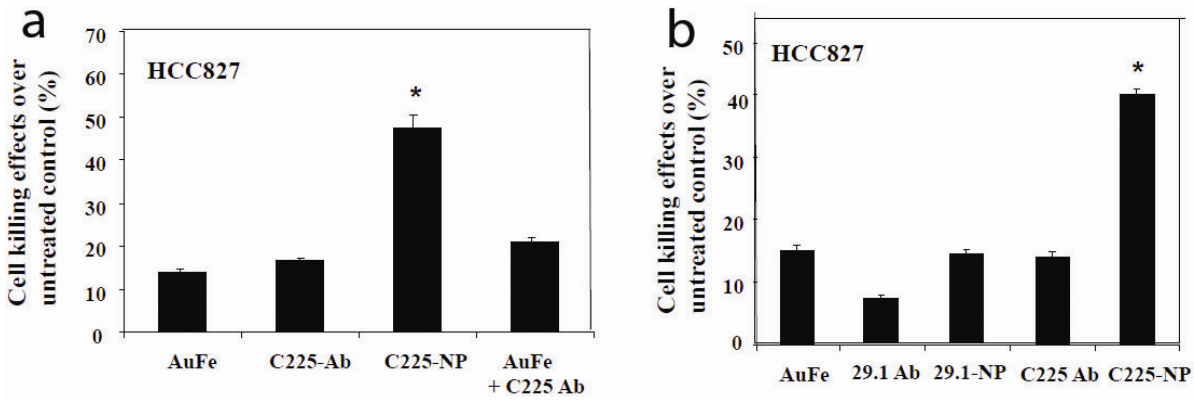

Figure 3.10 225-NP produces a greater killing effect than individual components of 225-NP. (a) HCC827 cells treated with 225-NPs demonstrated significant cancer cell killing effect compared to treatment with AuFe, 225 antibody, and a mixture of AuFe plus 225 antibody. *P-value<0.05. (b) Comparison of the inhibitory effects produced by 29.1-NP conjugates with 225-NPs on HCC827 cells. 225-NP treatment produced a great killing effect than 29.1-NP treatment compared to other treatment groups. *P-value<0.05.

These results show that assembling the therapeutic antibody Clone 225 on a surface of a nanoparticle results in enhanced cancer cell killing effect compared to individual components and targeted nanoparticles that do not have a therapeutic component.

3.3.4 225-NP induces both apoptosis and autophagy

3.3.4.1 Apoptosis

To determine the paths activated by 225-NP conjugates, we performed flow cytometric analyses on high pEGFR-expressing HCC827 cells and EGFR-null H520 cells treated with 225-NPs. The sub-G1 population, which indicates percentages of apoptotic cells, showed a dose-dependent response of apoptosis occurring in 225-NP-treated HCC827 cells (9-20%), while on non-specific IgG-NPs, there was only a 4-8% apoptotic population of the same cells (Figure 3.11a).

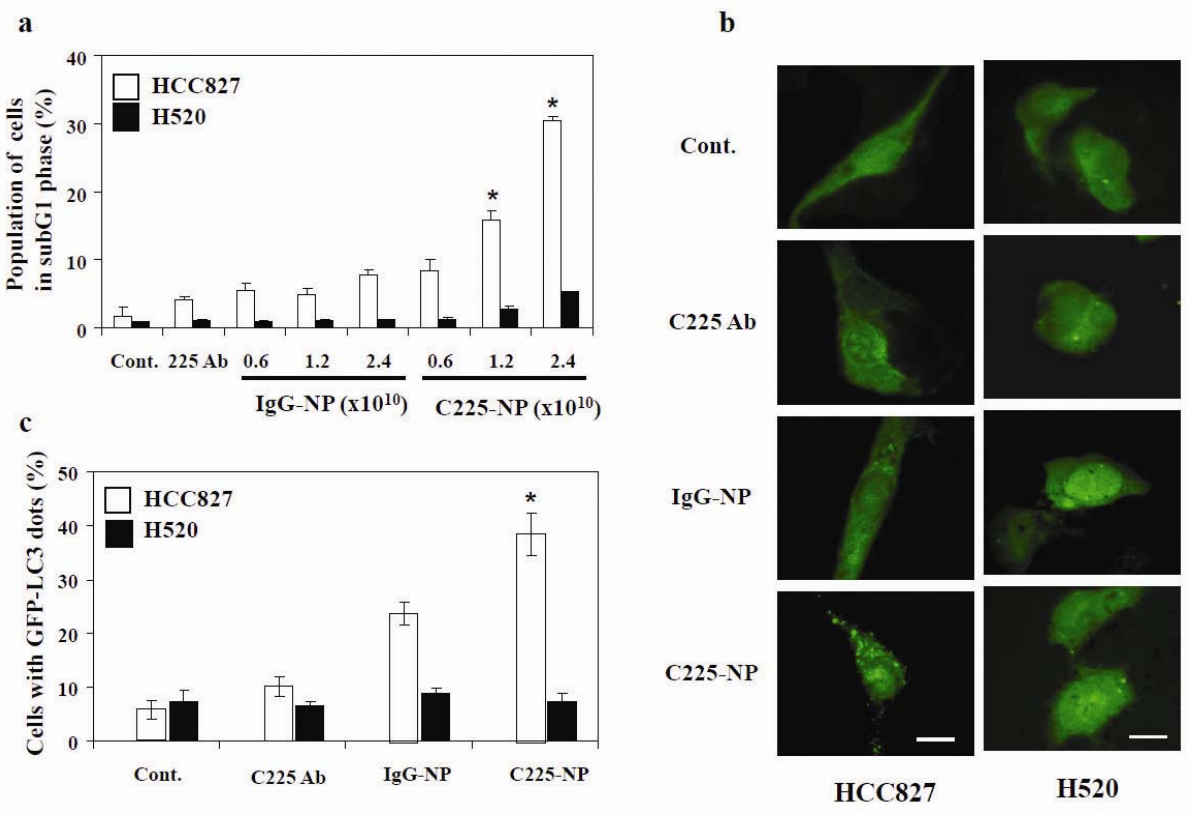

Figure 3.11 Induction of apoptosis and autophagy in response to EGFR-targeted 225-NPs in NSCLC cells. (a) Percentage of NSCLC cells treated with different doses (0.6, 1.2, and 2.4x10^{10} particles) of IgG-NP or 225-NP for 72 hrs that was in the sub-G1 phase of the cell cycle. This percentage was determined by DNA flow-cytometric analysis. Untreated cells and cells treated with free 225 antibody served as controls. A dose-dependent increase in the number of HCC827 cells in subG1 phase was observed in both IgG-NP and 225-NP treatments. The increase in number of cells in subG1, however, was significantly higher in 225-NP treatment than in IgG-NP (*P-value<0.05). There was no marked increase in subG1 phase in H520 cells between IgG-NP- and 225-NP-treatements. (b) Detection of GFP-LC3 dots indicative of autophagy on NSCLC cells that were not treated or treated with 225 antibody, IgG-NP, or 225-NPs (3x10^{9} particles) for 72 hours on chamber slides. Scale bar = 5 μm. (c) Quantification of the number of cells with GFP-LC3 dots on untreated and treated NSCLC cells. The number of cells with GFP-LC3 dots was higher in 225-NP-treated HCC827 cells compared to all other treatment groups. In H520 cells, there was no increase in the number of GFP-LC3 dots when treated with 225-NP and 225 antibody alone, and IgG-NP on HCC827 cells.

Clone 225 antibody alone yielded a significantly less percentage of apoptotic population (4-8%) compared to 225-NP-treated HCC827 cells (Figure 3.12). There was no increase in apoptotic population for EGFR-null H520 cells treated with either nanoparticle treatments (Figure 3.11a). Thus, 225-NP induced apoptosis in EGFR-expressing HCC827 cells over EGFR-null H520 cells.

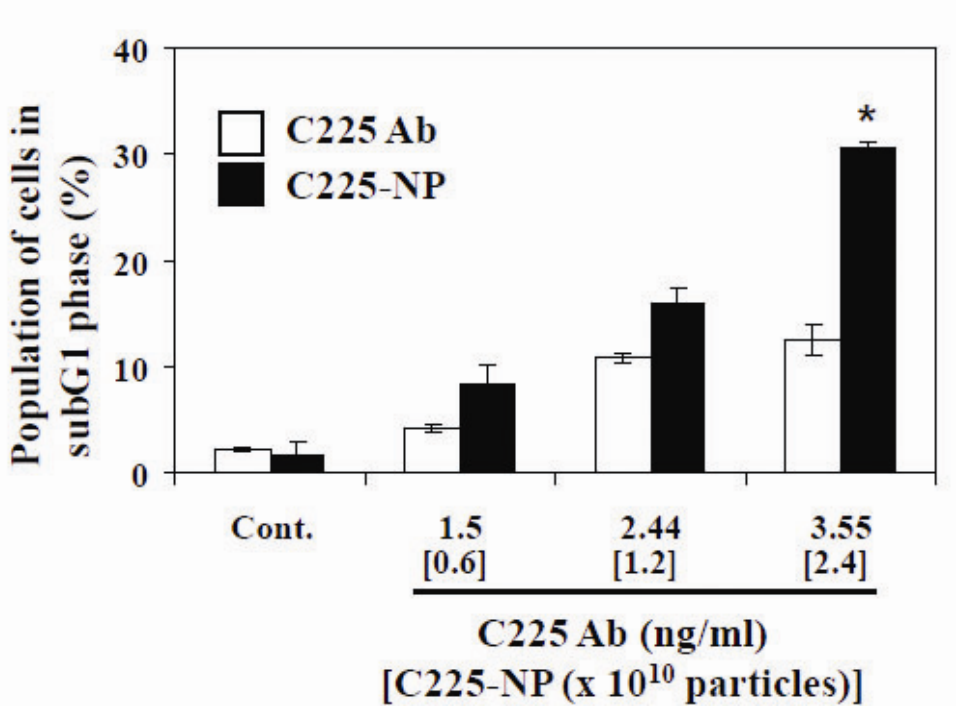

Figure 3.12 Comparison of free Clone 225 antibody with 225-NP conjugates on their ability to induce apoptosis in lung tumor cells. 225-NP treatment of HCC827 cells resulted in a dose-dependent increase in the percentage of cells in the subG1 phase compared to treatment with Clone 225 antibody at all concentrations tested. *P-value<0.05 vs. the same concentrations of Clone 225 antibody.

3.3.4.2 Autophagy

Recently, Seleverstov showed that quantum dots induced size-dependent autophagy in human mesenchymal stem cells[211]. Thus, to further elucidate activated

pathways, we investigated whether autophagy was occurring with our nanoparticles. We examined if autophagy was occurring in our cells after treatment of cells with nanoparticles using a green fluorescent protein (GFP)-tagged expression vector of microtubule associated-light chain 3 (LC3)[212]. In cells undergoing autophagy, the GFP-LC3 will distribute in a punctate distribution, sequestering in the membranes of autophagosomes, while a normal cell will yield an even distribution of LC3, and thus an even homogenous green color throughout the cell. Fluorescence images showed that high pEGFR-expressing HCC827 cells that did not receive 225-NP, but was transfected with the GFP-LC3 showed a diffuse distribution of GFP-LC3, while the same cells treated with 225-NP showed a punctate distribution indicating the presence of autophagic vacuoles (Figure 3.11b). The same even distribution was seen with control groups of non-specific IgG-NPs and 225 antibodies alone. The percentage of cells with a punctate distribution increased significantly ($p<0.05$) with treatment of 225-NPs compared to untreated cells (Figure 3.11c).

The same increase in autophagy indicated by a punctate distribution of GFP-LC3 was also observed in medium pEGFR-expressing H1299 cells that were treated with 225-NPs compared to control treatments (Figure 3.13).

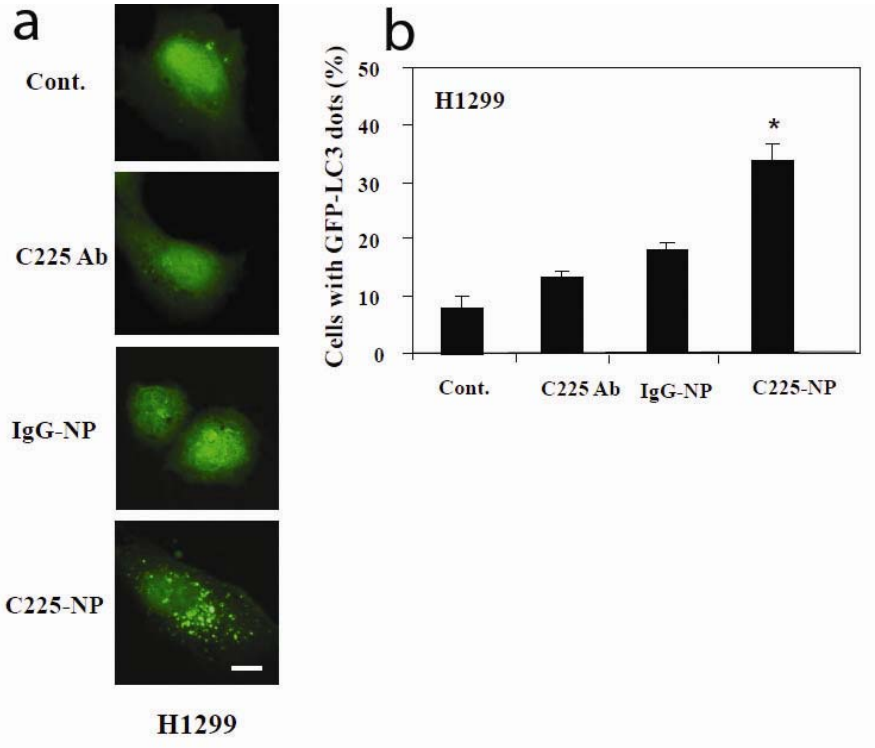

Figure 3.13 225-NP induces autophagy in H1299 lung cancer cells. (a) Detection of GFP-LC3 dots in H1299 cells that were either not treated or treated with Clone 225 antibodies, IgG-NPs, or 225-NPs ($3x10^9$ particles) for 72 hours on chamber slides. Scale bar = 5 μm. (b) Quantitative analysis showed 225-NP-treated HCC827 cells had a higher number of GFP-LC3 dots in comparison to all other treatment groups. Results shown are the means ± S.D. of three independent experiments. *P-value<0.05 vs. untreated control, Clone 225 antibody, and non-specific IgG-NP.

3.3.4.3 PARP cleavage

We wanted to further confirm that apoptosis and autophagy were occurring, so we investigated an apoptosis indicator, poly (ADP-ribose) polymerase (PARP) cleavage, and further studied the autophagy marker, light chain 3 (LC3) protein.

PARP cleavage was seen at 24 hours after treating high pEGFR-expressing HCC827 cells with either 225-NPs or with non-specific IgG-NPs, but PARP cleavage

was not observed in EGFR-null H520 cells. PARP cleavage was also higher for 225-NP-treated HCC827 compared to control nanoparticles (Figure 3.14a).

Regarding autophagy, light chain 3 (LC3) protein exists in tow forms: LC3-I and LC3-II. LC3-I is converted to LC3-II by conjugation to phosphatidylethanolamine, and the amount of LC3-II is closely correlated with the number of autophagosomes[213]. High pEGFR-expressing HCC827 cells treated with 225-NPs showed an increase in LC3-II over time, indicating autophagy was occurring (Figure 3.14a). Additionally, recent studies have shown that LC3-II is more accurately represented in autophagic flux when in the presence of lysosomal inhibitors[214]. Thus, in the presence of protease inhibitors E-64-d and pepstatin A, endogenous LC3-II increased in HCC827 cells after treatment with either IgG-NP or 225-NPs (Figure 3.14b). Again, the LC3-II amount was greater for HCC827 cells treated with 225-NPs compared to non-specific IgG-NPs. A similar increase in LC3-II was observed in medium pEGFR-expressing H1299 cells. In contrast, EGFR-null H520 cells treated with either nanoparticles conjugates after 72 hours did not show any increase in LC3-II amount, indicating autophagy was not occurring.

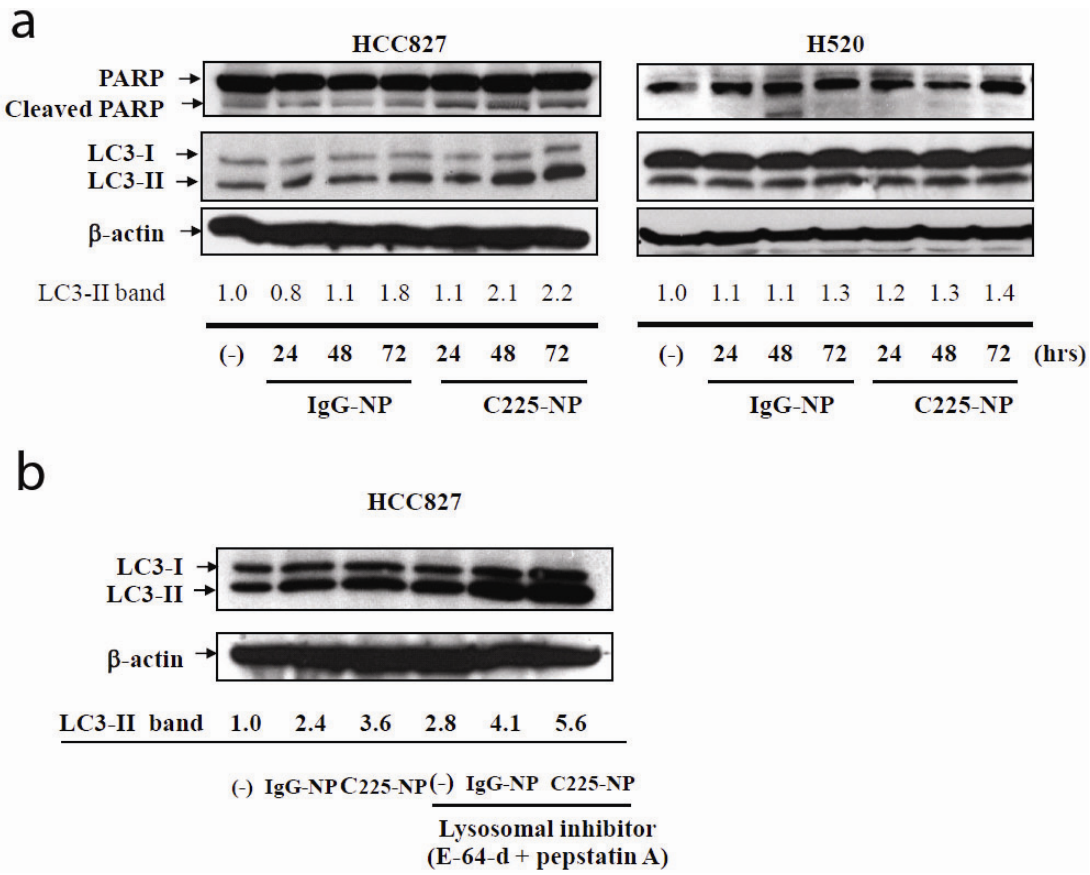

Figure 3.14 Analysis for molecular markers of autophagy and apoptosis in 225-NP-treated cancer cells. (a) Cellular proteins were lysed at the indicated time after treatment with IgG-NPs or 225-NPs ($6x10^9$ particles) and subjected to Western blotting. In HCC827 cells but not in H520 cells, increased PARP cleavage and LC3-II were observed at 48 and 72 hrs after treatment with 225-NPs and when compared with IgG-NP treatment and untreated control. The intensities of the amount of LC3-II bands were semi-quantified by ImageJ software (National Institutes of Health, Bethesda, MD). (b) MCC827 cells were treated with IgG-NPs or 225-NPs for 68 hrs. Cells were further cultured with or without protease inhibitors [10 μg/mL E-64-d and 10 μg/mL pepstatin A (BIOMOL International L.P., Plymouth Meeting, PA)] for 4 hours. Cellular proteins were lysed and immunoblotted with anti-LC3 antibody. LC3-II protein levels were increased in the presence of protease inhibitors in all of the groups indicating occurrence of autophagy. The intensities of the amount of LC3-II bands were semi-quantified by ImageJ software (National Institutes of Health, Bethesda, MD).

In conclusion, 225-NPs induced both apoptosis and autophagy in EGFR-expressing NSCLC cells. Non-specific IgG-NPs also induced autophagy to a lesser extent and caused a significantly less effect of cell killing compared to 225-NPs. This difference is probably because 225-NPs initiate autophagy and this autophagy is strong enough to activate a caspase cascade and lead to apoptotic cell death, while IgG-NPs induce a lesser extent of autophagy which serves as a cell survival mechanism and thus does not lead to cell death via apoptosis.

To further characterize the effects of 225-NPs on high pEGFR-expressing HCC827 cells, TEM of treated cells was performed. TEM images revealed a significant amount of autophagic vacuoles within HCC827 cells treated with 225-NPs compared to HCC827 cells treated with IgG-NPs ($p<0.05$) (Figure 3.15).

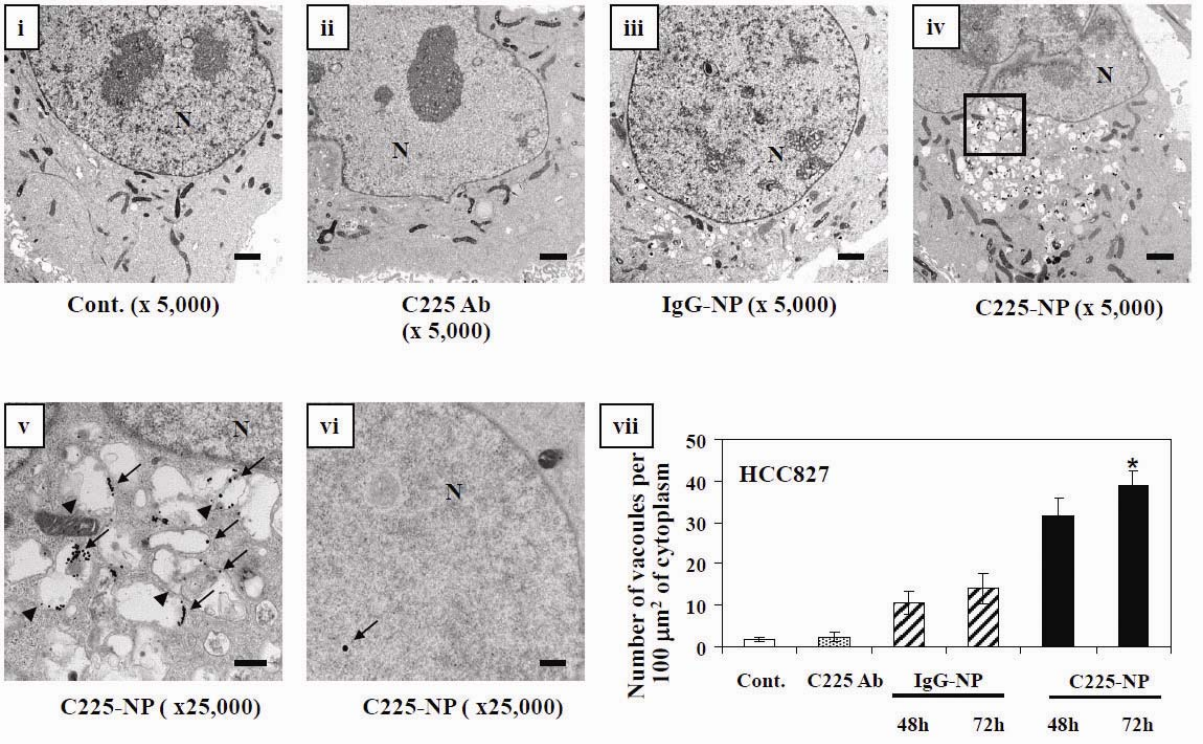

Figure 3.15 In situ localization of 225-NP in NSCLC cells. Electron micrographs showing the ultrastructure of a cell, including the nucleus (N), of HCC827 cells treated with Clone 225 antibody (0.065 μg/mL), IgG-NPs, or 225-NPs ($6x10^9$ particles) for 72 hours. (i) Untreated cells (ii) Clone 225 antibody-treated cells (iii) IgG-NP-treated cells (iv) 225-NP-treated cells (v) A magnified view of the area boxed in (iv). The arrows indicated NPs, and the arrowhead indicated autophagosomes that includes residual material and nanoparticles in the cytoplasm (vi) 225-NPs detected inside the nucleus. The arrow indicates nanoparticles in the nucleus. Scale bar = 1 μm. (vii) Autophagosomes were quantified, as describes in Materials and Methods (Chapter 3.2.8). *P-value<0.05 vs. controls, Clone 225 antibody and IgG-NPs for 48 and 72 hours.

While most 225-NPs were observed in vacuoles, a few 225-NPs were observed in the nuclei. This was confirmed with confocal microscopy (Figure 3.16). We did not quantify the number of particles in the nucleus because of limitations of using TEM and confocal for quantitative analysis. Because TEM has high resolution, the quantitation of multiple cells would be impractical. Analysis by confocal microscopy is complicated by

the fact that cellular uptake of the nanoparticles is mostly in the perinuclear space, and thus, optical resolution is not sufficient to separate the nanoparticles that are close to the nuclear membrane and the nanoparticles that are indeed inside the nucleus. Additionally, very bright objects such as gold nanoparticles can induce strong out of focus signal that can be misinterpreted in 3D. This limitation of 3D quantitation using confocal microscopy was demonstrated when the cytosolic uptake of quantum dots was overestimated[215].

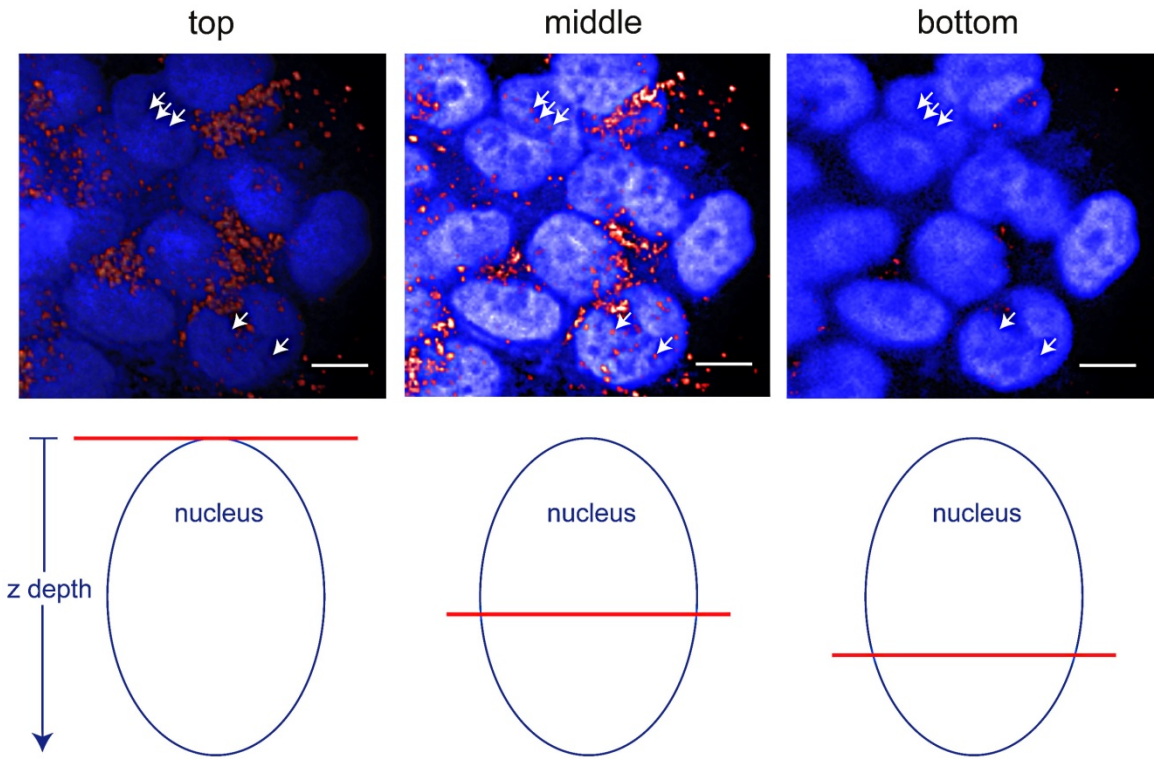

Figure 3.16 Detection of 225-NP localization in the nucleus by confocal microscopy. (Top row) Confocal images show DAPI stained nuclei (blue) and 225-NPs (red). Arrows in the "middle" column point to the 225-NPs localized in a nucleus. Arrows in the columns labeled "top" and "bottom" point to the same area in the xy plane of the nucleus but at locations above and below the middle of the nucleus, respectively. In both the "top" and "bottom" images, the arrows are no longer pointing at red spots which indicate that the red spots in the "middle" image are indeed within the nucleus. (Bottom row) Cartoon indicating the z position of each image within the nucleus, where the red horizontal line represents the relative depth position within the nucleus that the cross-sectional images (top row) were taken. Scale bar = 10 μm.

3.3.4.4 225-NPs are molecular-specific for EGFR

Dark-field reflectance (DR) microscopy was used to characterize 225-NP interactions and the feasibility of optical detection of NSCLC cells. DR images showed a high concentration of internalized 225-NP in high pEGFR-expressing HCC827 cells after

24 hours after treatment (Figure 3.17). In contrast, no uptake was observed for IgG-NPs, and in EGFR-null H520 cells, no uptake was seen with any nanoparticles (Figure 3.17).

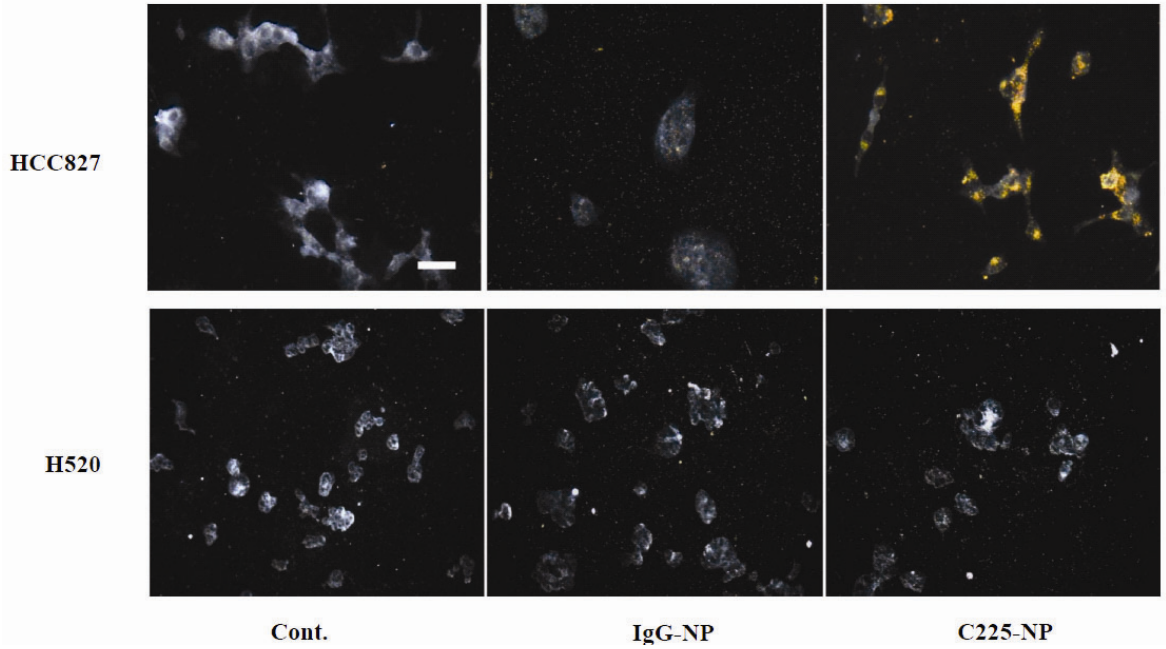

Figure 3.17 Visualization and determination of selective binding and uptake of 225-NPs in NSCLC cells. HCC827 and H520 cells seeded on chamber slides were treated with IgG-NPs or 225-NPs ($2x10^9$ particles). Untreated cells served as control. At 24 hours after treatment, cells were washed, fixed, and images were taken under dark-field reflectance (DR) microscopy. Scale bar is 50 μm. Selective binding and uptake of 225-NPs but not IgG-NPs was observed in HCC827 cells. In H520 cells, there was no binding and uptake of 225-NPs when compared with IgG-NPs

A standard competition assay was also performed to determine the specificity of the 225-NP binding to EGFR. High pEGFR-expressing HCC827 cells were pre-treated with an excess of free Clone 225 antibody prior to being treated with non-specific IgG-NPs or 225-NPs. DR images showed binding of 225-NPs was blocked by pre-treatment of free Clone 225 antibody (Figure 3.18)

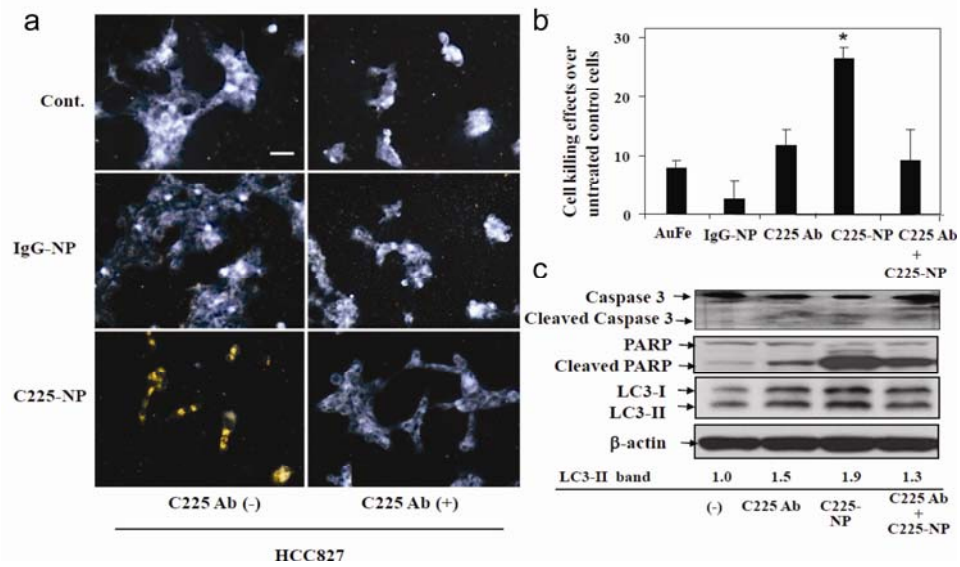

Figure 3.18 225-NP is specific for EGFR-expressing tumor cells and pre-treatment with Clone 225 antibody abrogates 225-NP-mediated tumor cell killing. (a) The right column shows images of HCC827 cells pre-treated with Clone 225 antibody (2 μg/mL) for 15 minutes before incubation with either IgG-NPs (middle row) or 225-NPs (bottom row). Cells shown in the left column were not treated with free Clone 225 antibodies. The fixed cells were imaged using dark-field reflectance microscopy. Binding and uptake of 225-NPs was completely inhibited in the presence of Clone 225 antibody. In IgG-NP-treated cells, Clone 225 antibody had no effect. Scale bar is 50 μm. (b) Inhibition effect on the cytotoxicity of 225-NPs by pre-treatment with free Clone 225 antibody. After treatment with/without Clone 225 antibody (0.065 μg/mL) for 6 hours, the cells were treated with either non-conjugated nanoparticles (AuFe), IgG-NPs, or 225-NPs for an additional 66 hours. The number of viable cells was counted as described in Materials and Methods. Results shown are the means ± S.D. of three independent experiments. *P-value<0.05 vs. AuFe alone, Clone 225 antibody alone, IgG-NPs, or Clone 225 antibody plus 225-NPs. (c) Inhibition effects on 225-NP-induced apoptosis and autophagy by pre-treatment with Clone 225 antibody. Cellular proteins were lysed after treatment with 225-NPs ($6x10^9$ particles) for 66 hours in the presence or absence of free Clone 225 antibody (0.065 μg/mL). Proteins were separated by SDS-PAGE, and immunoblotted with anti-PARP and anti-LC3 antibodies. The anti-β-actin antibody was used as a control for protein loading and transfer. The intensities of the amount of LC3-II bands were quantified by ImageJ software. 225-NP-mediated activation of apoptosis and autophagy as indicated by cleavage of caspase-3, PARP, and LC3-II respectively was markedly abrogated in the presence of free Clone 225 antibody.

Pre-treatment with free Clone 225 antibodies attenuated the cytotoxicity effect of 225-NP conjugates, leading to a reduced amount of apoptosis and autophagy observed in HCC827 cells compared to no pre-treatment (Figure 3.18b,c). A similar reduction in apoptosis and autophagy was observed for medium pEGFR-expressing H1299 cells treated with 225-NPs after being pre-treated with free Clone 225 antibodies (Figure 3.19).

In conclusion, 225-NPs interacted specifically with EGFR and induced a molecular-specific enhanced cell death effect on EGFR-overexpressing NSCLC cells.

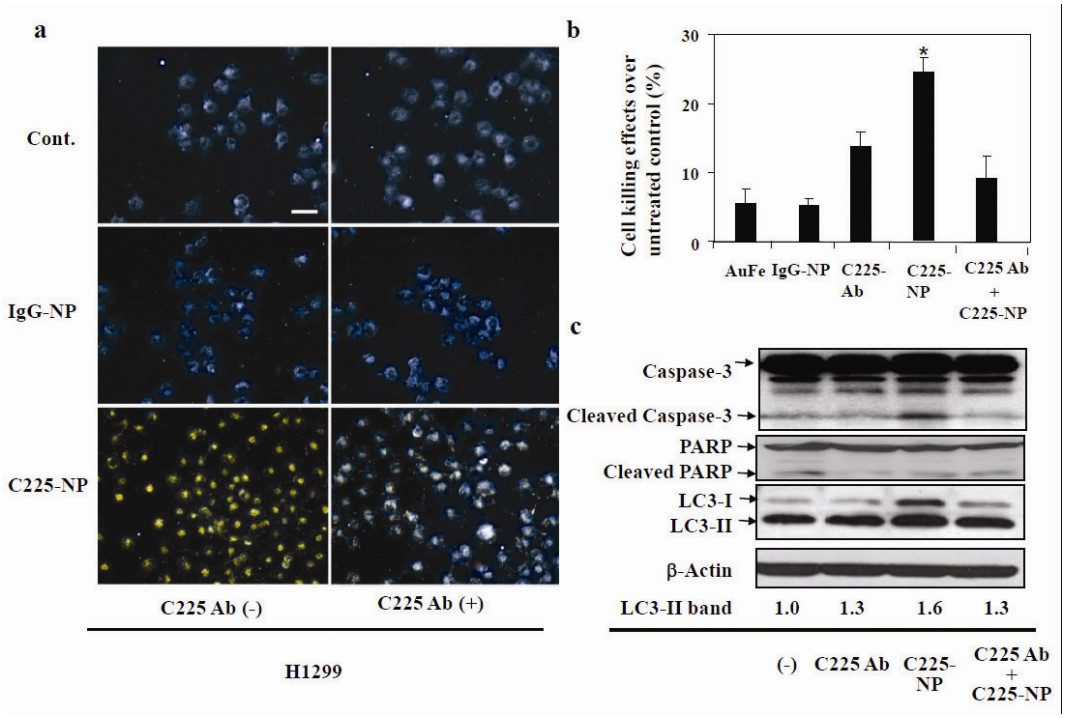

Figure 3.19 Visualization and determination of selective binding and uptake of 225-NPs in H1299 cells. (a) In the right column, cells were treated with free Clone 225 antibody (2 μg/mL) for 15 minutes, and then incubated with either IgG-NPs or 225-NPs for an additional 24 hours. The left column was not pre-treated with free antibodies. Images were obtained using dark-field reflectance microscopy. Binding was inhibited by pre-treatment with free antibodies. In IgG-NP-treated cells, pre-treatment had no effect. Scale bar is 50 μm. (b) Inhibition effects of free Clone 225 antibody on the cytotoxicity of 225-NPs. After pre-treatment with antibody (0.065 μg/mL) for 6 hrs, cells were treated with 225-NPs for an additional 66 hrs. Cells were treated with 225-NPs, free Clone 225 antibodies, non-conjugated NP (AuFe), and IgG-NPs. Results are the means ± S.D. of three independent experiments. *P-value<0.05 vs. AuFe alone, free Clone 225 antibody, IgG-NP, or Clone 225 antibody plus 225-NP. (c) Inhibition effects of pre-treatment with 225-NPs ($6x10^9$ particles) for 66 hrs in the presence or absence of free antibody. Proteins were separated by SDS-PAGE, and immunoblotted with anti-PARP and anti-LC3 antibodies. The intensities of the amount of LC3-II bands were quantified by ImageJ software. 225-NP-mediated activation of apoptosis and autophagy as indicated by cleavage of caspase-3, PARP, and LC3-II respectively was markedly abrogated in the presence of free Clone 225 antibody. PARP cleavage was not detectable in all of the groups.

3.3.4.5 Density of antibodies attached to the surface of nanoparticles is important

The dependence of therapeutic efficacy of nanoparticles on the density of Clone 225 antibodies conjugated to the surface of the nanoparticles was investigated. Ratios of Clone 225 antibody to non-specific IgG antibody of 1:0, 1:1, 1:3, 1:10, 1:40, and 0:1 were conjugated to the surface of the nanoparticle. A conjugate with ratio 1:0 corresponded to the original 225-NP while a ratio of 0:1 corresponded to a nanoparticle conjugated to only non-specific IgG antibodies. The relative density of antibodies conjugated to the surface of the nanoparticles was confirmed using a fluorescent assay. More details of this method can be found in the Materials and Methods section Chapter 3.2.2. The total amount of antibodies on the surface of the nanoparticle was kept constant between all nanoparticles. Nanoparticles of 1:0 ratio which are 225-NPs showed significantly higher cell killing effect ($p<0.05$) on high pEGFR-expressing HCC87 cells and medium pEGFR-expressing H1299 cells compared to nanoparticles of 0:1 ratio, which were non-specific IgG-NPs. As the density of the Clone 225 antibodies on the surface of the nanoparticle decreased, so did the cell killing effect on both cell lines (Figure 3.20a). The same trend was observed when autophagy was measured in these cells (Figure 3.20b,c). This density-dependent therapeutic effect can steer therapeutic strategies towards developing nanoparticles that can hold extremely high loadings of therapeutic antibodies[216].

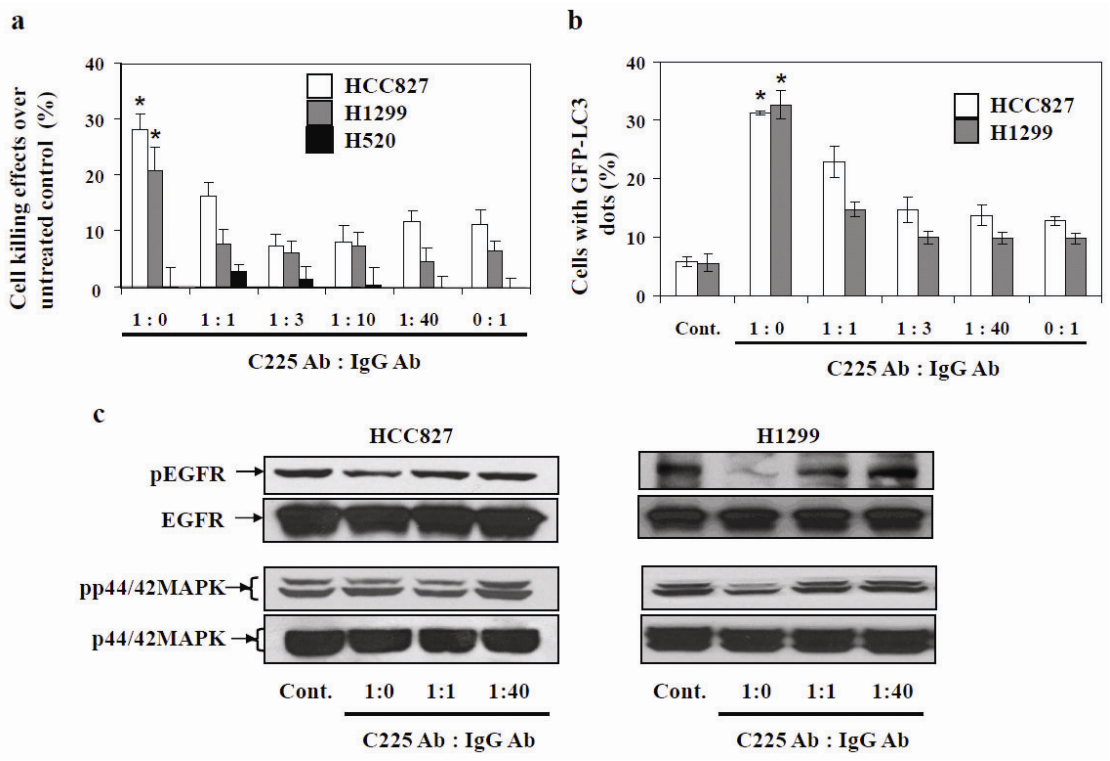

Figure 3.20 Effect of antibody density on 225-NP-mediated killing of NSCLC cells. (a) Cell growth inhibition in response to treatment with nanoparticles that had varying ratio (1:0, 1:1, 1:3, 1:10, 1:40, and 0:1) of Clone 225 antibody and anti-rabbit IgG antibody co-conjugated to the nanoparticle surface. Cells (HCC827, H1299, and H520) were treated with nanoparticles ($6x10^9$ particles) for 72 hours. The number of viable cells was counted as described in Materials and Methods. Results are the means ± S.D. of three independent experiments. *P-value<0.05 for 225-NPs (1:0) vs. nanoparticles with 1:1 – 1:40 and 0:1 nanoparticles on HCC827 and H1299 cells. H520 cells showed no inhibitory effect when treated with nanoparticles of different ratios. (b) The number of GFP-LC3 dots induced by 225-NPs (1:0)-treatment on HCC827 and H1299 cells decreased with changes in Clone 225 antibody: anti-rabbit IgG antibody ratio. Results are the means ± S.D. of three independent experiments. *P-value<0.05 for 225-NPs (1:0) vs. 1:1 – 1:40 and 0:1 nanoparticles on HCC827 and H1299 cells. (c) 225-NPs (1:0)-mediated reduction in the pEGFR and p44/42MAPK expression was abrogated in HCC827 and H1299 ells when treated with nanoparticles of 1:1 and 1:40 ratio.

This observed decrease in cell killing effect can be attributed to decreasing density of therapeutic Clone 225 antibody on the surface of the nanoparticles, which led to a decrease in valency. Previous report have shown that increasing the valency of a molecule can increase the binding affinity of the molecule to its target[196-197]. For more details on this multivalent effect, see Chapter 3.1.2. In contrast, EGFR-null H520 cells showed little to no cytotoxicity when treated with nanoparticles with varying ratios of antibodies.

In conclusion, nanoparticles coated completely in Clone 225 antibodies showed the greatest cytotoxic effect, and decreasing the density of these therapeutic antibodies led to a decreased antitumor effect. This study also demonstrated the specificity of 225-NPs' cell killing on NSCLC cells.

3.3.5 Conclusions and Discussion

We demonstrate that EGFR-targeted 225-NP conjugates are selectively taken up by EGFR-overexpressing NSCLC cells and produced an enhanced antitumor effect by inducing both autophagy and apoptosis. The enhanced tumor cell killing is attributed to the unique properties conferred by the conjugation of Clone 225 antibody with AuFe nanoparticles. While previous research using EGFR-targeted plasmonic gold nanoparticles has focused only on the ability of the gold nanoparticles to induce photothermal therapy, we have demonstrated another route of cell death here, via multivalent enhancement of a therapeutic antibody. This enhanced effect is immediately significant because the therapeutic molecule being studied is currently used in the clinic and enhancing the molecule's effect can lead to better survival rates as well as minimize the dose. Additionally, this is the first study to reveal the cell death pathways that are activated by this 225-NP conjugate. This information helps us understand the exact effect

of our therapeutic molecule and can lead us to tailor designs of future nanoparticle conjugates for specific individual patients' needs.

Future work will focus on attempting to elucidate activated pathways of the conjugates and other effects that are different between targeted, therapeutic nanoparticles and controls. Another future path is to determine if combination therapy can enhance the effect of these conjugates because previous studies suggest this is possible[217]. Additionally, previous studies have shown that these hybrid core/shell iron oxide/gold nanoparticles yield strong T2 weighted contrast in MRI because of the iron oxide component of the nanoparticles[112b]. Thus, future work will involve monitoring these conjugates in vivo using MRI.

Chapter 4: Clearance of Hybrid Gold Nanoparticles

4.1 INTRODUCTION

In the past couple of decades, various plasmonic gold nanoparticles have been extensively investigated as near infrared (NIR) image contrast agents for biomedical applications. Absorbance of these agents in the NIR wavelength range is desired because this range is where the tissue optical window lies. Intravenous administration of these agents allows the agents to be rapidly dispersed throughout the body. Previous reports have indicated that nanoparticles of the size 6-100 nm exhibit sufficiently long blood residence time to accumulate at diseased sites such as cancer and cardiovascular plaques[218]. If particles are <6 nm, they can be removed quickly from the blood stream through pores between endothelial cells lining blood vessels and be filtered through the kidneys[164]. On the other extreme, particles >100 nm are quickly removed from the blood stream by the body's immune cells[219].

Along with long blood circulation, an ideal nanoparticle for biomedical applications would also have a large optical cross-section for imaging and potential photothermal therapy. Nanoparticles of larger dimensions have larger optical cross-sections. Metal nanoparticles of the size 50 nm or larger have shown strong NIR absorbance[22, 127b, 193, 220].

As inorganic nanoparticles are not biodegradable, there exist concerns about their long-term toxicity[164, 221]. These concerns have restricted their translation to the clinic. The FDA mandates that diagnostic agents must be completely cleared in a reasonable time[164]. Thus, translation of the nanoparticles to the clinic involves their ability to be efficiently cleared by the body. Previous studies indicate that nanoparticles must be less than 6 nm to be efficiently cleared[164]. Thus, there is a conflict between two essential optimal sizes

for a biomedical imaging and therapeutic agent: optimal size for delivery, imaging, and therapy (50 nm or greater), and optimal size for efficient clearance (<6 nm).

Here, we address this conflict by developing a flexible platform for the kinetically controlled assembly of sub-5 nm gold particles to produce ~100 nm biodegradable nanoclusters with strong NIR absorbance for multimodal and multifunctional applications. The nanoclusters are stabilized with a small amount of weakly adsorbed biodegradable triblock co-polymer: PLA(2K)-b-PEG(10K)-b-PLA(2K). The polymer degrades under physiological conditions to release the constituent clearable gold particles. These clusters can provide sufficient blood residence time for clinical applications, while facilitating effective clearance from the body after biodegradation (Figure 4.1a). Close spacing between the gold particles within the 100 nm clusters facilitates strong NIR absorbance. The hydrophilic PEG loops in the center block of the polymer extend into the aqueous environment and provide steric stabilization for the clusters. The results from this chapter have been recently published in the journal ACS Nano[222].

4.2 MATERIALS AND METHODS

4.2.1 Gold particle synthesis

To synthesize the citrate-capped gold nanoparticles, 100 mL of deionized (DI) water was heated to 97°C. While stirring, 1 mL of 1% $HAuCl_4 \cdot 3H_2O$, 1 mL of 1% $Na_3C_3H_5O(COO)_3 \cdot 2H_2O$, and 1 mL of 0.075% $NaBH_4$ in a 1% $Na_3C_3H_5O(COO)_3 \cdot 2H_2O$ solution was added in 1 minute intervals. The solution was stirred for 5 minutes and then removed to an ice bath to cool to room temperature. The gold particles were then concentrated using centrifugal devices (Ultracel YM-30, Millipore Co.) to 3 mg Au/mL.

Gold concentrations were determined using flame atomic absorption spectroscopy (FAAS), as described below.

4.2.2 Nanocluster characterization

The nanocluster morphology was observed by scanning electron (SEM) and transmission electron microscopy (TEM). A Zeiss Supra 40VP field emission SEM was operated at an accelerating voltage of 5-10 kV. SEM samples were prepared by depositing a dilute aqueous dispersion of the nanoclusters onto a silicon wafer. The sample was then dried and washed with DI water to remove excess polymer. TEM was performed on an FEI TECNAI G2 F20 X-TWIN TEM using a high-angle annular dark-field detector. A dilute aqueous dispersion of the nanoclusters was deposited onto a 200 mesh carbon-coated copper TEM grid for observation. Separation distances between primary particles within the nanoclusters were measured by analyzing TEM images using Scion Image software (Frederick, Maryland). UV-Vis spectra were obtained with a Varian Cary 5000 spectrophotometer and a 1 cm path length. Dynamic light scattering (DLS) measurements of hydrodynamic diameter and zeta-potential measurements were performed in triplicate on a Brookhaven Instruments ZetaPlus dynamic light scattering apparatus (scattering angle of 90°) at a temperature of 25°C. Dispersion concentrations were adjusted with either DI water for DLS measurements of pH = 7.4 buffer (10 mM) for zeta-potential measurements to yield a measured count rate between 300 and 400 kcps. Prior to all DLS measurements, the nanocluster dispersions were filtered through a 0.2 μm filter and probe sonicated for 2 minutes. Data analysis was performed using a digital autocorrelator (Brookhaven BI-9000AT) with a non-negative least-squares (NNLS) method (Brookhaven 9KDLSW32). Reported average diameters correspond to the D_{50} or diameter at which the cumulative sample volume was under 50%. For zeta-

potential measurements, the average value of at least three data points was reported. Thermogravimetric analysis (TGA) was conducted using a Perkin-Elmer TGA 7 under nitrogen atmosphere at a gas flow rate of 20 mL/min. The samples were cleaned to remove excess polymer by centrifuging nanocluster dispersions at 800°C for 30 minutes. Flame atomic absorption spectroscopy (FAAS) was used to determine the gold concentration in the nanocluster dispersion using a GBC 908AA Flame atomic absorption spectrometer (GBC Scientific Equipment Pty Ltd.). Measurements were conducted at 242.8 nm using an air-acetylene flame. To determine clustering efficiency, dispersions of nanoclusters of known concentration were centrifuged at 10,000 rpm for 10 minutes at 4°C. FAAS measurements were conducted on the supernatant.

4.2.3 Hyperspectral characterization of nanoclusters in solution

Microscope slides were submerged in a warm, aqueous gelatin solution (3% w/v) for 10 minutes. The slides were removed from the gelatin and 10 μL of a dilute nanocluster dispersion (~0.01 mg/mL) was placed on the gelatin-coated slide and covered with a coverslip. The gelatin was allowed to cool for 2 hours to allow the nanoparticles to solidify into the gelatin. Hyperspectral images were acquired under the same conditions as described below for cell studies.

4.2.4 Cellular studies of nanocluster disassembly

The cells were J774A.1 murine macrophage cells (American Type Culture Collection, Manassas, VA) and were cultured in a 12-well plate in a phenol-free DMEM media (Gibco, Grand Island, NY) supplemented with 5% fetal bovine serum (Hyclone, Logan, UT) and antibiotics (Gibco, Grand Island NY) and incubated at 37°C in a 5% CO_2 environment for 1 week. The nanoclusters were filtered through a 0.45 μm filter (Corning, Corning, NY) spun down and resuspended in DMEM medium and, then, were

added to each well with cells (0.4 mg per well). Incubation of the cells with the nanoclusters occurred over 24 hours, after which the excess of the nanoparticles was removed and the cells were allowed to proliferate to 96 or 168 hour time points. The cells were washed three times in 0.01 M phosphate buffered saline (PBS), harvested, and centrifuged at 110 x g for 3 minutes. The supernatant was discarded. The cells were resuspended in 10 μL of PBS, placed on a microscope slide, and imaged using a combination of dark-field reflectance (DR) and hyperspectral (HS) imaging. DR microscopy images of the cells and nanoclusters were taken with a Leica DM6000 upright microscope, and the hyperspectral system was calibrated using a standard wavelength calibration lamp (low pressure Hg, Lightform, Inc.). All HS spectra from cells were normalized by the spectrum of the Xe excitation light source on a pixel by pixel basis. RGB images were taken with a Q-imaging Retiga EXi CCD camera with color LCD attachment. Images were white balanced with a Spectralon (Labsphere, North Sutton, NH), and the acquisition settings were chosen such that all samples were acquired under identical conditions.

For the studies involving TEM of cells, approximately $3x10^4$ cells were seeded overnight on Aclar Embedding Film (Electron Microscopy Sciences, Hatfield, PA). All samples for TEM imaging were treated identically and were run in parallel to the samples used for optical imaging. At each time point, the cells were fixed in a 1% glutaraldehyde and 1% paraformaldehyde solution for 1 hour at room temperature and then washed three times in PBS. Subsequently, cells were stained with 2% osmium tetroxide in water for 10 minutes and washed for 10 minutes in water. The sample was then dehydrated using increasing ratios of ethanol to acetone solutions and finally embedded in an epoxy-acetone mixture and allowed to bake at 60°C for 24 hours. Ultrathin sections were sliced

using a Leica Ultracut microtome (Leica, Deerfield, IL) and imaged with a Tecnai G2 TEM at a voltage of 80 kV.

4.2.5 Mice studies

Female 2-4 months old Balb/c mice (Jackson Labs) were used for all mice studies. All procedures performed on the mice were approved by the University's Institutional Animal Care and Use Committee. Mice were divided into three groups: non-degrading solid nanoparticle-injected, biodegradable nanocluster-injected, and PBS-injected mice. Each nanoparticle-injected group contained 4 mice, while the PBS-injected group contained 3 mice. Mice were followed up to 4 months, with time points of sacrifice 1 day, 1 week, 1 month, 2 months, 3 months, and 4 months. At each time point, organs were harvested and analyzed using inductively coupled plasma mass spectrometry (ICP-MS) and microscopy. Mice were placed individually in metabolic cages to collect urine and feces samples from each mouse for analysis of cleared nanoparticles. PBS-injected mice were only followed up to 1 month because of a limited number of cages.

Mice were given a 200 μL injection of either nanoparticles (6 mg/mL) or PBS via tail vein.

4.2.6 Inductively coupled plasma mass spectrometry

Harvested organs from mice were digested using a microwave digestion system (MARS Xpress, CEM GmbH, Germany). Samples were digested using a mixture of 35% HNO_3 (Fisher Scientific) and 18.5% HCl (Fisher Scientific) in the microwave to homogenize, and samples were analyzed using inductively coupled plasma mass spectrometry (ICP-MS). Samples were then diluted to <10% acid in water and calibration standards were prepared using a NIST gold standard of 1000 ppm Au, diluted to a range

of 1-50 ppb. Samples were then analyzed using an ICP-MS (GBC Scientific Equipment, Australia).

4.3 RESULTS

4.3.1 Current methods of synthesizing assemblies of nanoparticles

Properties of assemblies of nanoparticles such as size and interparticle spacing are controlled by varying particle volume fractions during solvent evaporation. The changes in electrostatic, van der Waals (VDW), depletion, and steric interactions on the concentration of the gold nanoparticles and polymer micelles govern the kinetic assembly of the nanoclusters as well as their disassembly after polymer degradation[223]. Without the presence of a polymeric stabilizer, irregular micrometer-sized aggregates of gold nanoparticles have been formed by varying the particle charge after adjusting the pH for particles capped with lysine[221, 224], cysteine[225], or glutathione[226] ligands. Alternatively, nanoclusters composed of metal particles may be formed by equilibrium self-assembly with polymer templates[227] but the high polymer concentrations required for the equilibrium assembly typically lead to metal loadings and interparticle spacings that are not sufficient for strong NIR absorbance. Additionally, the templating agents are highly specialized.

In contrast, our kinetically controlled assembly platform requires only small concentrations of commonly used copolymers as stabilizers and simple biocompatible capping ligands on gold, such as citrate and/or lysine.

4.3.2 Nanocluster characterization

4.3.2.1 Morphology

Nanocluster growth is controlled by mediation of the interactions between ligand-capped gold particles with biodegradable polymer (Figure 4.1b).

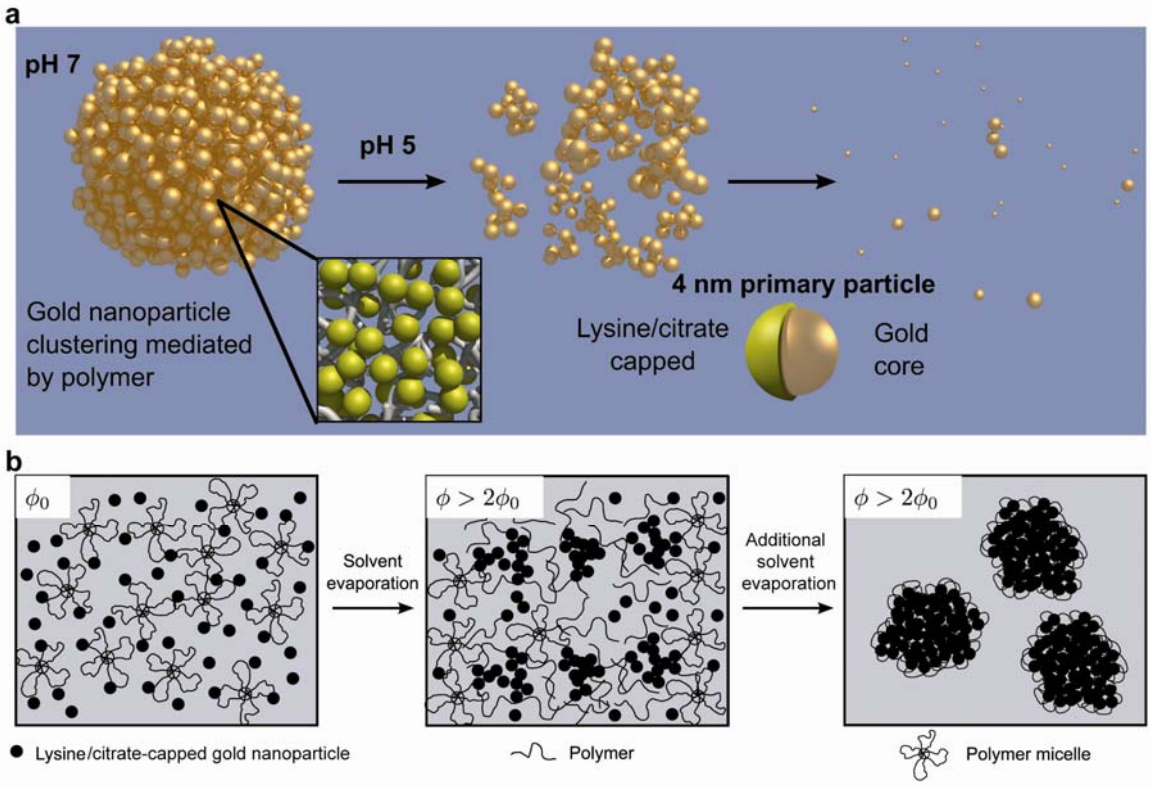

Figure 4.1 Schematic of synthesis and degradation of gold nanoclusters. (a) Illustration of a biodegradable nanocluster, which is composed of ~4 nm primary gold particles held together with a biodegradable polymer. Upon polymer degradation, catalyzed by low pH in endosomal compartments of cells, the nanocluster deaggregates into primary gold nanoparticles. (b)Schematic of nanocluster formation process, in which primary gold nanoparticles aggregate in the presence of a polymer in a controlled manner to yield sub-100 nm clusters. Polymer adsorption to the nanoparticle surface and an increase in the volume fraction of particles, Φ, via solvent evaporation promote cluster formation.

Gold nanoparticles stabilized with citrate ligands were synthesized based on a previously published method[228]. Lysine was used as a stabilizing agent for the gold nanoparticles, and led to an average diameter of 4.1±0.8 nm (Figure 4.2a and Figure 4.3).

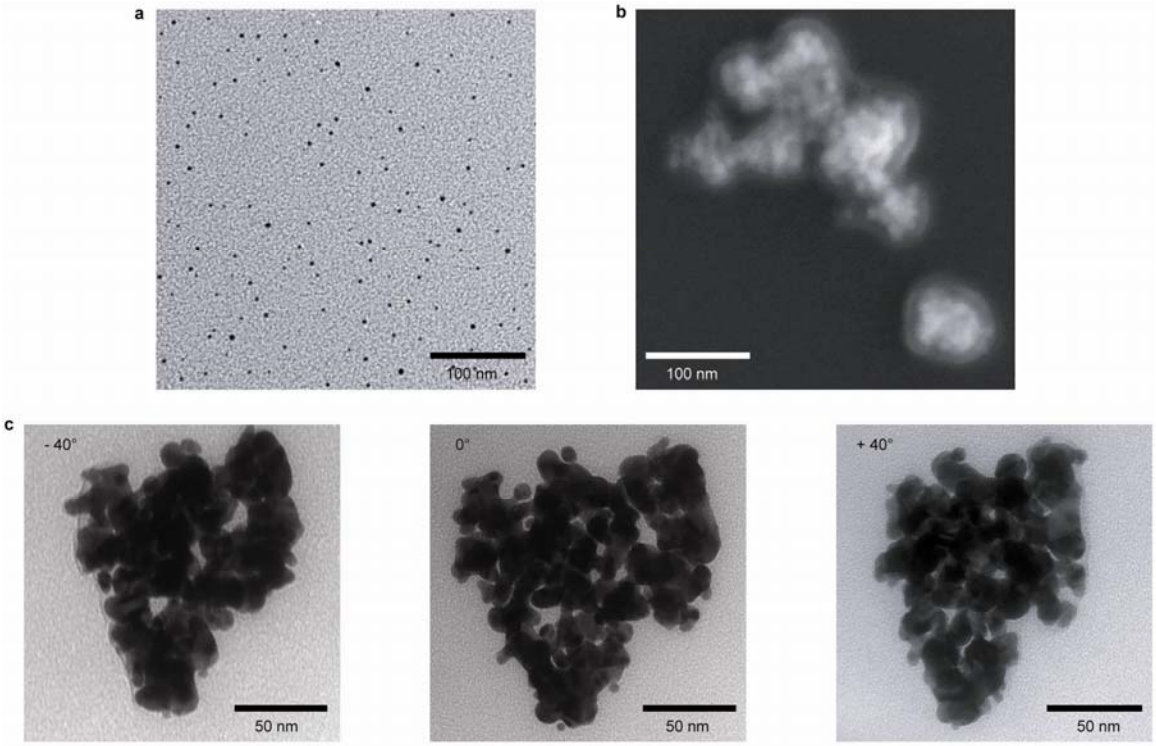

Figure 4.2 Electron microscopy characterization of gold nanoclusters. (a) TEM of initial 4 nm lysine/citrate-capped gold nanoparticles before clustering. (b) SEM and (c) TEM micrographs of nanoclusters template using PLA(2K)-PEG(10K)-PLA(2K) at a 16/1 polymer/Au ratio (w/w). For TEM micrographs, the stage was tilted at an angle of -40, 0 (no tilt), and 40°.

These lysine-capped gold spheres were mixed with the polymer PLA(2K)-PEG(10K)-PLA(2K) yielding a final polymer concentration of 50 mg/mL. The dispersion was sonicated in a water bath for 5 minutes and the dispersion changed from ruby red in color to a darker red-purple color. Upon evaporation of ~80% of the solvent, the dispersion turned blue, indicating absorption in the red wavelength region. Complete solvent evaporation over 2 hours produced a smooth blue film, and reconstitution of the film in deionized (DI) water to a concentration of 0.3 mg/mL yielded a dark blue dispersion.

TABLE 1. Characterization of Gold Primary Particles and Nanoclusters[a]

ligand	absorbance (750 nm)	$D_{avg,primary\ particle}$ (nm)	$D_{avg,cluster,pH=7.4}$ (nm)	$D_{avg,storage,pH=5}$ (nm)
lysine/citrate	1.10	4.1 ± 0.8	83.0 ± 4.6	4.4 ± 0.8
citrate	1.09	4.0 ± 0.8	119.4 ± 22.5	4.0 ± 0.9

Figure 4.3 Summary of absorbance maximum and size of nanoclusters (measured by DLS) and primary particles (measured by TEM) for lysine/citrate and citrate only capped primary gold particles. [a]Absorbance measurement were recorded at gold concentrations of ~56 μg/mL. All nanoclusters were formed using the polymer PLA(2K)-b-PEG(10K)-b-PLA(2K).

SEM was used to determine the nanocluster size of ~ sub-100 nm. A highly scattering core can be seen within a lighter scattering shell indicating the hydrophilic PEG polymer surrounds the assembly of gold nanoparticles in the center of the cluster. This polymer sterically stabilizes the clusters in solution. Additionally, thermogravimetric analysis (TGA) indicated that the nanoclusters contained only 20±5% organic material (polymer and ligands), where 10-15% consisted of polymer. TEM images taken at various angles revealed closely-spaced primary gold nanoparticles throughout the porous cluster. DLS revealed the hydrodynamic diameter to be 83±4.6 nm, which is in agreement with TEM results (Figure 4.3 and Figure 4.4a).

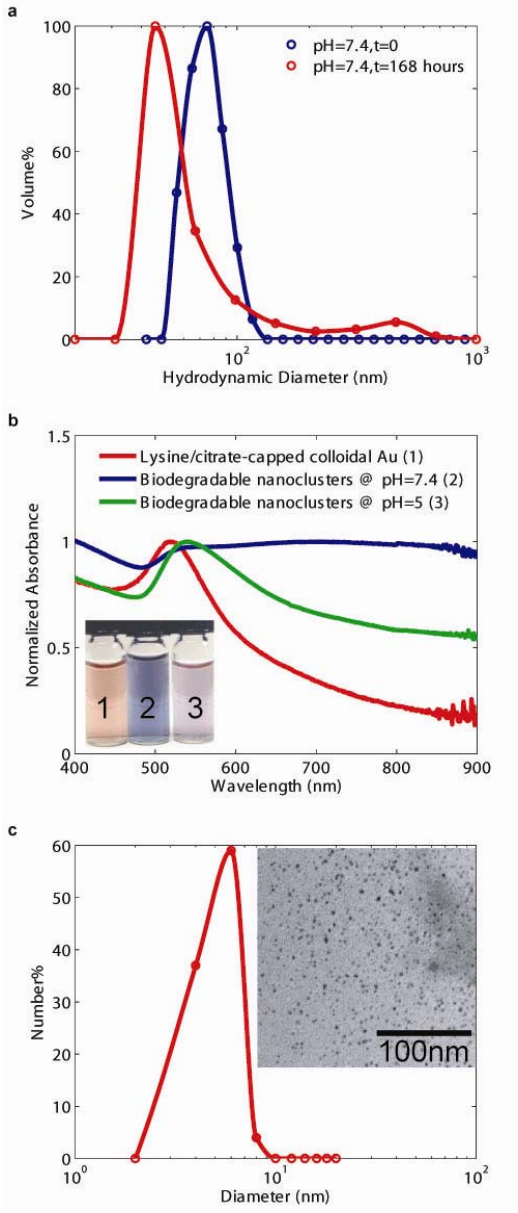

Figure 4.4 Degradation of gold nanoclusters in solution. (a) Hydrodynamic diameter (DLS) in pH 7.4 media initially and after 168 hrs (1 week) of incubation. (b) UV-Vis-NIR absorbance spectra of (1) colloidal dispersion of lysine/citrate-capped gold nanoparticles, (2) biodegradable nanoclusters (pH = 7.4), and (3) deaggregated nanoclusters (pH = 5). (c) Size distribution after deaggregation in pH = 5 media, as determined by image analysis of TEM micrographs (>200 particles). Inset: TEM micrograph of nanoclusters after incubation at pH = 5 for 1 week.

These low polymer loadings allow for close spacing of the primary gold particles. These low loadings are facilitated by control of the depletion forces and the propensity of the PEG blocks to migrate towards the water interface and thus be present mostly on the surface of the cluster. Interparticle distances between the primary particles were estimated to be 1.8±0.6 nm from TEM images (Figure 4.5).

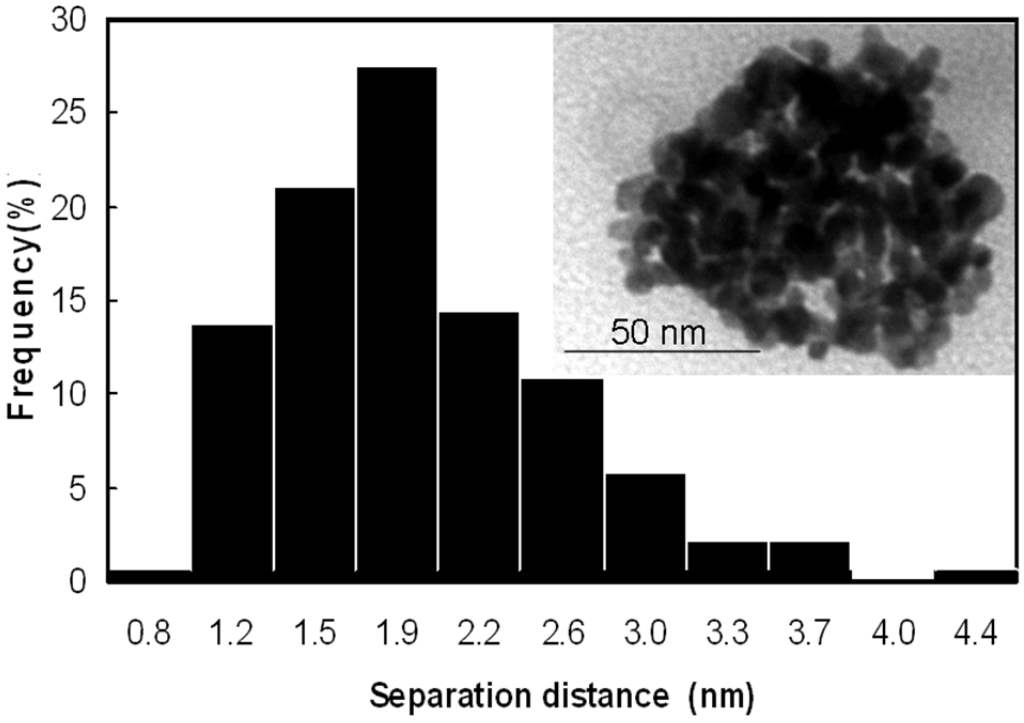

Figure 4.5 Histogram of separation distances between primary gold nanoparticles within a nanocluster. Measurements were taken using particles on the periphery of the nanoclusters. Inset is a TEM image of one of the clusters that was used in this measurement. >130 data points were taken.

This spacing is consistent with the length of a lysine-lysine dipeptide in solution, which is 1.49 nm[229]. The ability to control both cluster size and interparticle spacing was achieved by manipulating the particle volume fractions upon solvent evaporation, and

controlling the electrostatic, van der Waals, depletion, and steric interactions between the gold primary particles and the polymer. This approach provides a large amount of control over nanocluster morphology compared to nanoclusters formed by reducing gold precursors without a polymer stabilizer[230].

4.3.2.2 Optical properties

Optical extinction spectra changed markedly between primary gold spheres and nanoclusters (Figure 4.4b) An initial dispersion of gold nanoparticles had a maximum absorbance at 520 nm, which is characteristic of isolated gold spheres, but upon cluster formation, the absorbance red-shifted and broadened into the NIR region, with a broad maximum spanning 700-900 nm. The extinction cross-section was calculated to be ~10^{-14} m^2, which is comparable to NIR absorbing gold nanoparticles commonly used in biomedical research such as rods[56], cages[220c], and nanoshells[127b].

Extinction cross-section was calculated using Beer-Lambert's Law as given in Equation (4):

$$A = \varepsilon(\lambda)C\iota \qquad (4)$$

Where A is absorbance, ε is the wavelength-dependent extinction coefficient, C is concentration, and ι is the path length. For a path length of 1 cm and a concentration of gold of 56 μg/mL, a maximum absorbance of 1.1 was found at a wavelength of 703 nm. Using Beer-Lambert's Law, the extinction coefficient at 703 nm was 0.02 $cm^2/\mu g$. Assuming that the nanoclusters are spherical and have a diameter of 100 nm, in a closest-packed state, the extinction cross-section (product of extinction coefficient and mass of gold per nanocluster) is ~$1x10^{-14}$ m^2.

The high NIR absorbance observed for nanoclusters can be attributed to multiple factors: close interparticle spacing between primary particles, non-uniform spatial distribution of primary particles, roughness of surface, and a deviation from a spherical shape. TEM images (Figure 4.2)) show that short oligomers of primary particles and subcluster domains can be clearly observed, indicating a non-uniform volume-packing distribution, which has been known to enhance the red-shift of the surface plasmon resonance[76, 231]. The NIR absorbance of the nanoclusters per total particle mass is much higher than previous composite particles with smaller amounts of gold nanoparticles synthesized via templates with liposomes, block copolymer micelles, or DNA[227b, c, 232]. We also demonstrated the assembly of primary gold spheres into nanoclusters with strong NIR absorbance with citrate-capped gold nanoparticles, which possess a zeta-potential of -44±4.9 mV, compared to -30.1±2.4 mV for the lysine/citrate-capped nanoparticles (Figure 4.3). The remainder of this chapter will focus on lysine/citrate-capped nanoclusters because of their smaller size.

4.3.2.3 Stability and degradation in solution

The stability and degradation of nanoclusters were examined at physiologically relevant pHs of 7.4 (normal cell environment) and 5 (endosomal environment[233]). After storing a solution of nanoclusters for 1 week in pH 7.4 buffer, the DLS peak shifted modestly toward smaller sizes (Figure 4.4a). This limited degradation is consistent with the long half-life of PLA(MW 2K) of about 4 weeks at neutral pH. In contrast, after nanoclusters were incubated in a pH of 5 (a medium of 0.1N HCl) for 1 week, near complete degradation of the nanoclusters was observed by TEM (Figure 4.4c and Figure 4.3). The mean particle size of degraded clusters was 4.3±0.1 nm (n>100 particles), which was comparable to the initial particle size of 4.1±0.8 nm (Figure 4.6).

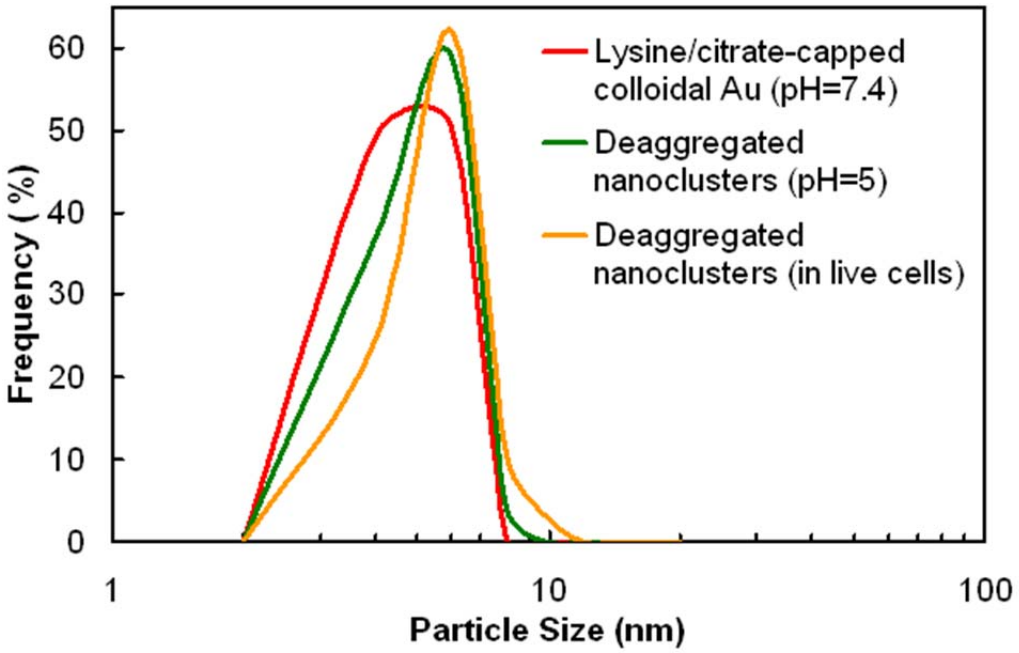

Figure 4.6 Particle size distribution of primary lysine/citrate-capped gold particles (red curve), nanoclusters deaggregated at pH=5 (green curve), and nanoclusters after biodegradation in live cells (orange curve) determined by image analysis of over 100 particles per sample in TEM micrographs.

Upon degradation of the polymer, a combination of steric repulsion because of capping ligands and remaining polymer fragments, electrostatic repulsion because of negative charge of gold nanoparticles, and effective entropic forces are sufficient to completely redisperse the primary gold particles. The extinction spectrum of the colloidal gold spheres blue-shifts towards the spectrum of primary particles and the color of the solution changes back towards red (Figure 4.4b). The remaining discrepancy between these spectra is attributed to the presence of a small number of clusters (~7%) still present in the degraded solution. More recent work, however, has shown that smaller 20 and 30 nm clusters have eliminated this secondary population of larger non-degrading particles.

Degradation of nanoclusters consisting of citrate-capped primary particles was also achieved.

4.3.2.4 Degradation in cells

Nanocluster biodegradation was then demonstrated in macrophage cells, a common model cell type for any clearance organ. Scattering spectra and hyperspectral (HS) images (Figure 4.7a,c), dark-field reflectance (DR) images (Figure 4.7b,d top row), and HS images (Figure 4.7b,d bottom row) were acquired at 24, 96, and 168 hrs after cells were treated with nanoclusters.

High nanocluster uptake was observed in the DR images, where nanoclusters strongly scattered the illuminated light. Overall scattering intensity decreased over time as macrophages divided and nanoclusters were distributed between daughter cells (Figure 4.7b, top row). A significant increase in red-NIR scattering signal of the labeled cells was seen compared to unlabeled cells (compared Figure 4.7a, dark blue curve and c), consistent with the high scattering of clusters in solution (Figure 4.7a, light blue curve).

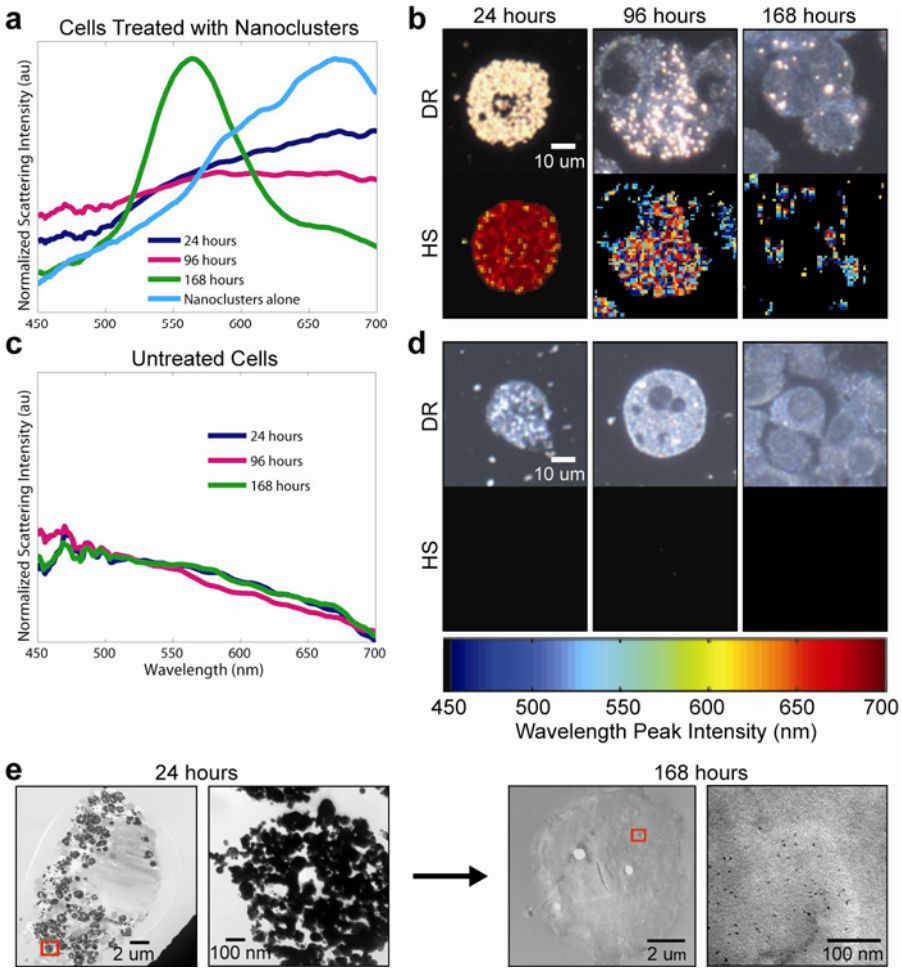

Figure 4.7 Biodegradation of gold nanoclusters inside live cells. Scattering spectra (normalized by area under the curve) of (a) live cells labeled with nanoclusters and (c) control cells without nanoclusters. The spectra were taken at 24, 96, and 168 hrs after cells were treated with nanoclusters. Dark-field reflectance (DR) images of cells treated with (b) nanoclusters and (d) control cells over time are shown together with corresponding color coded images indicating scattering peak position at each pixel in the field of view (b and d, bottom rows). Hyperspectral (HS) images and the color bar were used to obtain the color coded distribution of scattering peaks within cells (b and d, bottom row). Pixels that did not have an identifiable peak in a corresponding spectrum were not assigned a color. The scale bar in the DR and HS images is 10 μm. (e) TEM images of cells treated with nanoclusters at low magnification (scale bar 2 μm) and high magnification (scale bar 100 nm) at 24 and 168 hrs. Red boxes in the low magnification images are magnified on the right at each time point.

The relative intensity of the red-NIR scattering signal decreased after 96 hrs, and the scattering from labeled cells showed a marked blue shift to 550 nm, which is consistent with scattering from constituent lysine-citrate-capped gold nanoparticles (Figure 4.8).

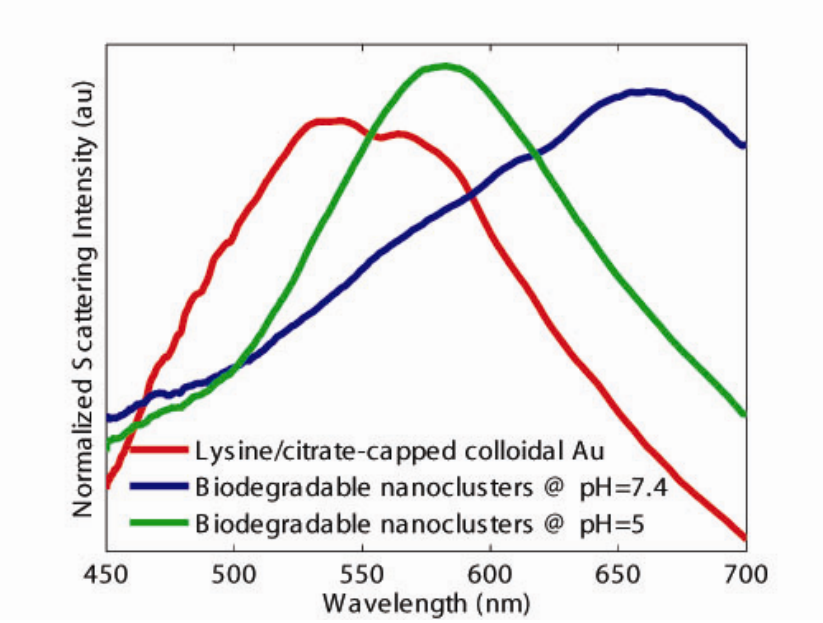

Figure 4.8 Hyperspectral scattering spectra (normalized to the area under the curve) of biodegradable nanoclusters at pH=7.4 (dark-blue curve), deaggregated nanoclusters at pH=5 (green curve), and the primary lysine/citrate-capped colloidal gold (red curve).

Hyperspectral images showed a gradual progression from very strong scattering in the 650-700 nm region at t=24 hrs to a less intense scattering signal predominantly in the 500-550 nm region at t=168 hrs (Figure 4.7b, bottom row). The endogenous scattering from control untreated cells did not significantly change over time (Figure 4.7c,d). Note that the scattering from the control cells is approximately 6 times weaker than scattering from labeled cells. Additionally, most of the pixels in the HS image of untreated cells do

not exhibit any distinct scattering peaks, which result in a black appearance in the images in Figure 4.7d, bottom row. The biodegradation of nanoclusters inside live cells was further confirmed by TEM (Figure 4.7e). After 24 hrs, large ~100 nm clusters can be observed throughout the interior of cells (Figure 4.7e, 24 hrs), whereas after 168 hrs, cells contain only particles less than 5 nm (Figure 4.7e, 168 hrs). These TEM results are in excellent agreement with the optical measurements and with results in solution, providing unambiguous proof that the nanoclusters are achieving complete biodegradation of the initial 100 nm nanoclusters into sub-5 nm primary particles (Figure 4.6).

4.4 Animal studies

The in vivo behavior of nanoclusters was investigated in normal Balb/c mice. Mice were injected via tail vein with 200 μL of 6 mg/mL of either 40 nm biodegradable gold nanoclusters or 10kD PEGylated 40 nm non-degrading gold particles in phenol-free DMEM media. Mice injected with PBS were used as a control. Tissues were harvested for inductively coupled plasma mass spectrometry (ICP-MS) analysis at time points: 1 day, 1 week (7 days), 1 month (28 days), 2 months (56 days), 3 months (84 days),and 4 months (112 days) after injection.

Biodistribution results revealed that both biodegradable nanoclusters and non-degrading solid spheres accumulated significantly (~70% injected dose) in clearance organs: liver, spleen, and kidney by the initial time point of 1 day, as expected (Figure 4.9). Control PBS-injected mice did not yield any gold in these organs. Over time, both non-degrading solid spheres and biodegradable nanoclusters cleared from these clearance organs at a similar rate until the final time point of 4 months (112 days), where the concentration of nanoclusters dropped markedly compared to non-degrading spheres.

These results indicate that even though initial clearance is fairly slow, the nanoclusters will clear the body faster than non-degrading particles.

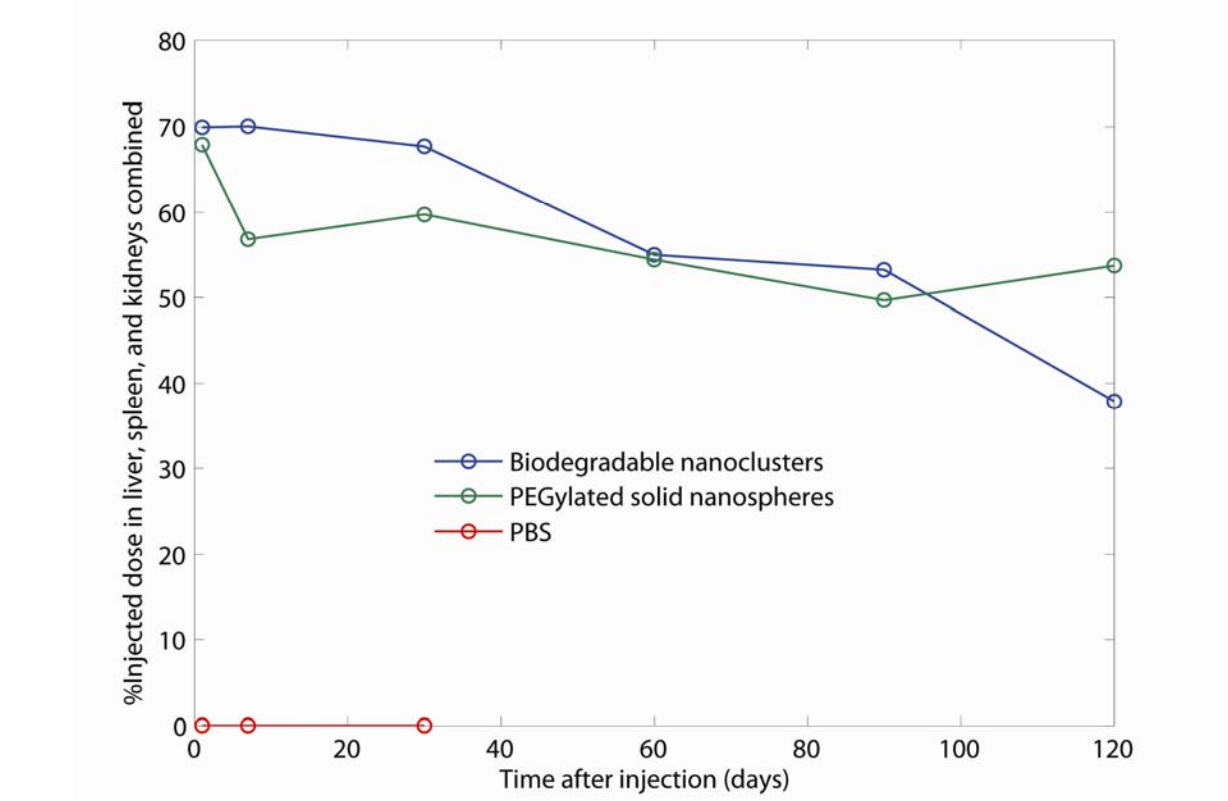

Figure 4.9 % Injected dose (ID) of gold found in clearance organs: liver, spleen, and kidneys, combined, over time. Both clusters (blue curve) and solids (red curve) showed a drop in gold content in clearance organs over time. Clusters, however, exhibited a larger drop than solids at the final time point of 112 days (4 months). PBS-injected mice were used as a negative control and did not show gold content in clearance organs. Control mice were only analyzed up to a third time point (1 month after injection).

While the accumulation of the biodegradable nanoclusters and the non-degrading spheres was very similar in all of the clearance organs (liver, spleen, and kidneys) combined over time, the distribution between individual clearance organs was

significantly different for the two particle types even at initial time points (Figure 4.10). Nanoclusters initially accumulated mostly in the liver (~70% injected dose (ID)) with very little accumulation in the spleen (2% ID) or kidneys (0.2% ID). In contrast, non-degrading spheres distributed more evenly between the clearance organs, with ~40% ID found in the liver after 1 day, 24% ID in the spleen, and 3% ID found in the kidneys (Figure 4.10). This significant difference in distribution between nanoclusters and non-degrading spheres has been observed with other types of particles. Perry and colleagues showed that non-PEGylated nanoparticles accumulated mostly in the liver, while PEGylated nanoparticles accumulated more evenly between both liver and spleen[96]. The hypothesis for this difference was that PEGylated particles, which can circulate longer than non-PEGylated particles, have more time to interact with the spleen, while particles with shorter circulation time interact initially with liver[96]. This effect can be explored for future studies with the aim of avoiding both clearance organs.

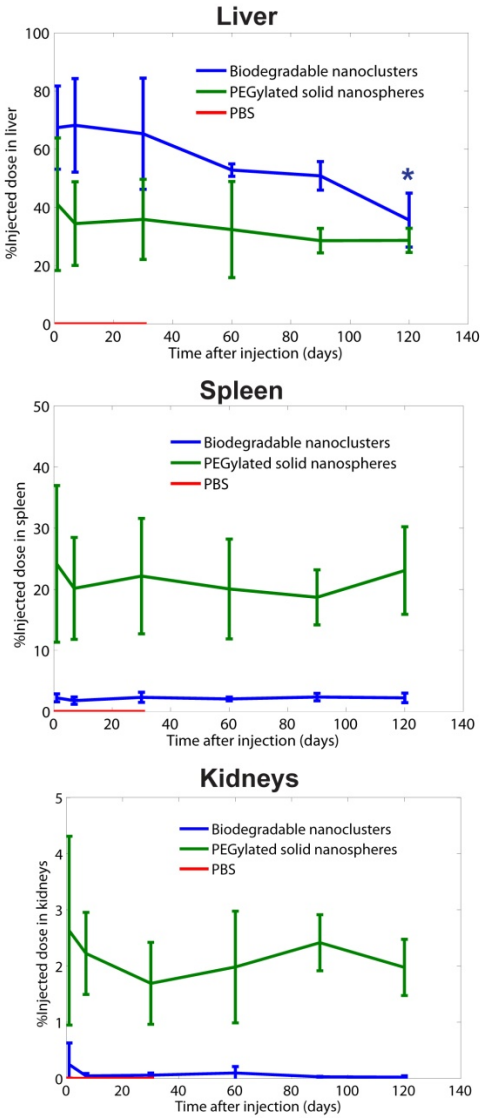

Figure 4.10 %Injected dose (ID) of gold from biodegradable 40 nm clusters (blue curves), solid non-degrading 40nm (red curves), and control PBS (green curves) injected in mice. Organs analyzed over time were: liver (top), spleen (middle), and kidney s (bottom). A significant drop in gold was observed in the liver of mice injected with nanoclusters after 4 months compared to initial time points 1, 7, and 30 days after injection (blue curve, top graph) (*$p<0.05$). No other curves showed a significant change over time. Clusters accumulated mostly in the liver, while solids were more evenly distributed between the liver, spleen, and kidneys.

Nanoclusters in the liver showed a significant decrease ($p<0.05$) after 4 months, while non-degrading spheres did not exhibit any significant change over time. Moreover, neither particles in the spleen nor kidneys showed any change over time. The significant drop in concentration of clusters from the liver compared to non-degrading particles is promising for more optimized clusters to clear at an even faster rate from the body. For future studies, to increase rate of clearance of nanoclusters in vivo, smaller 20nm nanoclusters will be explored[234]. These nanoclusters show no opsonization in serum for both intact and degraded nanoclusters[235] and show promise to clear at a fast rate from the body than the previously studies 40 nm nanoclusters.

4.5 Conclusions and Discussion

We have developed a general kinetic assembly platform for the design of hybrid polymer/gold nanoclusters smaller than 100 nm with closely-spaced gold spheres that produce strong absorbance in the NIR. Only small amounts of biodegradable polymers are needed to reduce electrostatic repulsion between gold particles to stabilize the clusters. These nanoclusters have both high optical cross-sections required for imaging and therapy, prolonged blood residence time required for effective targeting to a diseased site, and ability to be degraded into efficiently clearable components which is required for minimizing exposure of the agent to the body in the long-term, thus minimizing potential toxic effects. This method of assembling primary gold particles can serve as a platform for tuning parameters such as varying surface chemistries, which play a large role in clearance, or synthesizing an assembly comprised of multiple types of materials to allow for multimodal imaging and multifunctional applications such as targeting and therapy.

The combination of all these tunable parameters can be explored to facilitate translating plasmonic nanoparticles to the clinic.

Chapter 5: Conclusions and Future Work

5.1 Conclusions

Chapter 2 described properties of gold nanoparticles that make this nanoparticle an attractive sensing, imaging, and therapeutic agent. Gold nanoparticles have consistently shown strong optical imaging capabilities because of high optical cross-sections compared to conventional clinically used imaging agents: fluorophores and organic dyes. Also, these nanoparticles can be of the size to allow for fairly long blood residence time and thus have served as delivery vehicles for targeting agents and drugs. One area of concern, however, is the fact that even though there is an abundance of research in developing stealthy and targeted nanoparticles, many nanoparticles are still cleared from the bloodstream by the MPS. This fact is further complicated by the fact that inorganic nanoparticles such as gold do not degrade and thus can have a potential of causing long-term negative side effects in vital organs.

Chapter 3 demonstrated that by conjugating a therapeutic antibody to the surface of a nanoparticle, the therapeutic efficacy of the therapeutic molecule was increased compared to free antibody, via a multivalent effect, which has been demonstrate numerous times to enhance binding affinity of molecules. Additionally, cell death pathways that were activated by this therapeutic conjugate were shown to be a combination of the known programmed cell death pathways: autophagy and apoptosis, giving us a better understanding of how our treatment is working. These pathways were not activated using individual components of the conjugate, showing that the assembly of the conjugates provides a unique therapeutic enhancement to components that have been studied more extensively on their own. This conjugate was also comprised of multiple

materials to allow for multimodal imaging, which many think will be the next area of major advancement towards personalized medicine.

Chapter 4 provided a method of developing plasmonic particles that were both large enough to have strong optical cross sections and as long of a circulation time that a particle of this size can have, and over time, small enough to be of the size that is renally and efficiently clearable. We showed that these particles degrade in cells to primary components within a week, and even showed degradation within mice, but over a much longer time frame, over the course of many months. These results showed that these particles have potential to be efficiently cleared. Additionally, these particles have strong NIR absorbance for high resolution, NIR imaging in vivo and are composed of multiple primary components, lending itself to have multifunctional and multimodal capabilities.

5.2 FUTURE WORK

5.2.1 Therapeutic efficacy

Therapeutic molecules like therapeutic antibodies conjugated to plasmonic particles have the unique opportunity to convey a high degree of functionality in a small system. Future work for these conjugates involves determining therapeutic efficacy of the conjugates in vivo. Therapeutic efficacy of the therapeutic molecules alone has been demonstrated by other groups to be highly effective at inhibiting tumor growth at certain concentrations, and these plasmonic hybrid conjugates provide a way to not only monitor these therapeutic molecules in vivo but also to enhance the therapeutic effect of these therapeutic molecules. A major challenge to delivering a large load of drugs or imaging agents to a diseased site in the body is the immune system of the body. Thus, optimizing particle size, charge, and composition will be essential to using these particles in vivo. Additionally, determining cell signaling paths and molecules that are activated by these

conjugates will lead to the development of the conjugates as a platform to be translated to an individual patient's needs.

5.2.2 Clearance of nanoparticles

The clearance of degradable plasmonic nanoclusters will rely on fully characterizing the nanoparticles' interactions with the body's host blood and immune system. Previous reports have indicated the range of sizes and charges of inorganic nanoparticles that can be efficiently cleared, but combining these traits with other essential traits like high absorbance cross sections for imaging and being initially of the size to allow for prolonged blood circulation complicates the scenario and requires a new set of characterizations.

Overall, plasmonic nanoparticles provide a strong multifunctional platform for imaging and treating diseases like cancer, but before they can be translated to the clinic, their interactions with the body's defense system must be fully characterized which can help in developing particles with increased stability and stealth. This, then, can greatly affect other important properties biomedical nanoparticles strive to have, such as increased targeting and clearance over time.

References

1. Siegel, R.; Naishadham, D.; Jemal, A., Cancer Statistics, 2012. *Ca-Cancer J Clin* **2012,** *62* (1), 10-29.
2. Hanahan, D.; Weinberg, R. A., The hallmarks of cancer. *Cell* **2000,** *100* (1), 57-70.
3. http://www.cancer.gov/cancertopics/wyntk/cancer. **2012**.
4. Tearney, G. J.; Brezinski, M. E.; Bouma, B. E.; Boppart, S. A.; Pitris, C.; Southern, J. F.; Fujimoto, J. G., In vivo endoscopic optical biopsy with optical coherence tomography. *Science* **1997,** *276* (5321), 2037-2039.
5. http://www.cancer.gov/cancertopics/factsheet/Therapy/targeted. **2012**.
6. He, T. C.; Sparks, A. B.; Rago, C.; Hermeking, H.; Zawel, L.; da Costa, L. T.; Morin, P. J.; Vogelstein, B.; Kinzler, K. W., Identification of c-MYC as a target of the APC pathway. *Science* **1998,** *281* (5382), 1509-1512.
7. Mantovani, A.; Allavena, P.; Sica, A.; Balkwill, F., Cancer-related inflammation. *Nature* **2008,** *454* (7203), 436-444.
8. Pikarsky, E.; Porat, R. M.; Stein, I.; Abramovitch, R.; Amit, S.; Kasem, S.; Gutkovich-Pyest, E.; Urieli-Shoval, S.; Galun, E.; Ben-Neriah, Y., NF-kappa B functions as a tumour promoter in inflammation-associated cancer. *Nature* **2004,** *431* (7007), 461-466.
9. Yu, H.; Jove, R., The stats of cancer - New molecular targets come of age. *Nat. Rev. Cancer* **2004,** *4* (2), 97-105.
10. Banerjee, S. K.; Sarkar, D. K.; Weston, A. P.; De, A.; Campbell, D. R., Over expression of vascular endothelial growth factor and its receptor during the development of estrogen-induced rat pituitary tumors may mediate estrogen-initiated tumor angiogenesis. *Carcinogenesis* **1997,** *18* (6), 1155-1161.
11. Lynch, T. J.; Bell, D. W.; Sordella, R.; Gurubhagavatula, S.; Okimoto, R. A.; Brannigan, B. W.; Harris, P. L.; Haserlat, S. M.; Supko, J. G.; Haluska, F. G.; Louis, D. N.; Christiani, D. C.; Settleman, J.; Haber, D. A., Activating mutations in the epidermal growth factor receptor underlying responsiveness of non-small-cell lung cancer to gefitinib. *N. Engl. J. Med.* **2004,** *350* (21), 2129-2139.
12. Hynes, N. E.; Lane, H. A., ERBB receptors and cancer: The complexity of targeted inhibitors. *Nat. Rev. Cancer* **2005,** *5* (5), 341-354.
13. Sato, J. D.; Kawamoto, T.; Le, A. D.; Mendelsohn, J.; Polikoff, J.; Sato, G. H., Biological effects in vitro of monoclonal antibodies to human epidermal growth factor receptors. *Mol. Biol. Med.* **1983,** *1* (Copyright (C) 2012 American Chemical Society (ACS). All Rights Reserved.), 511-29.
14. (a) Van Cutsem, E.; Kohne, C. H.; Hitre, E.; Zaluski, J.; Chien, C. R. C.; Makhson, A.; D'Haens, G.; Pinter, T.; Lim, R.; Bodoky, G.; Roh, J. K.; Folprecht, G.; Ruff, P.; Stroh, C.; Tejpar, S.; Schlichting, M.; Nippgen, J.; Rougier, P., Cetuximab and

Chemotherapy as Initial Treatment for Metastatic Colorectal Cancer. *N. Engl. J. Med.* **2009,** *360* (14), 1408-1417; (b) Bokemeyer, C.; Bondarenko, I.; Makhson, A.; Hartmann, J. T.; Aparicio, J.; de Braud, F.; Donea, S.; Ludwig, H.; Schuch, G.; Stroh, C.; Loos, A. H.; Zubel, A.; Koralewski, P., Fluorouracil, Leucovorin, and Oxaliplatin With and Without Cetuximab in the First-Line Treatment of Metastatic Colorectal Cancer. *Journal of Clinical Oncology* **2009,** *27* (5), 663-671.
15. Merchan, J. R.; Ferrell, A.; Macintyre, J.; Ciombor, K. K.; Levi, J.; Ribeiro, A.; Sleeman, D.; Flores, A.; Lopes, G.; Rocha-Lima, C. M., Phase II Study of Gemcitabine, Oxaliplatin, and Cetuximab in Advanced Pancreatic Cancer. *Am. J. Clin. Oncol.-Cancer Clin. Trials* **2012,** *35* (5), 446-450.
16. Yonesaka, K.; Zejnullahu, K.; Okamoto, I.; Satoh, T.; Cappuzzo, F.; Souglakos, J.; Ercan, D.; Rogers, A.; Roncalli, M.; Takeda, M.; Fujisaka, Y.; Philips, J.; Shimizu, T.; Maenishi, O.; Cho, Y. G.; Sun, J. S.; Destro, A.; Taira, K.; Takeda, K.; Okabe, T.; Swanson, J.; Itoh, H.; Takada, M.; Lifshits, E.; Okuno, K.; Engelman, J. A.; Shivdasani, R. A.; Nishio, K.; Fukuoka, M.; Varella-Garcia, M.; Nakagawa, K.; Janne, P. A., Activation of ERBB2 Signaling Causes Resistance to the EGFR-Directed Therapeutic Antibody Cetuximab. *Sci. Transl. Med.* **2011,** *3* (99).
17. Brigger, I.; Dubernet, C.; Couvreur, P., Nanoparticles in cancer therapy and diagnosis. *Advanced Drug Delivery Reviews* **2002,** *54* (5), 631-651.
18. Links, M.; Brown, R., Clinical relevance of the molecular mechanisms of resistance to anti-cancer drugs. *Expert Rev. Mol. Med.* **1999,** (Copyright (C) 2012 American Chemical Society (ACS). All Rights Reserved.), No pp. given.
19. Krishna, R.; Mayer, L. D., Multidrug resistance (MDR) in cancer - Mechanisms, reversal using modulators of MDR and the role of MDR modulators in influencing the pharmacokinetics of anticancer drugs. *European Journal of Pharmaceutical Sciences* **2000,** *11* (4), 265-283.
20. Yuan, F., Transvascular drug delivery in solid tumors. *Seminars in Radiation Oncology* **1998,** *8* (3), 164-175.
21. Moghimi, S. M.; Hunter, A. C.; Murray, J. C., Long-circulating and target-specific nanoparticles: Theory to practice. *Pharmacological Reviews* **2001,** *53* (2), 283-318.
22. Peer, D.; Karp, J. M.; Hong, S.; FaroKhzad, O. C.; Margalit, R.; Langer, R., Nanocarriers as an emerging platform for cancer therapy. *Nature Nanotechnology* **2007,** *2* (12), 751-760.
23. Couvreur, P.; Kante, B.; Roland, M.; Speiser, P., ADSORPTION OF ANTI-NEOPLASTIC DRUGS TO POLYALKYLCYANOACRYLATE NANOPARTICLES AND THEIR RELEASE IN CALF SERUM. *Journal of Pharmaceutical Sciences* **1979,** *68* (12), 1521-1524.
24. Duncan, R., Polymer conjugates as anticancer nanomedicines. *Nat. Rev. Cancer* **2006,** *6* (9), 688-701.
25. (a) Yuan, F.; Dellian, M.; Fukumura, D.; Leunig, M.; Berk, D. A.; Torchilin, V. P.; Jain, R. K., VASCULAR-PERMEABILITY IN A HUMAN TUMOR XENOGRAFT - MOLECULAR-SIZE DEPENDENCE AND CUTOFF SIZE. *Cancer Research* **1995,**

55 (17), 3752-3756; (b) Torchilin, V. P., Recent advances with liposomes as pharmaceutical carriers. *Nat. Rev. Drug Discov.* **2005,** *4* (2), 145-160; (c) Hobbs, S. K.; Monsky, W. L.; Yuan, F.; Roberts, W. G.; Griffith, L.; Torchilin, V. P.; Jain, R. K., Regulation of transport pathways in tumor vessels: Role of tumor type and microenvironment. *Proc. Natl. Acad. Sci. U. S. A.* **1998,** *95* (8), 4607-4612.
26. Kreuter, J.; Higuchi, T., IMPROVED DELIVERY OF METHOXSALEN. *Journal of Pharmaceutical Sciences* **1979,** *68* (4), 451-454.
27. (a) Couvreur, P.; Vauthier, C., Nanotechnology: Intelligent design to treat complex disease. *Pharmaceutical Research* **2006,** *23* (7), 1417-1450; (b) Lee, K. S.; Chung, H. C.; Im, S. A.; Park, Y. H.; Kim, C. S.; Kim, S. B.; Rha, S. Y.; Lee, M. Y.; Ro, J., Multicenter phase II trial of Genexol-PM, a Cremophor-free, polymeric micelle formulation of paclitaxel, in patients with metastatic breast cancer. *Breast Cancer Research and Treatment* **2008,** *108* (2), 241-250.
28. Wu, X. Y.; Liu, H. J.; Liu, J. Q.; Haley, K. N.; Treadway, J. A.; Larson, J. P.; Ge, N. F.; Peale, F.; Bruchez, M. P., Immunofluorescent labeling of cancer marker Her2 and other cellular targets with semiconductor quantum dots. *Nat. Biotechnol.* **2003,** *21* (1), 41-46.
29. Gao, X. H.; Cui, Y. Y.; Levenson, R. M.; Chung, L. W. K.; Nie, S. M., In vivo cancer targeting and imaging with semiconductor quantum dots. *Nat. Biotechnol.* **2004,** *22* (8), 969-976.
30. (a) Dabbousi, B. O.; RodriguezViejo, J.; Mikulec, F. V.; Heine, J. R.; Mattoussi, H.; Ober, R.; Jensen, K. F.; Bawendi, M. G., (CdSe)ZnS core-shell quantum dots: Synthesis and characterization of a size series of highly luminescent nanocrystallites. *Journal of Physical Chemistry B* **1997,** *101* (46), 9463-9475; (b) Leatherdale, C. A.; Woo, W. K.; Mikulec, F. V.; Bawendi, M. G., On the absorption cross section of CdSe nanocrystal quantum dots. *Journal of Physical Chemistry B* **2002,** *106* (31), 7619-7622.
31. Medintz, I. L.; Uyeda, H. T.; Goldman, E. R.; Mattoussi, H., Quantum dot bioconjugates for imaging, labelling and sensing. *Nature Materials* **2005,** *4* (6), 435-446.
32. (a) Efros, A. L., INTERBAND ABSORPTION OF LIGHT IN A SEMICONDUCTOR SPHERE. *Soviet Physics Semiconductors-Ussr* **1982,** *16* (7), 772-775; (b) Ekimov, A. I.; Onushchenko, A. A., QUANTUM SIZE EFFECT IN THE OPTICAL-SPECTRA OF SEMICONDUCTOR MICRO-CRYSTALS. *Soviet Physics Semiconductors-Ussr* **1982,** *16* (7), 775-778.
33. (a) Gao, X. H.; Nie, S. M., Molecular profiling of single cells and tissue specimens with quantum dots. *Trends in Biotechnology* **2003,** *21* (9), 371-373; (b) Jovin, T. M., Quantum dots finally come of age. *Nat. Biotechnol.* **2003,** *21* (1), 32-33.
34. Lee, K. H.; Galloway, J. F.; Park, J.; Dvoracek, C. M.; Dallas, M.; Konstantopoulos, K.; Maitra, A.; Searson, P. C., Quantitative molecular profiling of biomarkers for pancreatic cancer with functionalized quantum dots. *Nanomed.-Nanotechnol. Biol. Med.* **2012,** *8* (7), 1043-1051.
35. (a) Kim, S.; Lim, Y. T.; Soltesz, E. G.; De Grand, A. M.; Lee, J.; Nakayama, A.; Parker, J. A.; Mihaljevic, T.; Laurence, R. G.; Dor, D. M.; Cohn, L. H.; Bawendi, M. G.; Frangioni, J. V., Near-infrared fluorescent type II quantum dots for sentinel lymph node

mapping. *Nat. Biotechnol.* **2004,** *22* (1), 93-97; (b) Ruan, J.; Song, H.; Qian, Q. R.; Li, C.; Wang, K.; Bao, C. C.; Cui, D. X., HER2 monoclonal antibody conjugated RNase-A-associated CdTe quantum dots for targeted imaging and therapy of gastric cancer. *Biomaterials* **2012,** *33* (29), 7093-7102; (c) Yang, Y. L.; An, F. F.; Liu, Z.; Zhang, X. J.; Zhou, M. J.; Li, W.; Hao, X. J.; Lee, C. S.; Zhang, X. H., Ultrabright and ultrastable near-infrared dye nanoparticles for in vitro and in vivo bioimaging. *Biomaterials* **2012,** *33* (31), 7803-7809.

36. (a) Chu, M. Q.; Pan, X. J.; Zhang, D.; Wu, Q.; Peng, J. L.; Hai, W. X., The therapeutic efficacy of CdTe and CdSe quantum dots for photothermal cancer therapy. *Biomaterials* **2012,** *33* (29), 7071-7083; (b) Jia, X.; Jia, L., Nanoparticles Improve Biological Functions of Phthalocyanine Photosensitizers Used for Photodynamic Therapy. *Curr. Drug Metab.* **2012,** *13* (8), 1119-1122; (c) Markovic, Z. M.; Ristic, B. Z.; Arsikin, K. M.; Klisic, D. G.; Harhaji-Trajkovic, L. M.; Todorovic-Markovic, B. M.; Kepic, D. P.; Kravic-Stevovic, T. K.; Jovanovic, S. P.; Milenkovic, M. M.; Milivojevic, D. D.; Bumbasirevic, V. Z.; Dramicanin, M. D.; Trajkovic, V. S., Graphene quantum dots as autophagy-inducing photodynamic agents. *Biomaterials* **2012,** *33* (29), 7084-7092.

37. Ballou, B.; Lagerholm, B. C.; Ernst, L. A.; Bruchez, M. P.; Waggoner, A. S., Noninvasive imaging of quantum dots in mice. *Bioconjugate Chemistry* **2004,** *15* (1), 79-86.

38. Mornet, S.; Vasseur, S.; Grasset, F.; Duguet, E., Magnetic nanoparticle design for medical diagnosis and therapy. *J. Mater. Chem.* **2004,** *14* (14), 2161-2175.

39. Weissleder, R.; Elizondo, G.; Wittenberg, J.; Rabito, C. A.; Bengele, H. H.; Josephson, L., ULTRASMALL SUPERPARAMAGNETIC IRON-OXIDE - CHARACTERIZATION OF A NEW CLASS OF CONTRAST AGENTS FOR MR IMAGING. *Radiology* **1990,** *175* (2), 489-493.

40. Pankhurst, Q. A.; Connolly, J.; Jones, S. K.; Dobson, J., Applications of magnetic nanoparticles in biomedicine. *J. Phys. D-Appl. Phys.* **2003,** *36* (13), R167-R181.

41. Na, H. B.; Song, I. C.; Hyeon, T., Inorganic Nanoparticles for MRI Contrast Agents. *Adv. Mater.* **2009,** *21* (21), 2133-2148.

42. Jordan, A.; Scholz, R.; Wust, P.; Fahling, H.; Felix, R., Magnetic fluid hyperthermia (MFH): Cancer treatment with AC magnetic field induced excitation of biocompatible superparamagnetic nanoparticles. *Journal of Magnetism and Magnetic Materials* **1999,** *201*, 413-419.

43. Hoshino, K.; Huang, Y. Y.; Lane, N.; Huebschman, M.; Uhr, J. W.; Frenkel, E. P.; Zhang, X. J., Microchip-based immunomagnetic detection of circulating tumor cells. *Lab Chip* **2011,** *11* (20), 3449-3457.

44. Longmire, M.; Choyke, P. L.; Kobayashi, H., Clearance properties of nano-sized particles and molecules as imaging agents: considerations and caveats. *Nanomedicine* **2008,** *3* (5), 703-717.

45. Cagle, D. W.; Kennel, S. J.; Mirzadeh, S.; Alford, J. M.; Wilson, L. J., In vivo studies of fullerene-based materials using endohedral metallofullerene radiotracers. *Proc. Natl. Acad. Sci. U. S. A.* **1999,** *96* (9), 5182-5187.

46. Bolskar, R. D.; Benedetto, A. F.; Husebo, L. O.; Price, R. E.; Jackson, E. F.; Wallace, S.; Wilson, L. J.; Alford, J. M., First soluble M@C-60 derivatives provide enhanced access to metallofullerenes and permit in vivo evaluation of Gd@C-60 C(COOH)(2) (10) as a MRI contrast agent. *Journal of the American Chemical Society* **2003,** *125* (18), 5471-5478.
47. Faulk, W. P.; Taylor, G. M., IMMUNOCOLLOID METHOD FOR ELECTRON MICROSCOPE. *Immunochemistry* **1971,** *8* (11), 1081-&.
48. (a) El-Sayed, I. H.; Huang, X. H.; El-Sayed, M. A., Surface plasmon resonance scattering and absorption of anti-EGFR antibody conjugated gold nanoparticles in cancer diagnostics: Applications in oral cancer. *Nano Lett.* **2005,** *5* (5), 829-834; (b) Grainger, R. G., INTRAVASCULAR CONTRAST-MEDIA - THE PAST, THE PRESENT AND THE FUTURE. *British Journal of Radiology* **1982,** *55* (649), 1-18; (c) Sokolov, K.; Follen, M.; Aaron, J.; Pavlova, I.; Malpica, A.; Lotan, R.; Richards-Kortum, R., Real-time vital optical imaging of precancer using anti-epidermal growth factor receptor antibodies conjugated to gold nanoparticles. *Cancer Research* **2003,** *63* (9), 1999-2004; (d) Wang, Y. W.; Xie, X. Y.; Wang, X. D.; Ku, G.; Gill, K. L.; O'Neal, D. P.; Stoica, G.; Wang, L. V., Photoacoustic tomography of a nanoshell contrast agent in the in vivo rat brain. *Nano Lett.* **2004,** *4* (9), 1689-1692; (e) Yelin, D.; Oron, D.; Thiberge, S.; Moses, E.; Silberberg, Y., Multiphoton plasmon-resonance microscopy. *Optics Express* **2003,** *11* (12), 1385-1391.
49. Huang, X. H.; Jain, P. K.; El-Sayed, I. H.; El-Sayed, M. A., Gold nanoparticles: interesting optical properties and recent applications in cancer diagnostic and therapy. *Nanomedicine* **2007,** *2* (5), 681-693.
50. Turkevich, J.; Stevenson, P. C.; Hillier, J., A STUDY OF THE NUCLEATION AND GROWTH PROCESSES IN THE SYNTHESIS OF COLLOIDAL GOLD. *Discussions of the Faraday Society* **1951,** (11), 55-&.
51. Boisselier, E.; Astruc, D., Gold nanoparticles in nanomedicine: preparations, imaging, diagnostics, therapies and toxicity. *Chem. Soc. Rev.* **2009,** *38* (6), 1759-1782.
52. Stewart, M. E.; Anderton, C. R.; Thompson, L. B.; Maria, J.; Gray, S. K.; Rogers, J. A.; Nuzzo, R. G., Nanostructured plasmonic sensors. *Chem. Rev.* **2008,** *108* (2), 494-521.
53. Klaus, T.; Joerger, R.; Olsson, E.; Granqvist, C. G., Silver-based crystalline nanoparticles, microbially fabricated. *Proc. Natl. Acad. Sci. U. S. A.* **1999,** *96* (24), 13611-13614.
54. Brust, M.; Walker, M.; Bethell, D.; Schiffrin, D. J.; Whyman, R., SYNTHESIS OF THIOL-DERIVATIZED GOLD NANOPARTICLES IN A 2-PHASE LIQUID-LIQUID SYSTEM. *Journal of the Chemical Society-Chemical Communications* **1994,** (7), 801-802.
55. Shahverdi, A. R.; Minaeian, S.; Shahverdi, H. R.; Jamalifar, H.; Nohi, A. A., Rapid synthesis of silver nanoparticles using culture supernatants of Enterobacteria: A novel biological approach. *Process Biochemistry* **2007,** *42* (5), 919-923.

56. Yu, Y. Y.; Chang, S. S.; Lee, C. L.; Wang, C. R. C., Gold nanorods: Electrochemical synthesis and optical properties. *Journal of Physical Chemistry B* **1997,** *101* (34), 6661-6664.
57. (a) Jana, N. R.; Gearheart, L.; Murphy, C. J., Seed-mediated growth approach for shape-controlled synthesis of spheroidal and rod-like gold nanoparticles using a surfactant template. *Adv. Mater.* **2001,** *13* (18), 1389-1393; (b) Nikoobakht, B.; El-Sayed, M. A., Preparation and growth mechanism of gold nanorods (NRs) using seed-mediated growth method. *Chemistry of Materials* **2003,** *15* (10), 1957-1962.
58. Murphy, C. J.; Gole, A. M.; Hunyadi, S. E.; Stone, J. W.; Sisco, P. N.; Alkilany, A.; Kinard, B. E.; Hankins, P., Chemical sensing and imaging with metallic nanorods. *Chemical Communications* **2008,** (5), 544-557.
59. Oldenburg, S. J.; Averitt, R. D.; Westcott, S. L.; Halas, N. J., Nanoengineering of optical resonances. *Chemical Physics Letters* **1998,** *288* (2-4), 243-247.
60. Wang, H.; Brandl, D. W.; Le, F.; Nordlander, P.; Halas, N. J., Nanorice: A hybrid plasmonic nanostructure. *Nano Lett.* **2006,** *6* (4), 827-832.
61. Chen, J. Y.; Wiley, B.; Li, Z. Y.; Campbell, D.; Saeki, F.; Cang, H.; Au, L.; Lee, J.; Li, X. D.; Xia, Y. N., Gold nanocages: Engineering their structure for biomedical applications. *Adv. Mater.* **2005,** *17* (18), 2255-2261.
62. (a) Thaxton, C. S.; Rosi, N. L.; Mirkin, C. A., Optically and chemically encoded nanoparticle materials for DNA and protein detection. *Mrs Bulletin* **2005,** *30* (5), 376-380; (b) Paciotti, G. F.; Myer, L.; Weinreich, D.; Goia, D.; Pavel, N.; McLaughlin, R. E.; Tamarkin, L., Colloidal gold: A novel nanoparticle vector for tumor directed drug delivery. *Drug Delivery* **2004,** *11* (3), 169-183; (c) Niidome, Y.; Honda, K.; Higashimoto, K.; Kawazumi, H.; Yamada, S.; Nakashima, N.; Sasaki, Y.; Ishida, Y.; Kikuchi, J., Surface modification of gold nanorods with synthetic cationic lipids. *Chemical Communications* **2007,** (36), 3777-3779; (d) Han, G.; Ghosh, P.; Rotello, V. M., Functionalized gold nanoparticles for drug delivery. *Nanomedicine* **2007,** *2* (1), 113-123; (e) Glomm, W. R., Functionalized gold nanoparticles for applications in bionanotechnology. *Journal of Dispersion Science and Technology* **2005,** *26* (3), 389-414.
63. Giersig, M.; Mulvaney, P., PREPARATION OF ORDERED COLLOID MONOLAYERS BY ELECTROPHORETIC DEPOSITION. *Langmuir* **1993,** *9* (12), 3408-3413.
64. Kolb, H. C.; Finn, M. G.; Sharpless, K. B., Click chemistry: Diverse chemical function from a few good reactions. *Angewandte Chemie-International Edition* **2001,** *40* (11), 2004-+.
65. Sperling, R. A.; Rivera gil, P.; Zhang, F.; Zanella, M.; Parak, W. J., Biological applications of gold nanoparticles. *Chem. Soc. Rev.* **2008,** *37* (9), 1896-1908.
66. Scott, R. W. J.; Wilson, O. M.; Crooks, R. M., Synthesis, characterization, and applications of dendrimer-encapsulated nanoparticles. *Journal of Physical Chemistry B* **2005,** *109* (2), 692-704.

67. Kumar, S.; Aaron, J.; Sokolov, K., Directional conjugation of antibodies to nanoparticles for synthesis of multiplexed optical contrast agents with both delivery and targeting moieties. *Nature Protocols* **2008,** *3* (2), 314-320.
68. Mie, G., Articles on the optical characteristics of turbid tubes, especially colloidal metal solutions. *Annalen Der Physik* **1908,** *25* (3), 377-445.
69. Kelly, K. L.; Coronado, E.; Zhao, L. L.; Schatz, G. C., The optical properties of metal nanoparticles: The influence of size, shape, and dielectric environment. *Journal of Physical Chemistry B* **2003,** *107* (3), 668-677.
70. (a) Sosa, I. O.; Noguez, C.; Barrera, R. G., Optical properties of metal nanoparticles with arbitrary shapes. *Journal of Physical Chemistry B* **2003,** *107* (26), 6269-6275; (b) Yang, W. H.; Schatz, G. C.; Vanduyne, R. P., DISCRETE DIPOLE APPROXIMATION FOR CALCULATING EXTINCTION AND RAMAN INTENSITIES FOR SMALL PARTICLES WITH ARBITRARY SHAPES. *Journal of Chemical Physics* **1995,** *103* (3), 869-875.
71. (a) Gray, S. K.; Kupka, T., Propagation of light in metallic nanowire arrays: Finite-difference time-domain studies of silver cylinders. *Physical Review B* **2003,** *68* (4); (b) Shlager, K. L.; Schneider, J. B., SELECTIVE SURVEY OF THE FINITE-DIFFERENCE TIME-DOMAIN LITERATURE. *Ieee Antennas and Propagation Magazine* **1995,** *37* (4), 39-57.
72. (a) Ghosh, S. K.; Nath, S.; Kundu, S.; Esumi, K.; Pal, T., Solvent and ligand effects on the localized surface plasmon resonance (LSPR) of gold colloids. *Journal of Physical Chemistry B* **2004,** *108* (37), 13963-13971; (b) Hutter, E.; Fendler, J. H., Exploitation of localized surface plasmon resonance. *Adv. Mater.* **2004,** *16* (19), 1685-1706.
73. Meier, M.; Wokaun, A., ENHANCED FIELDS ON LARGE METAL PARTICLES - DYNAMIC DEPOLARIZATION. *Optics Letters* **1983,** *8* (11), 581-583.
74. Wokaun, A.; Gordon, J. P.; Liao, P. F., RADIATION DAMPING IN SURFACE-ENHANCED RAMAN-SCATTERING. *Physical Review Letters* **1982,** *48* (14), 957-960.
75. (a) Hao, E.; Bailey, R. C.; Schatz, G. C.; Hupp, J. T.; Li, S. Y., Synthesis and optical properties of "branched" gold nanocrystals. *Nano Lett.* **2004,** *4* (2), 327-330; (b) Kottmann, J. P.; Martin, O. J. F.; Smith, D. R.; Schultz, S., Spectral response of plasmon resonant nanoparticles with a non-regular shape. *Optics Express* **2000,** *6* (11), 213-219.
76. Jain, P. K.; Lee, K. S.; El-Sayed, I. H.; El-Sayed, M. A., Calculated absorption and scattering properties of gold nanoparticles of different size, shape, and composition: Applications in biological imaging and biomedicine. *Journal of Physical Chemistry B* **2006,** *110* (14), 7238-7248.
77. Connor, E. E.; Mwamuka, J.; Gole, A.; Murphy, C. J.; Wyatt, M. D., Gold nanoparticles are taken up by human cells but do not cause acute cytotoxicity. *Small* **2005,** *1* (3), 325-327.
78. Niidome, T.; Yamagata, M.; Okamoto, Y.; Akiyama, Y.; Takahashi, H.; Kawano, T.; Katayama, Y.; Niidome, Y., PEG-modified gold nanorods with a stealth character for in vivo applications. *Journal of Controlled Release* **2006,** *114* (3), 343-347.

79. Takahashi, H.; Niidome, Y.; Niidome, T.; Kaneko, K.; Kawasaki, H.; Yamada, S., Modification of gold nanorods using phospatidylcholine to reduce cytotoxicity. *Langmuir* **2006,** *22* (1), 2-5.
80. Hauck, T. S.; Ghazani, A. A.; Chan, W. C. W., Assessing the effect of surface chemistry on gold nanorod uptake, toxicity, and gene expression in mammalian cells. *Small* **2008,** *4* (1), 153-159.
81. Moghimi, S. M.; Hunter, A. C.; Murray, J. C., Nanomedicine: current status and future prospects. *Faseb Journal* **2005,** *19* (3), 311-330.
82. Monfardini, C.; Veronese, F. M., Stabilization of substances in circulation. *Bioconjugate Chemistry* **1998,** *9* (4), 418-450.
83. (a) Florence, A. T., The oral absorption of micro- and nanoparticulates: Neither exceptional nor unusual. *Pharmaceutical Research* **1997,** *14* (3), 259-266; (b) Maincent, P.; Thouvenot, P.; Amicabile, C.; Hoffman, M.; Kreuter, J.; Couvreur, P.; Devissaguet, J. P., LYMPHATIC TARGETING OF POLYMERIC NANOPARTICLES AFTER INTRAPERITONEAL ADMINISTRATION IN RATS. *Pharmaceutical Research* **1992,** *9* (12), 1534-1539.
84. Zhang, G. D.; Yang, Z.; Lu, W.; Zhang, R.; Huang, Q.; Tian, M.; Li, L.; Liang, D.; Li, C., Influence of anchoring ligands and particle size on the colloidal stability and in vivo biodistribution of polyethylene glycol-coated gold nanoparticles in tumor-xenografted mice. *Biomaterials* **2009,** *30* (10), 1928-1936.
85. Hume, D. A.; Ross, I. L.; Himes, S. R.; Sasmono, R. T.; Wells, C. A.; Ravasi, T., The mononuclear phagocyte system revisited. *Journal of Leukocyte Biology* **2002,** *72* (4), 621-627.
86. Moghimi, S. M.; Patel, H. M., Serum-mediated recognition of liposomes by phagocytic cells of the reticuloendothelial system - The concept of tissue specificity. *Advanced Drug Delivery Reviews* **1998,** *32* (1-2), 45-60.
87. (a) Braet, F.; Dezanger, R.; Baekeland, M.; Crabbe, E.; Vandersmissen, P.; Wisse, E., STRUCTURE AND DYNAMICS OF THE FENESTRAE-ASSOCIATED CYTOSKELETON OF RAT-LIVER SINUSOIDAL ENDOTHELIAL-CELLS. *Hepatology* **1995,** *21* (1), 180-189; (b) Munn, L. L., Aberrant vascular architecture in tumors and its importance in drug-based therapies. *Drug Discovery Today* **2003,** *8* (9), 396-403.
88. (a) Ohara, Y.; Oda, T.; Yamada, K.; Hashimoto, S.; Akashi, Y.; Miyamoto, R.; Kobayashi, A.; Fukunaga, K.; Sasaki, R.; Ohkohchi, N., Effective delivery of chemotherapeutic nanoparticles by depleting host Kupffer cells. *International Journal of Cancer* **2012,** *131* (10), 2402-2410; (b) VanRooijen, N.; Sanders, A., Kupffer cell depletion by liposome-delivered drugs: Comparative activity of intracellular clodronate, propamidine, and ethylenediaminetetraacetic acid. *Hepatology* **1996,** *23* (5), 1239-1243.
89. Stolnik, S.; Illum, L.; Davis, S. S., LONG CIRCULATING MICROPARTICULATE DRUG CARRIERS. *Advanced Drug Delivery Reviews* **1995,** *16* (2-3), 195-214.
90. Moghimi, S. M.; Hunter, A. C., Poloxamers and poloxamines in nanoparticle engineering and experimental medicine. *Trends in Biotechnology* **2000,** *18* (10), 412-420.

91. Peracchia, M. T., Stealth nanoparticles for intravenous administration. *Stp Pharma Sciences* **2003,** *13* (3), 155-161.
92. Larson, T. A.; Joshi, P. P.; Sokolov, K., Preventing Protein Adsorption and Macrophage Uptake of Gold Nanoparticles via a Hydrophobic Shield. *ACS Nano* **2012,** *6* (Copyright (C) 2012 American Chemical Society (ACS). All Rights Reserved.), 9182-9190.
93. Sonavane, G.; Tomoda, K.; Makino, K., Biodistribution of colloidal gold nanoparticles after intravenous administration: Effect of particle size. *Colloids and Surfaces B-Biointerfaces* **2008,** *66* (2), 274-280.
94. De Jong, W. H.; Hagens, W. I.; Krystek, P.; Burger, M. C.; Sips, A.; Geertsma, R. E., Particle size-dependent organ distribution of gold nanoparticles after intravenous administration. *Biomaterials* **2008,** *29* (12), 1912-1919.
95. Moghimi, S. M., Modulation of lymphatic distribution of subcutaneously injected poloxamer 407-coated nanospheres: the effect of the ethylene oxide chain configuration (FEBS 27132) (vol 540, pg 241, 2003). *Febs Letters* **2003,** *545* (2-3), 260-260.
96. Perry, J. L.; Reuter, K. G.; Kai, M. P.; Herlihy, K. P.; Jones, S. W.; Luft, J. C.; Napier, M.; Bear, J. E.; DeSimone, J. M., PEGylated PRINT Nanoparticles: The Impact of PEG Density on Protein Binding, Macrophage Association, Biodistribution, and Pharmacokinetics. *Nano Lett.* **2012,** *12* (10), 5304-5310.
97. Peracchia, M. T.; Fattal, E.; Desmaele, D.; Besnard, M.; Noel, J. P.; Gomis, J. M.; Appel, M.; d'Angelo, J.; Couvreur, P., Stealth (R) PEGylated polycyanoacrylate nanoparticles for intravenous administration and splenic targeting. *Journal of Controlled Release* **1999,** *60* (1), 121-128.
98. Gratton, S. E. A.; PohhauS, P. D.; Lee, J.; Guo, I.; Cho, M. J.; DeSimone, J. M., Nanofabricated particles for engineered drug therapies: A preliminary Biodistribution study of PRINT (TM) nanoparticles. *Journal of Controlled Release* **2007,** *121* (1-2), 10-18.
99. Semmler-Behnke, M.; Kreyling, W. G.; Lipka, J.; Fertsch, S.; Wenk, A.; Takenaka, S.; Schmid, G.; Brandau, W., Biodistribution of 1.4-and 18-nm Gold Particles in Rats. *Small* **2008,** *4* (12), 2108-2111.
100. Qian, X. M.; Peng, X. H.; Ansari, D. O.; Yin-Goen, Q.; Chen, G. Z.; Shin, D. M.; Yang, L.; Young, A. N.; Wang, M. D.; Nie, S. M., In vivo tumor targeting and spectroscopic detection with surface-enhanced Raman nanoparticle tags. *Nat. Biotechnol.* **2008,** *26* (1), 83-90.
101. (a) Choi, C. H. J.; Alabi, C. A.; Webster, P.; Davis, M. E., Mechanism of active targeting in solid tumors with transferrin-containing gold nanoparticles. *Proc. Natl. Acad. Sci. U. S. A.* **2010,** *107* (3), 1235-1240; (b) Huang, X.; Peng, X.; Wang, Y.; Wang, Y.; Shin, D. M.; El-Sayed, M. A.; Nie, S., A Reexamination of Active and Passive Tumor Targeting by Using Rod-Shaped Gold Nanocrystals and Covalently Conjugated Peptide Ligands. *ACS Nano* **2010,** *4* (10), 5887-5896.
102. Hirsch, L. R.; Jackson, J. B.; Lee, A.; Halas, N. J.; West, J., A whole blood immunoassay using gold nanoshells. *Analytical Chemistry* **2003,** *75* (10), 2377-2381.

103. Mbindyo, J. K. N.; Reiss, B. D.; Martin, B. R.; Keating, C. D.; Natan, M. J.; Mallouk, T. E., DNA-directed assembly of gold nanowires on complementary surfaces. *Adv. Mater.* **2001,** *13* (4), 249-+.
104. Nam, J. M.; Thaxton, C. S.; Mirkin, C. A., Nanoparticle-based bio-bar codes for the ultrasensitive detection of proteins. *Science* **2003,** *301* (5641), 1884-1886.
105. Tang, S. X.; Hewlett, I., Nanoparticle-Based Immunoassays for Sensitive and Early Detection of HIV-1 Capsid (p24) Antigen. *Journal of Infectious Diseases* **2010,** *201*, S59-S64.
106. Mirkin, C. A.; Letsinger, R. L.; Mucic, R. C.; Storhoff, J. J., A DNA-based method for rationally assembling nanoparticles into macroscopic materials. *Nature* **1996,** *382* (6592), 607-609.
107. Leuvering, J. H. W.; Thal, P.; Waart, M. V. D.; Schuurs, A., SOL PARTICLE AGGLUTINATION IMMUNOASSAY FOR HUMAN CHORIONIC-GONADOTROPIN. *Fresenius Zeitschrift Fur Analytische Chemie* **1980,** *301* (2), 132-132.
108. Xu, X. Y.; Han, M. S.; Mirkin, C. A., A gold-nanoparticle-based real-time colorimetric screening method for endonuclease activity and inhibition. *Angewandte Chemie-International Edition* **2007,** *46* (19), 3468-3470.
109. Ray, P. C.; Darbha, G. K.; Ray, A.; Walker, J.; Hardy, W., Gold nanoparticle based FRET for DNA detection. *Plasmonics* **2007,** *2* (4), 173-183.
110. Lee, S.; Cha, E. J.; Park, K.; Lee, S. Y.; Hong, J. K.; Sun, I. C.; Kim, S. Y.; Choi, K.; Kwon, I. C.; Kim, K.; Ahn, C. H., A near-infrared-fluorescence-quenched gold-nanoparticle imaging probe for in vivo drug screening and protease activity determination. *Angewandte Chemie-International Edition* **2008,** *47* (15), 2804-2807.
111. Debouttiere, P. J.; Roux, S.; Vocanson, F.; Billotey, C.; Beuf, O.; Favre-Reguillon, A.; Lin, Y.; Pellet-Rostaing, S.; Lamartine, R.; Perriat, P.; Tillement, O., Design of gold nanoparticles for magnetic resonance imaging. *Advanced Functional Materials* **2006,** *16* (18), 2330-2339.
112. (a) Ji, X. J.; Shao, R. P.; Elliott, A. M.; Stafford, R. J.; Esparza-Coss, E.; Bankson, J. A.; Liang, G.; Luo, Z. P.; Park, K.; Markert, J. T.; Li, C., Bifunctional gold nanoshells with a superparamagnetic iron oxide-silica core suitable for both MR imaging and photothermal therapy. *Journal of Physical Chemistry C* **2007,** *111* (17), 6245-6251; (b) Larson, T. A.; Bankson, J.; Aaron, J.; Sokolov, K., Hybrid plasmonic magnetic nanoparticles as molecular specific agents for MRI/optical imaging and photothermal therapy of cancer cells. *Nanotechnology* **2007,** *18* (32); (c) Lim, Y. T.; Cho, M. Y.; Kim, J. K.; Hwangbo, S.; Chung, B. H., Plasmonic magnetic nanostructure for bimodal imaging and photonic-based therapy of cancer cells. *Chembiochem* **2007,** *8* (18), 2204-2209; (d) Ma, L. L.; Feldman, M. D.; Tam, J. M.; Paranjape, A. S.; Cheruku, K. K.; Larson, T. A.; Tam, J. O.; Ingram, D. R.; Paramita, V.; Villard, J. W.; Jenkins, J. T.; Wang, T.; Clarke, G. D.; Asmis, R.; Sokolov, K.; Chandrasekar, B.; Milner, T. E.; Johnston, K. P., Small Multifunctional Nanoclusters (Nanoroses) for Targeted Cellular Imaging and Therapy. *ACS Nano* **2009,** *3* (9), 2686-2696.

113. Huang, X. H.; El-Sayed, I. H.; Qian, W.; El-Sayed, M. A., Cancer cells assemble and align gold nanorods conjugated to antibodies to produce highly enhanced, sharp, and polarized surface Raman spectra: A potential cancer diagnostic marker. *Nano Lett.* **2007,** *7* (6), 1591-1597.
114. Bishnoi, S. W.; Rozell, C. J.; Levin, C. S.; Gheith, M. K.; Johnson, B. R.; Johnson, D. H.; Halas, N. J., All-optical nanoscale pH meter. *Nano Lett.* **2006,** *6* (8), 1687-1692.
115. Mallidi, S.; Larson, T.; Tam, J.; Joshi, P. P.; Karpiouk, A.; Sokolov, K.; Emelianov, S., Multiwavelength Photoacoustic Imaging and Plasmon Resonance Coupling of Gold Nanoparticles for Selective Detection of Cancer. *Nano Lett.* **2009,** *9* (8), 2825-2831.
116. Wang, B.; Yantsen, E.; Larson, T.; Karpiouk, A. B.; Sethuraman, S.; Su, J. L.; Sokolov, K.; Emelianov, S. Y., Plasmonic Intravascular Photoacoustic Imaging for Detection of Macrophages in Atherosclerotic Plaques. *Nano Lett.* **2009,** *9* (6), 2212-2217.
117. Yang, X. M.; Skrabalak, S. E.; Li, Z. Y.; Xia, Y. N.; Wang, L. H. V., Photoacoustic tomography of a rat cerebral cortex in vivo with au nanocages as an optical contrast agent. *Nano Lett.* **2007,** *7* (12), 3798-3802.
118. Pan, D. P. J.; Pramanik, M.; Senpan, A.; Ghosh, S.; Wickline, S. A.; Wang, L. V.; Lanza, G. M., Near infrared photoacoustic detection of sentinel lymph nodes with gold nanobeacons. *Biomaterials* **2010,** *31* (14), 4088-4093.
119. Jokerst, J. V.; Thangaraj, M.; Kempen, P. J.; Sinclair, R.; Gambhir, S. S., Photoacoustic Imaging of Mesenchymal Stem Cells in Living Mice via Silica-Coated Gold Nanorods. *ACS Nano* **2012,** *6* (7), 5920-5930.
120. Durr, N. J.; Larson, T.; Smith, D. K.; Korgel, B. A.; Sokolov, K.; Ben-Yakar, A., Two-photon luminescence imaging of cancer cells using molecularly targeted gold nanorods. *Nano Lett.* **2007,** *7* (4), 941-945.
121. Wang, T. Y.; Mancuso, J. J.; Sapozhnikova, V.; Dwelle, J.; Ma, L. L.; Willsey, B.; Kazmi, S. M. S.; Qiu, J. Z.; Li, X. K.; Asmis, R.; Johnston, K. P.; Feldman, M. D.; Milner, T. E., Dual-wavelength multifrequency photothermal wave imaging combined with optical coherence tomography for macrophage and lipid detection in atherosclerotic plaques using gold nanoparticles. *Journal of Biomedical Optics* **2012,** *17* (3).
122. Tanaka, R.; Yuhi, T.; Nagatani, N.; Endo, T.; Kerman, K.; Takamura, Y.; Tamiya, E., A novel enhancement assay for immunochromatographic test strips using gold nanoparticles. *Analytical and Bioanalytical Chemistry* **2006,** *385* (8), 1414-1420.
123. Doria, G.; Franco, R.; Baptista, P., Nanodiagnostics: fast colorimetric method for single nucleotide polymorphism/mutation detection. *Iet Nanobiotechnology* **2007,** *1* (4), 53-57.
124. Aaron, J.; Nitin, N.; Travis, K.; Kumar, S.; Collier, T.; Park, S. Y.; Jose-Yacaman, M.; Coghlan, L.; Follen, M.; Richards-Kortum, R.; Sokolov, K., Plasmon resonance coupling of metal nanoparticles for molecular imaging of carcinogenesis in vivo. *Journal of Biomedical Optics* **2007,** *12* (3).

125. Haes, A. J.; Hall, W. P.; Chang, L.; Klein, W. L.; Van Duyne, R. P., A localized surface plasmon resonance biosensor: First steps toward an assay for Alzheimer's disease. *Nano Lett.* **2004,** *4* (6), 1029-1034.
126. Bowman, M. C.; Ballard, T. E.; Ackerson, C. J.; Feldheim, D. L.; Margolis, D. M.; Melander, C., Inhibition of HIV fusion with multivalent gold nanoparticles. *Journal of the American Chemical Society* **2008,** *130* (22), 6896-+.
127. (a) El-Sayed, I. H.; Huang, X. H.; El-Sayed, M. A., Selective laser photo-thermal therapy of epithelial carcinoma using anti-EGFR antibody conjugated gold nanoparticles. *Cancer Letters* **2006,** *239* (1), 129-135; (b) Hirsch, L. R.; Stafford, R. J.; Bankson, J. A.; Sershen, S. R.; Rivera, B.; Price, R. E.; Hazle, J. D.; Halas, N. J.; West, J. L., Nanoshell-mediated near-infrared thermal therapy of tumors under magnetic resonance guidance. *Proc. Natl. Acad. Sci. U. S. A.* **2003,** *100* (23), 13549-13554; (c) Huang, X. H.; Jain, P. K.; El-Sayed, I. H.; El-Sayed, M. A., Determination of the minimum temperature required for selective photothermal destruction of cancer cells with the use of immunotargeted gold nanoparticles. *Photochemistry and Photobiology* **2006,** *82* (2), 412-417; (d) Loo, C.; Lowery, A.; Halas, N. J.; West, J.; Drezek, R., Immunotargeted nanoshells for integrated cancer imaging and therapy. *Nano Lett.* **2005,** *5* (4), 709-711; (e) O'Neal, D. P.; Hirsch, L. R.; Halas, N. J.; Payne, J. D.; West, J. L., Photo-thermal tumor ablation in mice using near infrared-absorbing nanoparticles. *Cancer Letters* **2004,** *209* (2), 171-176.
128. Zharov, V. P.; Galitovskaya, E. N.; Johnson, C.; Kelly, T., Synergistic enhancement of selective nanophotothermolysis with gold nanoclusters: Potential for cancer therapy. *Lasers in Surgery and Medicine* **2005,** *37* (3), 219-226.
129. Stern, J. M.; Stanfield, J.; Kabbani, W.; Hsieh, J. T.; Cadeddu, J. R. A., Selective prostate cancer thermal ablation with laser activated gold nanoshells. *Journal of Urology* **2008,** *179* (2), 748-753.
130. Hu, K. W.; Huang, C. C.; Hwu, J. R.; Su, W. C.; Shieh, D. B.; Yeh, C. S., A new photothermal therapeutic agent: Core-free nanostructured AuxAg1-x dendrites. *Chemistry-a European Journal* **2008,** *14* (10), 2956-2964.
131. Cheng, Y.; Samia, A. C.; Meyers, J. D.; Panagopoulos, I.; Fei, B. W.; Burda, C., Highly efficient drug delivery with gold nanoparticle vectors for in vivo photodynamic therapy of cancer. *Journal of the American Chemical Society* **2008,** *130* (32), 10643-10647.
132. Visaria, R. K.; Griffin, R. J.; Williams, B. W.; Ebbini, E. S.; Paciotti, G. F.; Song, C. W.; Bischof, J. C., Enhancement of tumor thermal therapy using gold nanoparticle-assisted tumor necrosis factor-alpha delivery. *Molecular Cancer Therapeutics* **2006,** *5* (4), 1014-1020.
133. Bhattacharya, R.; Mukherjee, P., Biological properties of "naked" metal nanoparticles. *Advanced Drug Delivery Reviews* **2008,** *60* (11), 1289-1306.
134. Chamberland, D. L.; Agarwal, A.; Kotov, N.; Fowlkes, J. B.; Carson, P. L.; Wang, X., Photoacoustic tomography of joints aided by an Etanercept-conjugated gold nanoparticle contrast agent - an ex vivo preliminary rat study. *Nanotechnology* **2008,** *19* (9).

135. Sisco, P. N.; Wilson, C. G.; Mironova, E.; Baxter, S. C.; Murphy, C. J.; Goldsmith, E. C., The Effect of Gold Nanorods on Cell-Mediated Collagen Remodeling. *Nano Lett.* **2008,** *8* (10), 3409-3412.
136. Thomas, M.; Klibanov, A. M., Conjugation to gold nanoparticles enhances polyethylenimine's transfer of plasmid DNA into mammalian cells. *Proc. Natl. Acad. Sci. U. S. A.* **2003,** *100* (16), 9138-9143.
137. Rosi, N. L.; Giljohann, D. A.; Thaxton, C. S.; Lytton-Jean, A. K. R.; Han, M. S.; Mirkin, C. A., Oligonucleotide-modified gold nanoparticles for intracellular gene regulation. *Science* **2006,** *312* (5776), 1027-1030.
138. Cardinal, J.; Klune, J. R.; Chory, E.; Jeyabalan, G.; Kanzius, J. S.; Nalesnik, M.; Geller, D. A., Noninvasive radiofrequency ablation of cancer targeted by gold nanoparticles. *Surgery* **2008,** *144* (2), 125-132.
139. Diagaradjane, P.; Shetty, A.; Wang, J. C.; Elliott, A. M.; Schwartz, J.; Shentu, S.; Park, H. C.; Deorukhkar, A.; Stafford, R. J.; Cho, S. H.; Tunnell, J. W.; Hazle, J. D.; Krishnan, S., Modulation of in vivo tumor radiation response via gold nanoshell-mediated vascular-focused hyperthermia: Characterizing an integrated antihypoxic and localized vascular disrupting targeting strategy. *Nano Lett.* **2008,** *8* (5), 1492-1500.
140. Jennings, L. E.; Long, N. J., 'Two is better than one'-probes for dual-modality molecular imaging. *Chemical Communications* **2009,** (24), 3511-3524.
141. Vuu, K.; Xie, J. W.; McDonald, M. A.; Bernardo, M.; Hunter, F.; Zhang, Y. T.; Li, K.; Bednarski, M.; Guccione, S., Gadolinium-rhodamine nanoparticles for cell labeling and tracking via magnetic resonance and optical imaging. *Bioconjugate Chemistry* **2005,** *16* (4), 995-999.
142. Tomalia, D. A.; Reyna, L. A.; Svenson, S., Dendrimers as multi-purpose nanodevices for oncology drug delivery and diagnostic imaging. *Biochemical Society Transactions* **2007,** *35*, 61-67.
143. Gerion, D.; Herberg, J.; Bok, R.; Gjersing, E.; Ramon, E.; Maxwell, R.; Kurhanewicz, J.; Budinger, T. F.; Gray, J. W.; Shuman, M. A.; Chen, F. F., Paramagnetic silica-coated nanocrystals as an advanced MRI contrast agent. *Journal of Physical Chemistry C* **2007,** *111* (34), 12542-12551.
144. Rieter, W. J.; Kim, J. S.; Taylor, K. M. L.; An, H.; Lin, W.; Tarrant, T.; Lin, W., Hybrid silica nanoparticles for multimodal Imaging. *Angewandte Chemie-International Edition* **2007,** *46* (20), 3680-3682.
145. Kircher, M. F.; de la Zerda, A.; Jokerst, J. V.; Zavaleta, C. L.; Kempen, P. J.; Mittra, E.; Pitter, K.; Huang, R.; Campos, C.; Habte, F.; Sinclair, R.; Brennan, C. W.; Mellinghoff, I. K.; Holland, E. C.; Gambhir, S. S., A brain tumor molecular imaging strategy using a new triple-modality MRI-photoacoustic-Raman nanoparticle. *Nature Medicine* **2012,** *18* (5), 829-U235.
146. Shashkov, E. V.; Everts, M.; Galanzha, E. I.; Zharov, V. P., Quantum Dots as Multimodal Photoacoustic and Photothermal Contrast Agents. *Nano Lett.* **2008,** *8* (11), 3953-3958.

147. Mulder, W. J. M.; Koole, R.; Brandwijk, R. J.; Storm, G.; Chin, P. T. K.; Strijkers, G. J.; Donega, C. D.; Nicolay, K.; Griffioen, A. W., Quantum dots with a paramagnetic coating as a bimodal molecular imaging probe. *Nano Lett.* **2006,** *6* (1), 1-6.
148. Koole, R.; van Schooneveld, M. M.; Hilhorst, J.; Castermans, K.; Cormode, D. P.; Strijkers, G. J.; Donega, C. d. M.; Vanmaekelbergh, D.; Griffioen, A. W.; Nicolay, K.; Fayad, Z. A.; Meijerink, A.; Mulder, W. J. M., Paramagnetic Lipid-Coated Silica Nanoparticles with a Fluorescent Quantum Dot Core: A New Contrast Agent Platform for Multimodality Imaging. *Bioconjugate Chemistry* **2008,** *19* (12), 2471-2479.
149. Tu, C.; Ma, X.; Pantazis, P.; Kauzlarich, S. M.; Louie, A. Y., Paramagnetic, Silicon Quantum Dots for Magnetic Resonance and Two-Photon Imaging of Macrophages. *Journal of the American Chemical Society* **2010,** *132* (6), 2016-2023.
150. Marckmann, P.; Skov, L.; Rossen, K.; Dupont, A.; Damholt, M. B.; Heaf, J. G.; Thomsen, H. S., Nephrogenic systemic fibrosis: Suspected causative role of gadodiamide used for contrast-enhanced magnetic resonance imaging. *Journal of the American Society of Nephrology* **2006,** *17* (9), 2359-2362.
151. Josephson, L.; Kircher, M. F.; Mahmood, U.; Tang, Y.; Weissleder, R., Near-infrared fluorescent nanoparticles as combined MR/optical imaging probes. *Bioconjugate Chemistry* **2002,** *13* (3), 554-560.
152. (a) Kircher, M. F.; Allport, J. R.; Graves, E. E.; Love, V.; Josephson, L.; Lichtman, A. H.; Weissleder, R., In vivo high resolution three-dimensional imaging of antigen-specific cytotoxic T-lymphocyte trafficking to tumors. *Cancer Research* **2003,** *63* (20), 6838-6846; (b) Xie, J.; Chen, K.; Huang, J.; Lee, S.; Wang, J. H.; Gao, J.; Li, X. G.; Chen, X. Y., PET/NIRF/MRI triple functional iron oxide nanoparticles. *Biomaterials* **2010,** *31* (11), 3016-3022.
153. Xu, C.; Xie, J.; Ho, D.; Wang, C.; Kohler, N.; Walsh, E. G.; Morgan, J. R.; Chin, Y. E.; Sun, S., Au-Fe3O4 dumbbell nanoparticles as dual-functional probes. *Angewandte Chemie-International Edition* **2008,** *47* (1), 173-176.
154. Swierczewska, M.; Lee, S.; Chen, X., Inorganic Nanoparticles for Multimodal Molecular Imaging. *Molecular Imaging* **2011,** *10* (1), 3-16.
155. Mallidi, S.; Larson, T.; Aaron, J.; Sokolov, K.; Emelianov, S., Molecular specific optoacoustic imaging with plasmonic nanoparticles. *Optics Express* **2007,** *15* (11), 6583-6588.
156. Kim, J.-W.; Galanzha, E. I.; Shashkov, E. V.; Moon, H.-M.; Zharov, V. P., Golden carbon nanotubes as multimodal photoacoustic and photothermal high-contrast molecular agents. *Nature Nanotechnology* **2009,** *4* (10), 688-694.
157. Galanzha, E. I.; Shashkov, E. V.; Kelly, T.; Kim, J.-W.; Yang, L.; Zharov, V. P., In vivo magnetic enrichment and multiplex photoacoustic detection of circulating tumour cells. *Nature Nanotechnology* **2009,** *4* (12), 855-860.
158. Lee, J.-H.; Huh, Y.-M.; Jun, Y.-w.; Seo, J.-w.; Jang, J.-t.; Song, H.-T.; Kim, S.; Cho, E.-J.; Yoon, H.-G.; Suh, J.-S.; Cheon, J., Artificially engineered magnetic nanoparticles for ultra-sensitive molecular imaging. *Nature Medicine* **2007,** *13* (1), 95-99.
159. Lijowski, M.; Caruthers, S.; Hu, G.; Zhang, H.; Scott, M. J.; Williams, T.; Erpelding, T.; Schmieder, A. H.; Kiefer, G.; Gulyas, G.; Athey, P. S.; Gaffney, P. J.;

Wickline, S. A.; Lanza, G. M., High Sensitivity High-Resolution SPECT-CT/MR Molecular Imaging of Angiogenesis in the Vx2 Model. *Investigative Radiology* **2009,** *44* (1), 15-22.
160. (a) Raylman, R. R.; Majewski, S.; Sendhil Velan, S.; Lemieux, S.; Kross, B.; Popov, V.; Smith, M. F.; Weisenberger, A. G., Simultaneous acquisition of magnetic resonance spectroscopy (MRS) data and positron emission tomography (PET) images with a prototype MR-compatible, small animal PET imager. *Journal of Magnetic Resonance* **2007,** *186* (2), 305-310; (b) Raylman, R. R.; Majewski, S.; Lemieux, S.; Velan, S. S.; Kross, B.; Popov, V.; Smith, M. F.; Weisenberger, A. G.; Wojcik, R., Initial tests of a prototype MRI-compatible PET imager. *Nuclear Instruments & Methods in Physics Research Section a-Accelerators Spectrometers Detectors and Associated Equipment* **2006,** *569* (2), 306-309.
161. Choi, J.-s.; Park, J. C.; Nah, H.; Woo, S.; Oh, J.; Kim, K. M.; Cheon, G. J.; Chang, Y.; Yoo, J.; Cheon, J., A hybrid nanoparticle probe for dual-modality positron emission tomography and magnetic resonance imaging. *Angewandte Chemie-International Edition* **2008,** *47* (33), 6259-6262.
162. Lewin, M.; Carlesso, N.; Tung, C. H.; Tang, X. W.; Cory, D.; Scadden, D. T.; Weissleder, R., Tat peptide-derivatized magnetic nanoparticles allow in vivo tracking and recovery of progenitor cells. *Nat. Biotechnol.* **2000,** *18* (4), 410-414.
163. Csortos, C.; Kolosova, I.; Verin, A. D., Regulation of vascular endothelial cell barrier function and cytoskeleton structure by protein phosphatases of the PPP family. *American Journal of Physiology-Lung Cellular and Molecular Physiology* **2007,** *293* (4), L843-L854.
164. Choi, H. S.; Liu, W.; Misra, P.; Tanaka, E.; Zimmer, J. P.; Ipe, B. I.; Bawendi, M. G.; Frangioni, J. V., Renal clearance of quantum dots. *Nat. Biotechnol.* **2007,** *25* (10), 1165-1170.
165. Barrett, T.; Choyke, P. L.; Kobayashi, H., Imaging of the lymphatic system: new horizons. *Contrast Media & Molecular Imaging* **2006,** *1* (6), 230-245.
166. Hamidi, M.; Azadi, A.; Rafiei, P., Pharmacokinetic consequences of pegylation. *Drug Delivery* **2006,** *13* (6), 399-409.
167. Ohlson, M.; Sorensson, J.; Haraldsson, B., A gel-membrane model of glomerular charge and size selectivity in series. *American Journal of Physiology-Renal Physiology* **2001,** *280* (3), F396-F405.
168. Prescott, L. F.; McAuslane, J. A. N.; Freestone, S., THE CONCENTRATION-DEPENDENT DISPOSITION AND KINETICS OF INULIN. *European Journal of Clinical Pharmacology* **1991,** *40* (6), 619-624.
169. Chapman, A. P.; Antoniw, P.; Spitali, M.; West, S.; Stephens, S.; King, D. J., Therapeutic antibody fragments with prolonged in vivo half-lives. *Nat. Biotechnol.* **1999,** *17* (8), 780-783.
170. (a) Kobayashi, H.; Brechbiel, M. W., Nano-sized MRI contrast agents with dendrimer cores. *Advanced Drug Delivery Reviews* **2005,** *57* (15), 2271-2286; (b) Kobayashi, H.; Le, N.; Kim, I. S.; Kim, M. G.; Pie, J. E.; Drumm, D.; Paik, D. S.; Waldmann, T. A.; Paik, C. H.; Carrasquillo, J. A., The pharmacokinetic characteristics of

glycolated humanized anti-Tac Fabs are determined by their isoelectric points. *Cancer Research* **1999,** *59* (2), 422-430.
171. Wintrobe, Wintrobe's Clinical Hematology. **2009,** *1*, 255.
172. (a) Kobayashi, H.; Wu, C. C.; Kim, M. K.; Paik, C. H.; Carrasquillo, J. A.; Brechbiel, M. W., Evaluation of the in vivo biodistribution of indium-111 and yttrium-88 labeled dendrimer-1B4M-DTPA and its conjugation with anti-Tac monoclonal antibody. *Bioconjugate Chemistry* **1999,** *10* (1), 103-111; (b) Wiener, E. C.; Brechbiel, M. W.; Brothers, H.; Magin, R. L.; Gansow, O. A.; Tomalia, D. A.; Lauterbur, P. C., DENDRIMER-BASED METAL-CHELATES - A NEW CLASS OF MAGNETIC-RESONANCE-IMAGING CONTRAST AGENTS. *Magn.Reson.Med.* **1994,** *31* (1), 1-8.
173. (a) Kobayashi, H.; Jo, S. K.; Kawamoto, S.; Yasuda, H.; Hu, X. Z.; Knopp, M. V.; Brechbiel, M. W.; Choyke, P. L.; Star, R. A., Polyamine dendrimer-based MRI contrast agents for functional kidney imaging to diagnose acute renal failure. *Journal of Magnetic Resonance Imaging* **2004,** *20* (3), 512-518; (b) Sato, N.; Kobayashi, H.; Hiraga, A.; Saga, T.; Togashi, K.; Konishi, J.; Brechbiel, M. W., Pharmacokinetics and enhancement patterns of macromolecular MR contrast agents with various sizes of polyamidoamine dendrimer cores. *Magn.Reson.Med.* **2001,** *46* (6), 1169-1173.
174. Kobayashi, H.; Kawamoto, S.; Jo, S. K.; Bryant, H. L.; Brechbiel, M. W.; Star, R. A., Macromolecular MRI contrast agents with small dendrimers: Pharmacokinetic differences between sizes and cores. *Bioconjugate Chemistry* **2003,** *14* (2), 388-394.
175. Feng, Y.; Zong, Y. D.; Ke, T. Y.; Jeong, E. K.; Parker, D. L.; Lu, Z. R., Pharmacokinetics, biodistribution and contrast enhanced MR blood pool imaging of Gd-DTPA cystine copolymers and Gd-DTPA cystine diethyl ester copolymers in a rat model. *Pharmaceutical Research* **2006,** *23* (8), 1736-1742.
176. Zong, Y. D.; Wang, X. H.; Goodrich, K. C.; Mohs, A. M.; Parker, D. L.; Lu, Z. R., Contrast-enhanced MRI with new biodegradable macromolecular Gd(III) complexes in tumor-bearing mice. *Magn.Reson.Med.* **2005,** *53* (4), 835-842.
177. Fischer, H. C.; Liu, L. C.; Pang, K. S.; Chan, W. C. W., Pharmacokinetics of nanoscale quantum dots: In vivo distribution, sequestration, and clearance in the rat. *Advanced Functional Materials* **2006,** *16* (10), 1299-1305.
178. Cherukuri, P.; Gannon, C. J.; Leeuw, T. K.; Schmidt, H. K.; Smalley, R. E.; Curley, S. A.; Weisman, R. B., Mammalian pharmacokinetics of carbon nanotubes using intrinsic near-infrared fluorescence. *Proc. Natl. Acad. Sci. U. S. A.* **2006,** *103* (50), 18882-18886.
179. Singh, R.; Pantarotto, D.; Lacerda, L.; Pastorin, G.; Klumpp, C.; Prato, M.; Bianco, A.; Kostarelos, K., Tissue biodistribution and blood clearance rates of intravenously administered carbon nanotube radiotracers. *Proc. Natl. Acad. Sci. U. S. A.* **2006,** *103* (9), 3357-3362.
180. (a) Chonn, A.; Cullis, P. R.; Devine, D. V., THE ROLE OF SURFACE-CHARGE IN THE ACTIVATION OF THE CLASSICAL AND ALTERNATIVE PATHWAYS OF COMPLEMENT BY LIPOSOMES. *Journal of Immunology* **1991,** *146* (12), 4234-4241; (b) Ishida, T.; Harashima, H.; Kiwada, H., Liposome clearance. *Bioscience Reports* **2002,** *22* (2), 197-224.

181. Funato, K.; Yoda, R.; Kiwada, H., CONTRIBUTION OF COMPLEMENT-SYSTEM ON DESTABILIZATION OF LIPOSOMES COMPOSED OF HYDROGENATED EGG PHOSPHATIDYLCHOLINE IN RAT FRESH PLASMA. *Biochimica Et Biophysica Acta* **1992,** *1103* (2), 198-204.
182. Zheng, J. Z.; Liu, J. B.; Dunne, M.; Jaffray, D. A.; Allen, C., In vivo performance of a liposomal vascular contrast agent for CT and MR-based image guidance applications. *Pharmaceutical Research* **2007,** *24* (6), 1193-1201.
183. Hainfeld, J. F.; Slatkin, D. N.; Focella, T. M.; Smilowitz, H. M., Gold nanoparticles: a new X-ray contrast agent. *British Journal of Radiology* **2006,** *79* (939), 248-253.
184. Balogh, L.; Nigavekar, S. S.; Nair, B. M.; Lesniak, W.; Zhang, C.; Sung, L. Y.; Kariapper, M. S. T.; El-Jawahri, A.; Llanes, M.; Bolton, B.; Mamou, F.; Tan, W.; Hutson, A.; Minc, L.; Khan, M. K., Significant effect of size on the in vivo biodistribution of gold composite nanodevices in mouse tumor models. *Nanomed.-Nanotechnol. Biol. Med.* **2007,** *3* (4), 281-296.
185. Zhou, C.; Long, M.; Qin, Y. P.; Sun, X. K.; Zheng, J., Luminescent Gold Nanoparticles with Efficient Renal Clearance. *Angewandte Chemie-International Edition* **2011,** *50* (14), 3168-3172.
186. Corot, C.; Robert, P.; Idee, J.-M.; Port, M., Recent advances in iron oxide nanocrystal technology for medical imaging. *Advanced Drug Delivery Reviews* **2006,** *58* (14), 1471-1504.
187. Jain, T. K.; Reddy, M. K.; Morales, M. A.; Leslie-Pelecky, D. L.; Labhasetwar, V., Biodistribution, clearance, and biocompatibility of iron oxide magnetic nanoparticles in rats. *Molecular Pharmaceutics* **2008,** *5* (2), 316-327.
188. Bourrinet, P.; Bengele, H. H.; Bonnemain, B.; Dencausse, A.; Idee, J. M.; Jacobs, P. M.; Lewis, J. M., Preclinical safety and pharmacokinetic profile of ferumoxtran-10, an ultrasmall superparamagnetic iron oxide magnetic resonance contrast agent. *Investigative Radiology* **2006,** *41* (3), 313-324.
189. (a) Popplewell, J. F.; King, S. J.; Day, J. P.; Ackrill, P.; Fifield, L. K.; Cresswell, R. G.; Di Tada, M. L.; Liu, K., Kinetics of uptake and elimination of silicic acid by a human subject: A novel application of Si-32 and accelerator mass spectrometry. *Journal of Inorganic Biochemistry* **1998,** *69* (3), 177-180; (b) Park, J. H.; Gu, L.; von Maltzahn, G.; Ruoslahti, E.; Bhatia, S. N.; Sailor, M. J., Biodegradable luminescent porous silicon nanoparticles for in vivo applications. *Nature Materials* **2009,** *8* (4), 331-336.
190. Veale, D.; Kerr, N.; Gibson, G. J.; Harris, A. L., CHARACTERIZATION OF EPIDERMAL GROWTH-FACTOR RECEPTOR IN PRIMARY HUMAN NON-SMALL CELL LUNG-CANCER. *Cancer Research* **1989,** *49* (5), 1313-1317.
191. (a) Pao, W.; Miller, V. A., Epidermal growth factor receptor mutations, small-molecule kinase inhibitors, and non-small-cell lung cancer: Current knowledge and future directions. *Journal of Clinical Oncology* **2005,** *23* (11), 2556-2568; (b) Cappuzzo, F.; Hirsch, F. R.; Rossi, E.; Bartolini, S.; Ceresoli, G. L.; Bemis, L.; Haney, J.; Witta, S.; Danenberg, K.; Domenichini, I.; Ludovini, V.; Magrini, E.; Gregorc, V.; Doglioni, C.; Sidoni, A.; Tonato, M.; Franklin, W. A.; Crino, L.; Bunn, P. A.; Varella-Garcia, M.,

Epidermal growth factor receptor gene and protein and gefitinib sensitivity in non-small-cell lung cancer. *Journal of the National Cancer Institute* **2005,** *97* (9), 643-655; (c) Baker, C. H.; Kedar, D.; McCarty, M. F.; Tsan, R.; Weber, K. L.; Bucana, C. D.; Fidler, I. J., Blockade of epidermal growth factor receptor signaling on tumor cells and tumor-associated endothelial cells for therapy of human carcinomas. *American Journal of Pathology* **2002,** *161* (3), 929-938.
192. Yokoyama, T.; Tam, J.; Kuroda, S.; Scott, A. W.; Aaron, J.; Larson, T.; Shanker, M.; Correa, A. M.; Kondo, S.; Roth, J. A.; Sokolov, K.; Ramesh, R., EGFR-Targeted Hybrid Plasmonic Magnetic Nanoparticles Synergistically Induce Autophagy and Apoptosis in Non-Small Cell Lung Cancer Cells. *Plos One* **2011,** *6* (11).
193. Huang, X. H.; El-Sayed, I. H.; Qian, W.; El-Sayed, M. A., Cancer cell imaging and photothermal therapy in the near-infrared region by using gold nanorods. *Journal of the American Chemical Society* **2006,** *128* (6), 2115-2120.
194. (a) Vermorken, J. B.; Mesia, R.; Rivera, F.; Remenar, E.; Kawecki, A.; Rottey, S.; Erfan, J.; Zabolotnyy, D.; Kienzer, H. R.; Cupissol, D.; Peyrade, F.; Benasso, M.; Vynnychenko, I.; De Raucourt, D.; Bokemeyer, C.; Schueler, A.; Amellal, N.; Hitt, R., Platinum-based chemotherapy plus cetuximab in head and neck cancer. *N. Engl. J. Med.* **2008,** *359* (11), 1116-1127; (b) Cunningham, D.; Humblet, Y.; Siena, S.; Khayat, D.; Bleiberg, H.; Santoro, A.; Bets, D.; Mueser, M.; Harstrick, A.; Verslype, C.; Chau, I.; Van Cutsem, E., Cetuximab monotherapy and cetuximab plus irinotecan in irinotecan-refractory metastatic colorectal cancer. *N. Engl. J. Med.* **2004,** *351* (4), 337-345; (c) Bonner, J. A.; Harari, P. M.; Giralt, J.; Cohen, R. B.; Jones, C. U.; Sur, R. K.; Raben, D.; Baselga, J.; Spencer, S. A.; Zhu, J. M.; Youssoufian, H.; Rowinsky, E. K.; Ang, K. K., Radiotherapy plus cetuximab for locoregionally advanced head and neck cancer: 5-year survival data from a phase 3 randomised trial, and relation between cetuximab-induced rash and survival. *Lancet Oncology* **2010,** *11* (1), 21-28.
195. (a) Aaron, J.; Travis, K.; Harrison, N.; Sokolov, K., Dynamic Imaging of Molecular Assemblies in Live Cells Based on Nanoparticle Plasmon Resonance Coupling. *Nano Lett.* **2009,** *9* (10), 3612-3618; (b) Kumar, S.; Harrison, N.; Richards-Kortum, R.; Sokolov, K., Plasmonic nanosensors for imaging intracellular biomarkers in live cells. *Nano Lett.* **2007,** *7* (5), 1338-1343.
196. Crothers, D. M.; Metzger, H., INFLUENCE OF POLYVALENCY ON BINDING PROPERTIES OF ANTIBODIES. *Immunochemistry* **1972,** *9* (3), 341-&.
197. Pluckthun, A.; Pack, P., New protein engineering approaches to multivalent and bispecific antibody fragments. *Immunotechnology* **1997,** *3* (2), 83-105.
198. Kitov, P. I.; Sadowska, J. M.; Mulvey, G.; Armstrong, G. D.; Ling, H.; Pannu, N. S.; Read, R. J.; Bundle, D. R., Shiga-like toxins are neutralized by tailored multivalent carbohydrate ligands. *Nature* **2000,** *403* (6770), 669-672.
199. Mourez, M.; Kane, R. S.; Mogridge, J.; Metallo, S.; Deschatelets, P.; Sellman, B. R.; Whitesides, G. M.; Collier, R. J., Designing a polyvalent inhibitor of anthrax toxin. *Nat. Biotechnol.* **2001,** *19* (10), 958-961.

200. Stella, B.; Arpicco, S.; Peracchia, M. T.; Desmaele, D.; Hoebeke, J.; Renoir, M.; D'Angelo, J.; Cattel, L.; Couvreur, P., Design of folic acid-conjugated nanoparticles for drug targeting. *Journal of Pharmaceutical Sciences* **2000,** *89* (11), 1452-1464.
201. Hong, S.; Leroueil, P. R.; Majoros, I. J.; Orr, B. G.; Baker, J. R.; Holl, M. M. B., The binding avidity of a nanoparticle-based multivalent targeted drug delivery platform. *Chemistry & Biology* **2007,** *14* (1), 107-115.
202. Paciotti, G. F.; Kingston, D. G. I.; Tamarkin, L., Colloidal gold nanoparticles: A novel nanoparticle platform for developing multifunctional tumor-targeted drug delivery vectors. *Drug Development Research* **2006,** *67* (1), 47-54.
203. Farma, J. M.; Puhlmann, M.; Soriano, P. A.; Cox, D.; Paciotti, G. F.; Tamarkin, L.; Alexander, H. R., Direct evidence for rapid and selective induction of tumor neovascular permeability by tumor necrosis factor and a novel derivative, colloidal gold bound tumor necrosis factor. *International Journal of Cancer* **2007,** *120* (11), 2474-2480.
204. Poon, Z.; Chen, S.; Engler, A. C.; Lee, H. I.; Atas, E.; von Maltzahn, G.; Bhatia, S. N.; Hammond, P. T., Ligand-Clustered "Patchy" Nanoparticles for Modulated Cellular Uptake and In Vivo Tumor Targeting. *Angewandte Chemie-International Edition* **2010,** *49* (40), 7266-7270.
205. Lyon, J. L.; Fleming, D. A.; Stone, M. B.; Schiffer, P.; Williams, M. E., Synthesis of Fe oxide core/Au shell nanoparticles by iterative hydroxylamine seeding. *Nano Lett.* **2004,** *4* (4), 719-723.
206. Ramesh, R.; Mhashilkar, A. M.; Tanaka, F.; Saito, Y.; Branch, C. D.; Sieger, K.; Mumm, J. B.; Stewart, A. L.; Boquio, A.; Dumoutier, L.; Grimm, E. A.; Renauld, J. C.; Kotenko, S.; Chada, S., Melanoma differentiation-associated gene 7/interleukin (IL)-24 is a novel ligand that regulates angiogenesis via the IL-22 receptor. *Cancer Research* **2003,** *63* (16), 5105-5113.
207. Yokoyama, T.; Miyazawa, K.; Naito, M.; Toyotake, J.; Tauchi, T.; Itoh, M.; Yuo, A.; Hayashi, Y.; Georgescu, M. M.; Kondo, Y.; Kondo, S.; Ohyashiki, K., Vitamin K2 induces autophagy and apoptosis simultaneously in leukemia cells. *Autophagy* **2008,** *4* (5), 629-640.
208. Aoki, H.; Kondo, Y.; Aldape, K.; Yamamoto, A.; Iwado, E.; Yokoyama, T.; Hollingsworth, E. F.; Kobayashi, R.; Hess, K.; Shinojima, N.; Shingu, T.; Tamada, Y.; Zhang, L.; Conrad, C.; Bogler, O.; Mills, G.; Sawaya, R.; Kondo, S., Monitoring autography in glioblastoma with antibody aganist isoform B of human microtuble-associated protein 1 light chain 3. *Autophagy* **2008,** *4* (4), 467-475.
209. Klionsky, D. J.; Abeliovich, H.; Agostinis, P.; Agrawal, D. K.; Aliev, G.; Askew, D. S.; Baba, M.; Baehrecke, E. H.; Bahr, B. A.; Ballabio, A.; Bamber, B. A.; Bassham, D. C.; Bergamini, E.; Bi, X. N.; Biard-Piechaczyk, M.; Blum, J. S.; Breclesen, D. E.; Brodsky, J. L.; Brumell, J. H.; Brunk, U. T.; Bursch, W.; Camougrand, N.; Cebollero, E.; Cecconi, F.; Chen, Y. Y.; Chin, L. S.; Choi, A.; Chu, C. T.; Chung, J. K.; Clarke, P. G. H.; Clark, R. S. B.; Clarke, S. G.; Clave, C.; Cleveland, J. L.; Codogno, P.; Colombo, M. I.; Coto-Montes, A.; Cregg, J. M.; Cuervo, A. M.; Debnath, J.; Demarchi, F.; Dennis, P. B.; Dennis, P. A.; Deretic, V.; Devenish, R. J.; Di Sano, F.; Dice, J. F.; DiFiglia, M.; Dinesh-Kumar, S.; Distelhorst, C. W.; Djavaheri-Mergny, M.; Dorsey, F. C.; Droge, W.;

Dron, M.; Dunn, W. A.; Duszenko, M.; Eissa, N. T.; Elazar, Z.; Esclatine, A.; Eskelinen, E. L.; Fesues, L.; Finley, K. D.; Fuentes, J. M.; Fueyo, J.; Fujisaki, K.; Galliot, B.; Gao, F. B.; Gewirtz, D. A.; Gibson, S. B.; Gohla, A.; Goldberg, A. L.; Gonzalez, R.; Gonzalez-Estevez, C.; Gorski, S.; Gottlieb, R. A.; Haussinger, D.; He, Y. W.; Heidenreich, K.; Hill, J. A.; Hoyer-Hansen, M.; Hu, X.; Huang, W. P.; Iwasaki, A.; Jaattela, M.; Jackson, W. T.; Jiang, X.; Jin, S. K.; Johansen, T.; Jung, J. U.; Kadowaki, M.; Kang, C.; Kelekar, A.; Kessel, D. H.; Kiel, J.; Kim, H. P.; Kimchi, A.; Kinsella, T. J.; Kiselyov, K.; Kitamoto, K.; Knecht, E.; Komatsu, M.; Kominami, E.; Konclo, S.; Kovacs, A. L.; Kroemer, G.; Kuan, C. Y.; Kumar, R.; Kundu, M.; Landry, J.; Laporte, M.; Le, W. D.; Lei, H. Y.; Lenardo, M. J.; Levine, B.; Lieberman, A.; Lim, K. L.; Lin, F. C.; Liou, W.; Liu, L. F.; Lopez-Berestein, G.; Lopez-Otin, C.; Lu, B.; Macleod, K. F.; Malorni, W.; Martinet, W.; Matsuoka, K.; Mautner, J.; Meijer, A. J.; Melendez, A.; Michels, P.; Miotto, G.; Mistiaen, W. P.; Mizushima, N.; Mograbi, B.; Monastyrska, I.; Moore, M. N.; Moreira, P. I.; Moriyasu, Y.; Motyl, T.; Munz, C.; Murphy, L. O.; Naqvi, N. I.; Neufeld, T. P.; Nishino, I.; Nixon, R. A.; Noda, T.; Nurnberg, B.; Ogawa, M.; Oleinick, N. L.; Olsen, L. J.; Ozpolat, B.; Paglin, S.; Palmer, G. E.; Papassideri, I.; Parkes, M.; Perlmutter, D. H.; Perry, G.; Piacentini, M.; Pinkas-Kramarski, R.; Prescott, M.; Proikas-Cezanne, T.; Raben, N.; Rami, A.; Reggiori, F.; Rohrer, B.; Rubinsztein, D. C.; Ryan, K. M.; Sadoshima, J.; Sakagami, H.; Sakai, Y.; Sandri, M.; Sasakawa, C.; Sass, M.; Schneider, C.; Seglen, P. O.; Seleverstov, O.; Settleman, J.; Shacka, J. J.; Shapiro, I. M.; Sibirny, A.; Silva-Zacarin, E. C. M.; Simon, H. U.; Simone, C.; Simonsen, A.; Smith, M. A.; Spanel-Borowski, K.; Srinivas, V.; Steeves, M.; Stenmark, H.; Stromhaug, P. E.; Subauste, C. S.; Sugimoto, S.; Sulzer, D.; Suzuki, T.; Swanson, M. S.; Takeshita, F.; Talbot, N. J.; Talloczy, Z.; Tanaka, K.; Tanida, I.; Taylor, G. S.; Taylor, J. P.; Terman, A.; Tettamanti, G.; Thompson, C. B.; Thumm, M.; Tolkovsky, A. M.; Tooze, S. A.; Truant, R.; Tumanovska, L. V.; Uchiyama, Y.; Ueno, T.; Uzcategui, N. L.; van der Klei, I.; Vaquero, E. C.; Vellai, T.; Vogel, M. W.; Wang, H. G.; Webster, P.; Wiley, J. W.; Xi, Z. J.; Xiao, G.; Yahalom, J.; Yang, J. M.; Yap, G.; Yin, X. M.; Yoshimori, T.; Yu, L.; Yue, Z. Y.; Yuzaki, M.; Zabirnyk, O.; Zheng, X. X.; Zhu, X.; Deter, R. L.; Tabas, I., Guidelines for the use and interpretation of assays for monitoring autophagy in higher eukaryotes. *Autophagy* **2008,** *4* (2), 151-175.

210. Gooi, H. C.; Hounsell, E. F.; Lax, I.; Kris, R. M.; Libermann, T. A.; Schlessinger, J.; Sato, J. D.; Kawamoto, T.; Mendelsohn, J.; Feizi, T., THE CARBOHYDRATE SPECIFICITIES OF THE MONOCLONAL-ANTIBODIES 29.1, 455 AND 3C1B12 TO THE EPIDERMAL GROWTH-FACTOR RECEPTOR OF A431 CELLS. *Bioscience Reports* **1985,** *5* (1), 83-94.

211. Seleverstov, O.; Zabirnyk, O.; Zscharnack, M.; Bulavina, L.; Nowicki, M.; Heinrich, J. M.; Yezhelyev, M.; Emmrich, F.; O'Regan, R.; Bader, A., Quantum dots for human mesenchymal stem cells labeling. A size-dependent autophagy activation. *Nano Lett.* **2006,** *6* (12), 2826-2832.

212. Mizushima, N., Methods for monitoring autophagy. *International Journal of Biochemistry & Cell Biology* **2004,** *36* (12), 2491-2502.

213. Mizushima, N.; Yoshimori, T., How to interpret LC3 immunoblotting. *Autophagy* **2007,** *3* (6), 542-545.
214. Tanida, I.; Minematsu-Ikeguchi, N.; Ueno, T.; Kominami, E., Lysosomal turnover, but not a cellular level, of endogenous LC3 is a marker for autophagy. *Autophagy* **2005,** *1* (2), 84-91.
215. Jablonski, A. E.; Kawakami, T.; Ting, A. Y.; Payne, C. K., Pyrenebutyrate Leads to Cellular Binding, Not Intracellular Delivery, of Polyarginine Quantum Dots. *Journal of Physical Chemistry Letters* **2010,** *1* (9), 1312-1315.
216. Ma, L. L.; Tam, J. O.; Willsey, B. W.; Rigdon, D.; Ramesh, R.; Sokolov, K.; Johnston, K. P., Selective Targeting of Antibody Conjugated Multifunctional Nanoclusters (Nanoroses) to Epidermal Growth Factor Receptors in Cancer Cells. *Langmuir* **2011,** *27* (12), 7681-7690.
217. (a) Patra, C. R.; Bhattacharya, R.; Wang, E. F.; Katarya, A.; Lau, J. S.; Dutta, S.; Muders, M.; Wang, S. F.; Buhrow, S. A.; Safgren, S. L.; Yaszemski, M. J.; Reid, J. M.; Ames, M. M.; Mukherjee, P.; Mukbopadhyay, D., Targeted delivery of gemcitabine to pancreatic adenocarcinoma using cetuximab as a targeting agent. *Cancer Research* **2008,** *68* (6), 1970-1978; (b) Milas, L.; Fan, Z.; Andratschke, N. H.; Ang, K. K., Epidermal growth factor receptor and tumor response to radiation: In vivo preclinical studies. *International Journal of Radiation Oncology Biology Physics* **2004,** *58* (3), 966-971.
218. (a) Schipper, M. L.; Iyer, G.; Koh, A. L.; Cheng, Z.; Ebenstein, Y.; Aharoni, A.; Keren, S.; Bentolila, L. A.; Li, J. Q.; Rao, J. H.; Chen, X. Y.; Banin, U.; Wu, A. M.; Sinclair, R.; Weiss, S.; Gambhir, S. S., Particle Size, Surface Coating, and PEGylation Influence the Biodistribution of Quantum Dots in Living Mice. *Small* **2009,** *5* (1), 126-134; (b) Kooi, M. E.; Cappendijk, V. C.; Cleutjens, K.; Kessels, A. G. H.; Kitslaar, P.; Borgers, M.; Frederik, P. M.; Daemen, M.; van Engelshoven, J. M. A., Accumulation of ultrasmall superparamagnetic particles of iron oxide in human atherosclerotic plaques can be detected by in vivo magnetic resonance imaging. *Circulation* **2003,** *107* (19), 2453-2458; (c) Betancourt, T.; Brown, B.; Brannon-Peppas, L., Doxorubicin-loaded PLGA nanoparticles by nanoprecipitation: preparation, characterization and in vitro evaluation. *Nanomedicine* **2007,** *2* (2), 219-232; (d) Almutairi, A.; Akers, W. J.; Berezin, M. Y.; Achilefu, S.; Frechet, J. M. J., Monitoring the Biodegradation of Dendritic Near-Infrared Nanoprobes by in Vivo Fluorescence Imaging. *Molecular Pharmaceutics* **2008,** *5* (6), 1103-1110.
219. Arruebo, M.; Fernandez-Pacheco, R.; Ibarra, M. R.; Santamaria, J., Magnetic nanoparticles for drug delivery. *Nano Today* **2007,** *2* (3), 22-32.
220. (a) Alivisatos, P., The use of nanocrystals in biological detection. *Nat. Biotechnol.* **2004,** *22* (1), 47-52; (b) Anker, J. N.; Hall, W. P.; Lyandres, O.; Shah, N. C.; Zhao, J.; Van Duyne, R. P., Biosensing with plasmonic nanosensors. *Nature Materials* **2008,** *7* (6), 442-453; (c) Skrabalak, S. E.; Chen, J.; Au, L.; Lu, X.; Li, X.; Xia, Y. N., Gold nanocages for biomedical applications. *Adv. Mater.* **2007,** *19* (20), 3177-3184.
221. Lewinski, N.; Colvin, V.; Drezek, R., Cytotoxicity of nanoparticles. *Small* **2008,** *4* (1), 26-49.

222. Tam, J. M.; Tam, J. O.; Murthy, A.; Ingram, D. R.; Ma, L. L.; Travis, K.; Johnston, K. P.; Sokolov, K. V., Controlled Assembly of Biodegradable Plasmonic Nanoclusters for Near-Infrared Imaging and Therapeutic Applications. *ACS Nano* **2010,** *4* (4), 2178-2184.
223. Tam, J. M.; Murthy, A. K.; Ingram, D. R.; Nguyen, R.; Sokolov, K. V.; Johnston, K. P., Kinetic Assembly of Near-IR-Active Gold Nanoclusters Using Weakly Adsorbing Polymers to Control the Size. *Langmuir* **2010,** *26* (11), 8988-8999.
224. Selvakannan, P. R.; Mandal, S.; Phadtare, S.; Pasricha, R.; Sastry, M., Capping of gold nanoparticles by the amino acid lysine renders them water-dispersible. *Langmuir* **2003,** *19* (8), 3545-3549.
225. Lim, I. I. S.; Ip, W.; Crew, E.; Njoki, P. N.; Mott, D.; Zhong, C. J.; Pan, Y.; Zhou, S. Q., Homocysteine-mediated reactivity and assembly of gold nanoparticles. *Langmuir* **2007,** *23* (2), 826-833.
226. Basu, S.; Pal, T., Glutathione-induced aggregation of gold nanoparticles: Electromagnetic interactions in a closely packed assembly. *Journal of Nanoscience and Nanotechnology* **2007,** *7* (6), 1904-1910.
227. (a) Boal, A. K.; Ilhan, F.; DeRouchey, J. E.; Thurn-Albrecht, T.; Russell, T. P.; Rotello, V. M., Self-assembly of nanoparticles into structured spherical and network aggregates. *Nature* **2000,** *404* (6779), 746-748; (b) Gindy, M. E.; Panagiotopoulos, A. Z.; Prud'homme, R. K., Composite block copolymer stabilized nanoparticles: Simultaneous encapsulation of organic actives and inorganic nanostructures. *Langmuir* **2008,** *24* (1), 83-90; (c) Ofir, Y.; Samanta, B.; Rotello, V. M., Polymer and biopolymer mediated self-assembly of gold nanoparticles. *Chem. Soc. Rev.* **2008,** *37* (9), 1814-1823.
228. Grabar, K. C.; Allison, K. J.; Baker, B. E.; Bright, R. M.; Brown, K. R.; Freeman, R. G.; Fox, A. P.; Keating, C. D.; Musick, M. D.; Natan, M. J., Two-dimensional arrays of colloidal gold particles: A flexible approach to macroscopic metal surfaces. *Langmuir* **1996,** *12* (10), 2353-2361.
229. Xu, L.; Guo, Y.; Xie, R. G.; Zhuang, J. Q.; Yang, W. S.; Li, T. J., Three-dimensional assembly of Au nanoparticles using dipeptides. *Nanotechnology* **2002,** *13* (6), 725-728.
230. (a) Sakai, T.; Alexandridis, P., Mechanism of gold metal ion reduction, nanoparticle growth and size control in aqueous amphiphilic block copolymer solutions at ambient conditions. *Journal of Physical Chemistry B* **2005,** *109* (16), 7766-7777; (b) Chow, M. K.; Zukoski, C. F., GOLD SOL FORMATION MECHANISMS - ROLE OF COLLOIDAL STABILITY. *Journal of Colloid and Interface Science* **1994,** *165* (1), 97-109.
231. Khlebtsov, B.; Zharov, V.; Melnikov, A.; Tuchin, V.; Khlebtsov, N., Optical amplification of photothermal therapy with gold nanoparticles and nanoclusters. *Nanotechnology* **2006,** *17* (20), 5167-5179.
232. Troutman, T. S.; Barton, J. K.; Romanowski, M., Biodegradable plasmon resonant nanoshells. *Adv. Mater.* **2008,** *20* (13), 2604-+.
233. Vasir, J. K.; Labhasetwar, V., Biodegradable nanoparticles for cytosolic delivery of therapeutics. *Advanced Drug Delivery Reviews* **2007,** *59* (8), 718-728.

234. Murthy, A. K.; Stover, R. J.; Borwankar, A. U.; Nie, G. D.; Gourisankar, S.; Truskett, T. M.; Sokolov, K. V.; Johnston, K. P., Equilibrium Gold Nanoclusters Quenched with Biodegradable Polymers. *ACS Nano* **submitted**.
235. Murthy, A. K.; Stover, R. J.; Hardin, W. G.; Schramm, R.; Nie, G. D.; Gourisankar, S.; Sokolov, K.; Johnston, K. P., Charged Gold Nanoparticles with Essentially Zero Serum Protein Adsorption in Undiluted Fetal Bovine Serum. **in press**.